

Detection of Retinal Nerve Fiber Layer

Progression in Glaucoma

YU, Chak Yan Marco

A Thesis Submitted in Partial Fulfillment

of the Requirements for the Degree of

Doctor of Philosophy

in

Ophthalmology and Visual Sciences

The Chinese University of Hong Kong

August 2013

Thesis/Assessment Committee

Professor THAM Chee Yung Clement (Chair)

Professor LEUNG Kai Shun Christopher (Thesis Supervisor)

Professor William Bernard GOGGINS III (Committee Member)

Professor Joel Steven SCHUMAN (External Examiner)

Abstract of thesis entitled:

Detection of Retinal Nerve Fiber Layer Progression in Glaucoma

Submitted by YU, Chak Yan Marco

For the degree of Doctor of Philosophy

in Ophthalmology and Visual Sciences

at The Chinese University of Hong Kong in August 2013

Abstract

Glaucoma is a neurodegenerative disease characterized by chronic degeneration of retinal ganglion cells with progressive loss in visual function. While measurements of the optic disc, retinal nerve fiber layer (RNFL) and visual sensitivity have been used to monitor glaucoma progression, little is known about the optimal strategy for detection of change. Both event and trend analyses (EA and TA) are adopted to evaluate glaucoma progression in clinical practice but the agreement between the two approaches is often poor. This research project set out to investigate the performance of EA and TA for detection of progressive RNFL thinning measured with optical coherence tomography (OCT) and its association with subsequent change in visual function.

In the computer simulation study, average RNFL thickness progression was modeled with reference to the individual's test-retest variabilities and different patterns and rates of progression. We showed that TA generally attained sensitivity and accuracy $\geq 80\%$ earlier than EA at similar specificities. These findings were validated with prospective

RNFL measurements collected from 107 glaucoma patients who had a median follow-up of 38 months. TA detected 35% whereas EA detected 12% to 28% of eyes with progression in eyes with average test-retest variability.

With the observation that TA generally outperformed EA, we then set forth to develop a trend-based algorithm to compute RNFL loss in the individual pixels in the RNFL thickness map (Trend-based Progression Analysis (TPA)), and compared its performance with Guided Progression Analysis (GPA) – a commercially available event-based counterpart. 68 eyes of 48 glaucoma patients followed for a median of 60 months were examined. Among the 23 eyes with evidence of GPA progression, TPA detected RNFL progression in all but 4 eyes. For the 45 eye without GPA progression, 19 had progression detected by TPA. For the 19 progressing eyes detected by GPA and TPA at the latest follow-up visit, over 73.7% had progression evident in TPA earlier than or at the same time with GPA. With the inclusion of the rates of change of RNFL measurements at individual pixels and the false discovery rate (a measure of false positives in the RNFL thickness map) in TPA, TPA can provide a more informative approach to analyze RNFL changes in glaucoma.

As the ultimate goal of glaucoma management is to preserve visual function, it is relevant to investigate whether RNFL progression would translate to subsequent change in function. Analyzing longitudinal RNFL and visual field measurements with autoregressive modeling in 84 eyes of 84 glaucoma and glaucoma suspect patients followed for a median of 49 months, we showed that prior average RNFL thickness and prior visual field MD were associated with subsequent loss in visual field MD in the early stages of glaucoma. RNFL measurement would be useful to predict subsequent loss in visual function.

In summary, TA outperformed EA for detection of progressive RNFL thinning. RNFL measurement would be useful to predict subsequent visual field progression and may thus be qualified as an outcome measure in clinical trials investigating glaucoma progression.

Abstract total word count: 492 words

摘要 (Abstract in Chinese)

青光眼是一類視神經退化性的視神經病變，主要表現為慢性，進展性的視網膜神經節細胞離亡，最終導致失明。研究表明，視神經的退化要早於視覺功能的損傷，因此分析結構性與功能性的參數改變對監測青光眼是極為重要的。

既 1991 年光學相幹斷層掃描儀的發明使得客觀測量視盤及視網膜成為可能。以往很多臨床研究著眼於結構與功能之間的相關性，但其二者之間的不同步性仍然是青光眼進展研究的一大問題。

我們開展縱向研究主要關注視網膜神經纖維層厚度和視野平均標準差之間的相關性。應用統計學模型，發現二者之間的不同步性主要取決於疾病的嚴重程度。對早期診斷青光眼，視網膜神經纖維層厚度相較於視野平均標準差更有幫助。

事件及趨勢分析方法被廣泛應用於研究疾病進展。然而，究竟哪種方法的敏感性及特異性更高則尚未知曉。我們採用數學模擬法分析縱向臨床數據，結果表明趨勢分析在檢測疾病進展的敏感性較高，且特異性與事件性分析相似。

我們進一步利用趨勢分析方法分析視網膜神經纖維層厚度圖的逐點像素，分析表明趨勢分析方法較事件分析方法更早檢測出青光眼進展。

總之，統計學模型可用於解釋在青光眼進展過程中的結構功能關係。視網膜神經纖維層厚度是檢測青光眼進展的重要參數。趨勢分析方法比事件分析方法可更早發現疾病進展。

Acknowledgements

I would like to express my deepest appreciation to all individuals providing the kind support and help throughout my PhD study in Ophthalmology. First and foremost, I would like to express my gratitude to my supervisor, Prof. Christopher K. S. Leung, for his invaluable guidance and advice towards my understanding glaucoma and its progression.

Furthermore, I would also like to thank Prof. Calvin C. P. Pang for providing research involvement opportunities to present in international meetings and conferences.

My thanks and appreciation also go to the imaging team members, Miss Gilda Lai, Miss Vivian Chiu, Dr. Shu Liu, Dr. Cong Ye, Dr. Guihua Xu, Miss Heather Mak and Dr. Zhongheng Wu for their work in data collection and patient caring.

TABLE OF CONTENTS

CHAPTER 1 INTRODUCTION.....	1
1.1 Definition and Epidemiology of Glaucoma	1
1.2 Pathogenesis of Glaucoma	2
1.3 Functional Assessments for Glaucoma	5
1.4 Optic Disc Assessment for Glaucoma	8
1.4.1 Optic disc stereophotography and red-free RNFL photography.	11
1.4.2 Confocal scanning laser ophthalmoscopy.....	12
1.4.3 Scanning laser polarimetry	13
1.4.4 Optical coherence tomography	15
1.5 Monitoring Glaucoma Progression	20
1.5.1 Visual Field Progression	20
1.5.2 Optic Disc and RNFL Progression	24
1.6 Statistical Methods of Progression Analysis	30
1.6.1 Event-based Analysis.....	30
1.6.2 Trend-based Analysis	33
1.6.3 Advanced Regression Analysis	35
1.6.4 Comparison of Trend and Event Analyses to detect structural progression.....	44
1.6.5 Comparison of Trend and Event Analyses to detect Functional Progression	45
1.6.6 Structural and Functional Progression Detection Strategies	46
1.7 Project Objectives.....	48
CHAPTER 2 GENERAL MATERIALS AND METHODS.....	53
2.1 Subject Enrollments	53
2.2 Inclusion and Exclusion Criteria.....	53
2.3 Humphrey Visual Field Perimetry.....	54
2.4 Spectral-Domain OCT RNFL Imaging	55
2.5 Definition of Glaucoma, Glaucoma Suspects and Normal Subjects 56	
2.6 Statistical Analysis.....	56
CHAPTER 3 THE INVESTIGATION OF RETINAL NERVE FIBER LAYER PROGRESSION DETECTION.....	58

3.1	Computer Simulation of Progressive Retinal Nerve Fiber Layer Loss in Glaucoma: A Comparison between Event and Trend Analysis....	59
3.1.1	Abstract.....	59
3.1.2	Background and Objectives	61
3.1.3	Subjects and Methods.....	63
3.1.4	Statistics.....	67
3.1.5	Results	72
3.1.6	Discussion	78
3.2	Detection of Retinal Nerve Fiber Layer (RNFL) Progression using the RNFL thickness map.....	100
3.2.1	Abstract.....	100
3.2.2	Background and Objectives	102
3.2.3	Subjects and Methods.....	103
3.2.4	Results	109
3.2.5	Discussion	112
3.3	Impact of Retinal Nerve Fiber Layer Measurement on Subsequent Change in Visual Function	129
3.3.1	Abstract.....	129
3.3.2	Background and Objectives	131
3.3.3	Subjects and Methods.....	132
3.3.4	Results	135
3.3.5	Discussion	138
CHAPTER 4 GENERAL CONCLUSIONS		150
4.1	Conclusions.....	150
4.2	Future Works.....	152
BIBLIOGRAPHY.....		153
APPENDIX		179

LIST OF TABLES

Table 3.1.1	Demographics, retinal nerve fiber layer (RNFL), and visual field measurements of 46 eyes of 46 subjects who underwent weekly RNFL evaluations for 8 consecutive weeks.	87
Table 3.1.2	Demographics, retinal nerve fiber layer (RNFL), and visual field measurements of 175 eyes of 107 glaucoma and glaucoma suspect subjects who were followed up every 4 months for at least 30 months.	88
Table 3.2.1	Demographics, RNFL, and visual field measurements of 68 eyes of 48 glaucoma subjects and 60 eyes of 34 normal subjects who were followed up every 4 months for at least 36 months.	119
Table 3.3.1	Demographics, Retinal Nerve Fiber Layer (RNFL), and visual field measurements of 84 eyes of 84 glaucoma and glaucoma suspect subjects who were followed up every 4 months for at least 35 months.	143
Table 3.3.2	Coefficient estimates of Random Coefficient Autoregressive Linear Mixed Model (RCALMM) for the change in visual field mean deviation (MD) on the prior average RNFL thickness and the prior visual field MD.	144
Table 3.3.3	Coefficient estimates of Random Coefficient Autoregressive Linear Mixed Model (RCALMM) for the change in average RNFL thickness on the prior average RNFL thickness and the prior visual field MD.	145
Table 3.3.4	Coefficient estimates of Random Coefficient Autoregressive Linear Mixed Models (RCALMMs) for the average RNFL thickness and visual field MD on the prior average RNFL thickness, the prior visual field MD, follow-up duration, age and spherical error.	146
Table 3.3.5	Coefficient estimates of Linear Mixed Models (LMMs) for the average RNFL thickness and visual field MD on the follow-up duration, age and spherical error.	147

LIST OF FIGURES

Figure 1.1	Classification tree of glaucoma.	50
Figure 1.2	Retinal nerve fiber bundle trajectories.	51
Figure 1.3	Visualization of a bivariate autoregressive model of order 1 with X_t causing Y_t .	52
Figure 3.1.1	Progressive average retinal nerve fiber layer (RNFL) thickness reduction modeled in linear, episodic, exponential, and parabolic patterns at an average rate of $-2.0 \mu\text{m}/\text{year}$ over 60 months.	89
Figure 3.1.2	Schematics illustrating simulation of 16 serial average retinal nerve fiber layer (RNFL) thickness measurements over 60 months.	90
Figure 3.1.3	Sensitivity profiles for detection of retinal nerve fiber layer (RNFL) progression at a rate of $-2 \mu\text{m}/\text{year}$ by trend and event analyses computed from month 12 to month 60.	91
Figure 3.1.4	Relationship between the rate of linear change in average RNFL thickness and the minimum duration required for TA and EA to detect progression at a sensitivity of 80%.	92
Figure 3.1.5	Sensitivity profiles for detection of retinal nerve fiber layer (RNFL) progression at a rate of $-4 \mu\text{m}/\text{year}$ by trend and event analyses computed from month 12 to month 60.	93
Figure 3.1.6	Specificity profiles of trend and event analyses.	94
Figure 3.1.7	Accuracy profiles for detection of retinal nerve fiber layer (RNFL) progression at a rate of $-2 \mu\text{m}/\text{year}$ by trend and event analyses computed from month 12 to month 60 in the simulation.	95
Figure 3.1.8	Accuracy profiles for detection of retinal nerve fiber layer (RNFL) progression at a rate of $-4 \mu\text{m}/\text{year}$ by trend and event analyses computed from month 12 to month 60 in the simulation.	96
Figure 3.1.9	Proportion of eyes detected with retinal nerve fiber layer progression by TA and EA in 175 eyes of 81 glaucoma and 26 glaucoma suspect subjects.	97
Figure 3.1.10	The impact of individual test-retest variability on the sensitivity and specificity of even analysis with group reproducibility coefficient (EA with group RC).	98
Figure 3.1.11	Relationship between the number of observations required per year and the minimum duration needed to detect a linear average RNFL thickness progression at rate of $-2 \mu\text{m}/\text{year}$.	99

Figure 3.2.1	An example of retinal nerve fiber layer progression analysis evaluated the Guided Progression Analysis (GPA) and the Trend-based Progression Analysis (TPA).	120
Figure 3.2.2	Another example of retinal nerve fiber layer progression analysis evaluated by the Guided Progression Analysis (GPA) and the Trend-based Progression Analysis (TPA).	122
Figure 3.2.3	Agreement of the localized RNFL progression detected by the Trend-based Progression Analysis (TPA) and Guided Progression Analysis (GPA) in the glaucoma group.	124
Figure 3.2.4	Survival probabilities of Trend-based Progression Analysis (TPA) and Guided Progression Analysis (GPA) estimated by the Kaplan–Meier estimators in the glaucoma group.	125
Figure 3.2.5	The overlay of the RNFL change maps obtained in the latest follow-up analyzed by Guided Progression Analysis (GPA) and Trend Progression Analysis (TPA) in the glaucoma group.	126
Figure 3.2.6	Agreement of the localized RNFL progression detected by the Trend-based Progression Analysis (TPA) and Guided Progression Analysis (GPA) in the normal group.	127
Figure 3.2.7	Survival probabilities of Trend-based Progression Analysis (TPA) and Guided Progression Analysis (GPA) estimated by the Kaplan–Meier estimators in the normal group.	128
Figure 3.3.1	Agreement of RNFL thickness and visual field progression in the 84 eyes of 84 subjects.	148
Figure 3.3.2	An example of spurious causality when an autoregressive model of order 2 is wrongly specified as autoregressive model of order 1.	149

ABBREVIATIONS

AGIS	Advanced Glaucoma Intervention Study
AR	Autoregressive
ARMA	Autoregressive Moving Average
CIGTS	Collaborative Initial Glaucoma Treatment Study
CSLO	Confocal Scanning Laser Ophthalmoscopy
EA	Event Analysis
EMGT	Early Manifest Glaucoma Trial
FDR	False Discovery Rate
FWER	Family-wise Error Rate
GPA	Guided Progression Analysis
HRT	Heidelberg Retina Tomograph
IOP	Intracocular pressure
LMM	Linear Mixed Model
LRT	Likelihood Ratio Test
MD	Mean Deviation
MLE	Maximum Likelihood Estimator
OAG	Open-angle glaucoma
OCT	Optical Coherence Tomography
OLS	Ordinary Least Square
ONH	Optic nerve head
RC	Reproducibility Coefficient
RCA	Random Coefficient Autoregressive
RCALMM	Random Coefficient Autoregressive Linear Mixed Model
RGC	Retinal Ganglion Cells
RNFL	Retinal Nerve Field Layer
SAP	Standard automated perimetry
SD	Standard Deviation
SLP	Scanning Laser Polarimetry
SPDE	Stochastic Partial Differentiate Equation
TA	Trend Analysis
TCA	Topographic Change Analysis
TPA	Trend-based Progression Analysis
VFI	Visual Field Index

PUBLICATION

Publications relevant to the work of this thesis

Yu, M., Weinreb, R. N., Yiu, C., Liu, S., Or, M. K., Ye, C., Lam, D. S.-C., Leung C.K.S. (2011). Computer simulation of progressive retinal nerve fiber layer loss in glaucoma: performance of event and trend analyses. *Investigative ophthalmology & visual science*, 52(13), 9674–9683. doi:10.1167/iovs.11-8052

Yu, M., Leung C.K.S, Detection of Retinal Nerve Fiber Layer (RNFL) Progression using the RNFL thickness map.

Non-provisional patent filed in the United States in May 2013 (attached in the Appendix) with funding support provided by the Knowledge Transfer Office (KTO) of The Chinese University of Hong Kong

Yu, M., Lai, G., Leung, C. K. S. Impact of Retinal Nerve Fiber Layer Measurement on Subsequent Change in Visual Function. Pending submission.

Publications related to Retinal Nerve Fiber Layer Imaging

1. Leung, C. K. S., Yu, M., Weinreb, R. N., Ye, C., Liu, S., Lai, G., & Lam, D. S. C. (2012). Retinal nerve fiber layer imaging with spectral-domain optical coherence tomography: a prospective analysis of age-related loss. *Ophthalmology*, 119(4), 731–737. doi:10.1016/j.ophtha.2011.10.010
2. Leung, C. K.-S., Yu, M., Weinreb, R. N., Lai, G., Xu, G., & Lam, D. S.-C. (2012). Retinal nerve fiber layer imaging with spectral-domain optical coherence tomography: patterns of retinal nerve fiber layer progression. *Ophthalmology*, 119(9), 1858–1866. doi:10.1016/j.ophtha.2012.03.044
3. Leung, C. K.-S., Yu, M., Weinreb, R. N., Mak, H. K., Lai, G., Ye, C., & Lam, D. S.-C. (2012). Retinal Nerve Fiber Layer Imaging with Spectral-Domain Optical Coherence Tomography: Interpreting the RNFL Maps in Healthy Myopic Eyes. *Investigative ophthalmology & visual science*, 53(11), 7194–7200. doi:10.1167/iovs.12-9726
4. Yang, B., Ye, C., Yu, M., Liu, S., Lam, D. S. C., & Leung, C. K. (2012). Optic disc imaging with spectral-domain optical coherence tomography: variability and agreement study with Heidelberg retinal tomograph. *Ophthalmology*, 119(9), 1852–1857. doi:10.1016/j.ophtha.2012.02.033

5. Leung, C. K.-S., Chiu, V., Weinreb, R. N., Liu, S., Ye, C., **Yu, M.**, Cheung, C. Y.-L., et al. (2011). Evaluation of retinal nerve fiber layer progression in glaucoma: a comparison between spectral-domain and time-domain optical coherence tomography. *Ophthalmology*, 118(8), 1558–1562. doi:10.1016/j.ophtha.2011.01.026
6. Ye, C., To, E., Weinreb, R. N., **Yu, M.**, Liu, S., Lam, D. S. C., & Leung, C. K. S. (2011). Comparison of retinal nerve fiber layer imaging by spectral domain optical coherence tomography and scanning laser ophthalmoscopy. *Ophthalmology*, 118(11), 2196–2202. doi:10.1016/j.ophtha.2011.03.035

Other Publications during the PhD study

1. Jhanji, V., Yang, B., **Yu, M.**, Ye, C., & Leung, C. K. (2013). Corneal thickness and elevation measurements using swept source optical coherence tomography and slit scanning topography in normal and keratoconic eyes. *Clinical & experimental ophthalmology*. doi:10.1111/ceo.12113
2. Lai, I., Mak, H., Lai, G., **Yu, M.**, Lam, D. S. C., & Leung, C. K. S. (2013). Anterior Chamber Angle Imaging with Swept-Source Optical Coherence Tomography: Measuring Peripheral Anterior Synechia in Glaucoma. *Ophthalmology*. doi:10.1016/j.ophtha.2012.12.006
3. McKee, H., Ye, C., **Yu, M.**, Liu, S., Lam, D. S. C., & Leung, C. K. S. (2013). Anterior Chamber Angle Imaging With Swept-Source Optical Coherence Tomography: Detecting the Scleral Spur, Schwalbe's Line, and Schlemm's Canal. *Journal of glaucoma*. doi:10.1097/IJG.0b013e31824485fa
4. Agarwal, T., Bhartiya, S., Dada, T., Panda, A., Jhanji, V., & **Yu, M.** (2012). Agreement of corneal thickness measurement using slitlamp and ultrasound pachymetry. *Eye & contact lens*, 38(4), 231–233. doi:10.1097/ICL.0b013e318250884e
5. Liu, S., **Yu, M.**, Ye, C., Lam, D. S. C., & Leung, C. K.-S. (2011). Anterior chamber angle imaging with swept-source optical coherence tomography: an investigation on variability of angle measurement. *Investigative ophthalmology & visual science*, 52(12), 8598–8603. doi:10.1167/iovs.11-7507
6. Li, Z., Liu, S., Weinreb, R. N., Lindsey, J. D., **Yu, M.**, Liu, L., Ye, C., et al. (2011). Tracking dendritic shrinkage of retinal ganglion cells after acute elevation of intraocular pressure. *Investigative*

ophthalmology & visual science, 52(10), 7205–7212.
doi:10.1167/iovs.10-6868

Poster Presentations in International Ophthalmology Meetings

1. Yu, M., Liu, S., Weinreb, R. N., Lai, G. Lam, D. S., Leung, C. K. A prospective analysis of frequency doubling technology perimetry for detection of visual field progression. International Symposium of Ophthalmology. December 14 - 16, 2012. Hong Kong, China.
2. Yu, M. C. Y., Lai, G. W. K., Weinreb, R. N., Chiu, V. S. M., Lam, D. S. C., Pang, C. C. P., Leung, C. K. S. Analysis of retinal nerve fiber layer (RNFL) defects in glaucoma progression. World Glaucoma Congress. June 29 - July 2, 2011. Paris, France.

CHAPTER 1 INTRODUCTION

1.1 Definition and Epidemiology of Glaucoma

Glaucoma is an optic neuropathy characterized by chronic progressive degeneration of retinal ganglion cells with clinical features including thinning of the retinal nerve fiber layer, narrowing of the neuroretinal rim, and optic disc cupping. Visual sensitivity is gradually loss which can eventually lead to blindness if treatment is not initiated.

Glaucoma is generally classified into open-angle glaucoma (OAG) and angle-closure glaucoma (ACG) according to the anterior chamber angle configuration. With reference to the etiology, OAG and ACG can be further subclassified into primary and secondary glaucoma (Figure 1.1).

Glaucoma is the second leading cause of global blindness after cataract since 1990 (Resnikoff & Keys, 2012), which causes around 8% of global blindness in 2010 (Pascolini & Mariotti, 2011). Worldwide, it is estimated that 60.5 million of people were suffering from glaucoma in 2010 and is predicted to grow to 79.6 million by 2020. Among the 60.5 million of people suffering from glaucoma, 44.7 and 15.7 million of people were open-angle glaucoma (OAG) and angle-closure glaucoma (ACG), respectively. Notably, 47% of OAG and 87% of ACG were Asians. 4.5 million of OAG patients and 3.9 million of ACG patients had bilateral blindness in 2010. These numbers are expected to increase to 5.9 and 5.3 million, respectively, by 2020. (Quigley & Broman, 2006)

1.2 Pathogenesis of Glaucoma

The pathogenesis of glaucoma is multifactorial and apoptosis is a key pathological process observed in retinal ganglion cells in eyes with glaucoma (Quigley, 2011). There are multiple factors influencing the structural and functional integrity of retinal ganglion cells.

The mechanical theory proposes that elevated intraocular pressure (IOP) mechanically compresses the lamina cribrosa, disrupting axoplasmic transport and leading to retinal ganglion cell degeneration (Fechtner & Weinreb, 1994, Agarwal et al., 2009). Animal studies show that both the level and duration of IOP elevation are positively correlated with RGC axon loss (Chauhan et al., 2002, Levkovitch-Verbin et al., 2002).

The vascular theory proposes that retinal ganglion cell axon death may be due to insufficient blood supply to the optic nerve head consequential to loss in capillaries, compromised microcirculation, and alterations in choroidal blood flow (Fechtner & Weinreb, 1994, Agarwal et al., 2009, Flammer et al., 2002, Grieshaber & Flammer, 2005). In healthy eyes, there is an efficient autoregulatory mechanism to maintain a constant rate of blood flow in the retina and optic nerve head (Bill & Sperber, 1990). However, in glaucomatous eyes, the ocular perfusion pressure is compromised, which is particularly deleterious in patients with low systemic blood pressure (Michelson et al., 1998, Chung et al., 1999, Grunwald et al., 1999), In fact, reduced diastolic perfusion pressure has

been shown to be an important risk factor for POAG (Bonomi et al., 2000).

Although the exact molecular mechanism(s) contributing to RGC apoptosis is unknown, glutamate toxicity, formation of nitric oxide and free radicals have been shown to be associated with RGC death in glaucoma. Hypoxia can induce the release of glutamate in the retina (Neal et al., 1994). Glutamate is an essential neurotransmitter in the retina and it can be toxic to the retinal neurons when the concentration in the retina is high. Glutamate toxicity was first demonstrated in an animal study conducted by Lucas & Newhouse, who observed severe RGC death after subcutaneous injection of glutamate in young mice (Lucas & Newhouse, 1957). Similar glutamate-induced retinal toxicity was also reported by Olney and the term "excitotoxicity" was introduced to describe the damage developed upon exposure to excess level of excitatory neurotransmitter (Olney, 1969). Vorwerk et al. found that glutamate is also toxic to RGCs when its level is mild but chronically elevated. (Vorwerk et al., 1996).

Excessive production of nitric oxide (NO) by astrocytes and microglia in the optic nerve head has been found to be associated with neuronal loss. NO is synthesized from L-arginine by the NO synthases and has been detected in three isoforms (Moncada & Higgs, 1993). In normal human eyes, NOS-1 has been detected in scattered astrocytes throughout the optic nerve head, which indicates that this isoform is

constitutive in certain glia and that NO may serve as a physiological mediator between astrocytes or between astrocytes and axons. By contrast, in patients with glaucoma, numerous cell bodies are positive for the presence of NOS-1 on the vitreal surface, in the remnant glial cells and in the cells in lamina cribrosa within glaucomatous tissue (Neufeld, 1999). NOS-3 is a constitutive isoform found in the vascular endothelial cells in the prelaminar region of the optic nerve head in normal eyes. In glaucomatous eye, vascular endothelial NOS-3 may cause vasodilation and contribute to increased blood flow and thereby offering neuroprotection (Neufeld, 1999). NOS-2 is the inducible form of the enzyme which reacts to diverse conditions such as exposure to cytokines and elevated IOP to produce excessive amount of NO. Significant amount of NOS-2 has been found in the astrocytes and microglia at the optic nerve head of patients with glaucoma (Liu & Neufeld, 2000, Liu & Neufeld, 2001).

Excessive formation of free radicals and oxidative stress from aerobic metabolism or vascular dysregulation are known to damage the DNA of the trabecular meshwork cells and altered the outflow of aqueous humor in glaucoma. In the study conducted by Izzotti et al., the oxidative DNA damage was measured by 8-hydroxy-2'-deoxyguanosine in the trabecular meshwork region from 42 glaucoma patients and 45 control subjects. Oxidative DNA damage is found to be significantly increased in glaucoma patients and correlated with intraocular pressure (IOP) (Izzotti

et al., 2003). Similar findings were observed in the study conducted by Saccà et al. with a sample of 17 glaucomatous eyes and 21 healthy eyes (Saccà et al., 2005).

1.3 Functional Assessments for Glaucoma

The goal in glaucoma management is to preserve visual function to meet with the needs of the patient for his/her lifespan. Since glaucomatous visual field loss commonly occurs in correspondence with the retinal nerve fiber bundle defects, understanding the retinal nerve fiber bundle trajectories is a prerequisite for diagnosing and monitoring glaucomatous damage. In the retina, the nerve fibers at the nasal side of the fovea travel directly into the temporal sector of the ONH and the nerve fibers at the temporal side travel to superotemporal and inferotemporal sectors of the ONH in arched traveling paths without crossing the horizontal midline (Figure 1.2) (Fitzgibbon & Taylor, 1996, Jansonius et al., 2009, Garvin et al., 2012). Therefore, glaucomatous visual field defects are often observed in arcuate-shaped extension of the blind spot corresponding to the nerve fiber bundle trajectories (Weber & Ulrich, 1991, Garway-Heath et al., 2000). Visual field loss commonly occurs first in the superonasal or inferonasal field.

Perimetry plays an important role in detection of visual field defects in glaucoma. Perimetry can be classified into kinetic and static testing. Kinetic perimetry uses moving light stimulus with fixed size and

brightness from a peripheral non-detectable location to a location where it is first detected by the test subject. The procedure is repeated until the visual field is mapped out. On the other hand, static perimetry uses stationary light stimulus with varying size and brightness. It presents light stimulus with different levels of intensity at different test locations and determines the stimulus intensity with 50% probability of perception. The intensity that results in 50% probability of perception is called the threshold or differential luminance sensitivity. Static perimetry is the reference standard for evaluation of glaucomatous damage.

Standard white-on-white automated perimetry (SAP)

Standard automated perimetry is a well-established technology to measure the thresholds of visual field in glaucoma. The white-on-white perimetry presents test stimulus with varying size and brightness against a standard white background at each test location. Humphrey Field Analyzer (HFA, Carl Zeiss Meditec, Dublin, California) is a popular commercial automated perimetry for visual field assessment. It provides global indices including mean deviation (MD), pattern standard deviation (PSD) and visual field index (VFI) to indicate the average visual sensitivity of the whole visual field. MD is defined as the average of the deviations of threshold values across all test locations in the total deviation plot. A negative MD value signifies a reduction in visual sensitivity compared with a reference normal visual field. PSD is a measure defined as the standard deviation of the deviations values

across all test locations in the pattern deviation plot. A large PSD is associated with high likelihood of the existence of localized defects. Localized visual field defects can be observed in the probability plots of the pattern deviation values with reference to a normative database. VFI is an age-corrected index to determine the percentage of visual field preserved (Bengtsson & Heijl, 2008). A VFI of 100% represents a normal visual field and 0% represents a perimetrically blind field.

Visual field progression is analyzed by the Guided Progression Analysis (GPA) software in HFA. GPA includes a linear regression analysis of VFI across time to estimate the rate of change in visual function and a progression analysis plot to detect the difference between baseline and follow-up visual sensitivity that exceeds the variability derived from the normative database with simple plain-language messages (no progression, possible progression and likely progression) based on the criteria used in the Early Manifest Glaucoma Trial (EMGT) (please refer to section 1.5.1.1 for detail).

Other types of perimetry testing in glaucoma

Frequency doubling technology perimetry uses frequency doubling illusion first described by Kelly in 1966 (Kelly, 1966) to measure the visual sensitivity to vertical gratings stimulus counter-phase flickered at high temporal frequency. It has shown to have above 85% sensitivity and specificity for the detection of glaucoma in early stage (Cello et al.,

2000). Humphrey Matrix (Carl Zeiss Meditec, Dublin, California) is the second generation of FDT perimetry which provides similar visual field indices as Humphrey Field Analyzer (HFA; Carl Zeiss Meditec, Dublin, California) to quantify visual sensitivity. Short-wavelength perimetry projects blue stimulus on a yellow background to quantify the visual function. Since there is relatively less dense matrix of blue cones serving the central visual field, it was believed to detect glaucomatous visual field loss earlier than SAP. However, a recent study by van der Schoot et al. showed that out of 24 glaucoma suspect eyes that converted to glaucoma, only 2 (8%) had earlier conversion detected in SWAP. In contrast, 15 (63%) eyes had conversion detected in SAP earlier (van der Schoot et al., 2010) than SWAP.

1.4 Optic Disc Assessment for Glaucoma

Thinning of retinal nerve fiber layer (RNFL), narrowing of the neuroretinal rim, and optic disc cupping are the key characteristic structural changes in glaucoma. Assessment of the RNFL and optic nerve head are critical in diagnosing and monitoring of glaucoma. Optic disc stereophotography (Morgan et al., 2005), red-free RNFL photography (Hoyt et al., 1973), confocal scanning laser ophthalmoscopy (Webb et al., 1987), scanning laser polarimetry (Weinreb et al., 1990), and optical coherence tomography (Huang et al., 1991) are common imaging techniques to measure the RNFL and ONH. Most imaging techniques can provide high measurement repeatability

and reproducibility (Weinreb et al., 1993, Chauhan et al., 1994, Hoh et al., 1998, Mikelberg et al., 1993, Paunescu et al., 2004, Kruse et al., 1989, Budenz et al., 2008, Leung et al., 2009, Leung et al., 2008).

Evaluation of optic disc stereophotography and red-free RNFL photography is largely subjective and thus limited by considerable inter-observer variability (Coleman et al., 1996, Azuara-Blanco et al., 2003, Jampel et al., 2009).

A number of studies have demonstrated that RNFL and ONH changes can be detected before visual field defects are apparent (Airaksinen et al., 1981, Quigley et al., 1992). Localized RNFL defect in glaucoma was first illustrated by Hoyt (Hoyt et al., 1973). According to Jonas & Dichtl (Jonas & Dichtl, 1996), RNFL defects are wedge-shaped and running toward the optic disc border, which occurred in about 20% of all glaucoma eyes. Due to the uneven distribution of RNFL thickness around the ONH, localized RNFL defects are most commonly occurred in the inferior temporal and superior temporal sectors followed by the inferior nasal and superior nasal sectors (Quigley & Addicks, 1982). Similar to the RNFL defects, neuroretinal rim loss is found predominantly at the inferotemporal and superotemporal sectors in the early stages of glaucoma, followed by the temporal and then nasal sectors when the disease reaches moderate and advanced stages (Jonas et al., 1993).

Optic disc cupping is another important sign observed in glaucoma. Optic cup size varies among individuals and positively correlates with optic disc size (Bengtsson, 1976, Caprioli & Miller, 1987, Jonas, et al. 1988a). Because of the correlation between the cup and disc area, cup/disc ratio, which is defined as the ratio of cup to disc diameters, is small in small optic discs and large in large optic discs. In normal eyes, horizontal cup/disc ratio is reported to be greater than vertical cup/disc ratio in 93% of eyes (Jonas et al., 1988a). Since the vertical cup/disc ratio increases faster than the horizontal cup/disc ratio in early to moderate stages of glaucoma, the quotient of horizontal to vertical cup/disc ratio smaller than one may provide an important indication of the development of glaucoma (Jonas et al., 1988b, Jonas et al., 1988c).

Peripapillary atrophy is associated with glaucoma. It can be divided into β and α zones. β zone is characterized by a complete loss of retinal pigment epithelium located near the optic disc margin. α zone is characterized by irregular hypopigmentation and hyperpigmentation in the retinal pigment epithelium located peripheral to β zone. Although both zones are observed in normal and non-glaucoma eyes, they are significantly larger in glaucoma eyes and the β zone is found to occur more often in glaucoma eyes (Jonas et al., 1989, Jonas & Naumann, 1989, Jonas et al., 1992). According to Tezel et al. (Tezel et al., 1997a, Tezel et al., 1997b), the presence and size of peripapillary atrophy are related to the development of subsequent optic disc or visual field

damage in ocular hypertension which may be an important feature in early glaucoma.

Splinter-shaped or flame-shaped hemorrhages at the margin of the optic disc are also associated with glaucoma. They often precede the onset of RNFL and visual field defects (Airaksinen et al., 1981a, Airaksinen & Heijl, 1983). Population studies estimated that optic disc hemorrhages occurred in about 1% of normal eyes (Healey et al., 1998, Yamamoto et al., 2004). By contrast, their prevalence was around 7-14% in glaucoma eyes (Airaksinen et al., 1981b, Gloster, 1981, Healey et al., 1998, Yamamoto et al., 2004). Although it is a rather specific sign in glaucoma, its low sensitivity limits its role in early detection of glaucoma.

Detection of Optic Disc Changes

1.4.1 Optic disc stereophotography and red-free RNFL

photography

Optic disc stereophotography and red-free RNFL photography have been used for diagnosing and monitoring glaucoma for decades. Optic disc stereophotography is useful to examine neuroretinal rim notching and narrowing, disc cupping and hemorrhages. On the other hand, red-free RNFL photography is useful to observe localized or diffuse loss of the RNFL. However, reliable examination of the optic disc and RNFL relies on the availability of high quality optic disc and RNFL images, which is subject to the influence of media opacity and imaging

techniques. Notably, intraobserver and interobserver agreement for optic disc evaluation with optic disc stereophotography and red-free RNFL photography has been shown to be fair (Coleman et al., 1996, Azuara-Blanco et al., 2003, Jampel et al., 2009).

1.4.2 Confocal scanning laser ophthalmoscopy

Confocal scanning laser ophthalmoscopy (cSLO) makes use of laser light to illuminate the retina. It emits light ray to the optic disc and retina and measures the reflected light through a pinhole which only allows light ray reflected from the focal plane to pass through. It starts scanning above the retinal surface, then captures parallel images at increasing depths and stacks images together to form a three-dimensional topographic image of the retina and optic disc (Weinreb et al., 1989).

The Heidelberg Retina Tomograph (HRT; Heidelberg Engineering, GmbH, Heidelberg, Germany) is a commercially available confocal scanning laser ophthalmoscope which provides two classification methods (1) the Moorfields Regression Analysis (MRA) and (2) the Glaucoma Probability Scores (GPS) to separate healthy and glaucomatous eyes. MRA discriminates glaucomatous from healthy eyes by using global and sectorial rim area adjusted for disc size and age of the examined optic disc and compares the rim area with a database of normal eyes (Wollstein et al., 1998). However, the subjectively drawn contour line of the optic disc results in moderate

interobserver and intraobserver agreement of rim area measurement (Garway-Heath et al., 1999).

By contrast, GPS is a contour line-independent method, which uses Bayesian machine-learning classifier to compare the shape of the examined optic disc with those obtained from healthy and glaucomatous eyes to evaluate the likelihood of optic disc damage (Swindale et al., 2000). The classification performance is comparable to MRA. However, the classification performance of both GPS and MRA varies with the optic disc size (Coops et al, 2006).

1.4.3 Scanning laser polarimetry

Scanning laser polarimetry (SLP) uses a polarized laser beam on to the retina and measures the retardation of the reflected light from the nerve fiber layer tissue. A fixed conversion factor (0.67 nm/ μm) is used to calculate the RNFL thickness in micrometers (Weinreb et al., 1990, Weinreb et al., 1998, Knighton et al., 1998). Other than the RNFL, the cornea and the lens are also birefringent structures. The measured retardation due to these structures have to be neutralized in order to derive the retardation of the RNFL (Greenfield et al., 2000, Weinreb et al., 2002). The variable corneal compensation (VCC) is a technique to compensate the anterior segment birefringence (Qienyuan Zhou & Weinreb, 2002) and is used in the commercial device, GDx (Carl Zeiss Meditec, Dublin, California). However, atypical patterns of elevated

retardation may appear in SLP-VCC images result in inaccurate calibration of the RNFL thickness (Reus & Lemij, 2004). The enhanced corneal compensation (ECC) algorithm is introduced in 2006 to better compensate the atypical retardation patterns and residual anterior segment birefringence in measuring the RNFL thickness (Q Zhou, 2006). This ECC algorithm is introduced in the GDxPro (Carl Zeiss Meditec, Dublin, California), the latest generation of GDx. The ECC algorithm provides a lower measurement variability of RNFL thickness (Tóth & Holló, 2005) and better classification performance to discriminate glaucomatous from healthy eyes (Medeiros et al., 2007).

The Nerve Fiber Indicator (NFI) calculated by both GDxVCC and GDxECC is an indicator of the likelihood of abnormal RNFL thickness based on support vector machine trained to discriminate healthy from glaucomatous eyes. There is evidence suggesting that the classification performance of NFI is better than the TSNIT (temporal, superior, nasal, inferior, temporal) average, superior average, inferior average RNFL thickness (Dada et al., 2009). RNFL defects can be detected by the RNFL thickness deviation map in both GDxVCC and GDxECC. The RNFL thickness deviation map compares RNFL measurements of individual pixels in the map with a database of normal RNFL measurements collected from healthy eyes.

1.4.4 Optical coherence tomography

Optical coherence tomography (OCT) was first introduced in 1991 by a team in Massachusetts Institute of Technology (MIT) headed by Fujimoto for noninvasive cross-sectional imaging in biological systems (Huang et al., 1991). Two dimensional grayscale OCT images representing the reflectivity of different structures of the retina were illustrated, where high reflective structures such as the RNFL and the retinal pigment epithelium were displayed in bright signal intensity whereas low reflective structures such as the subretinal fluid and the vitreous were displayed in low signal intensity. Based on the unique reflectivity in each layer of the retina, different layers can be segmented and the RNFL thickness can be quantified. The basic principal of optical coherence tomography is based on low coherence interferometry which makes use of the interference of two light beams split up from a common light source by a beam splitter. One light beam is directed to the sample, another one is directed to a reference mirror. The backscattered and back-reflected signals are then recombined through the beam splitter and received by a detector. Since interference only occurs when the two beams are matched in traveling distance, the location and depth of interfaces within sample can be determined by detection of the various interference envelop peaks. Multiple longitudinal scans at a series of lateral locations are performed to provide a two dimensional image of the reflection sites in the sample analogous to

ultrasound B scan imaging. Similarly, three dimensional image can be obtained by repeating the multiple longitudinal scanning operation in another dimension.

Currently, there are two types of OCT systems, known as time-domain OCT (TD-OCT) and spectral-domain OCT (SD-OCT). The one introduced by the MIT team headed by Fujimoto in 1991 is a TD-OCT. The first SD-OCT is introduced in 1995 (Fercher et. at, 1995) and the first demonstration of in vivo imaging was published in 2002 (Wojtkowski et al., 2002). The major difference between TD-OCT and SD-OCT is the method in acquiring a longitudinal scan. In TD-OCT, longitudinal scanning is performed by moving the reference mirror over a distance equal to the interested depth range. In SD-OCT, there are currently two systems of image acquisition. One system is called spectrometer-based SD-OCT, also known as Fourier domain OCT. In Fourier domain OCT, the reference mirror is immobilized, interferometric signal is detected by a low-loss spectrometer to measure the spectral oscillations. The other system is called swept-source SD-OCT, it uses a rapidly tunable narrowband laser with immobilized reference mirror to measure the spectral oscillations generated by the swept source. Yaqoob et al. have proved that spectrometer-based SD-OCT can provide a better signal-to-noise ratio (SNR) than TD-OCT with the same acquiring time, with a difference of $10 \log_{10}(N/2)$, where N is the number of detector elements in the spectrometer (Yaqoob et al., 2005).

The first commercialized TD-OCT was introduced in 1995. TD-OCT has undergone generations of changes from OCT 1, OCT 200, to Stratus OCT (Carl Zeiss Meditec). The time-domain OCT technology allows the Stratus OCT to acquire 400 A-scans per second. SD-OCT has become the current standard for optic disc and retina imaging because of the increased scan speed and improved image resolution. A number of SD-OCT models are available in the market. These include the Cirrus HD-OCT (Carl Zeiss Meditec, Dublin, California) with a scan speed of 27,000 A-scans per second, Spectralis OCT (Heidelberg Engineering, GmbH, Heidelberg, Germany) with a scan speed of 40,000 A-scans per second, 3D-OCT (Topcon Corporation, Tokyo, Japan) with a scan speed of 20,000 A-scans per second, RTVue (Optovue, Inc, Fremont, CA, USA) with a scan speed of 26,000 A-scans per second, 3D SD OCT (Bioptigen, Inc, Research Triangle Park, North Carolina) with a scan speed of 20,000 A-scans per second, SOCT Copernicus HR (Optopol Technology, SA, Zawiercie, Poland) with a scan speed of 52,000 A-scans per second and OCT/SLO (Ophthalmic Technologies Inc, OTI, Toronto, Ontario) with a scan speed of 27,000 A-scans per second. The scan speed of the spectral-domain OCT ranges between 20,000 A-scans per second and 52,000 A-scans per second and the axial resolution of is approximately 5 μ m.

Extensive research investigating the reproducibility of RNFL and optic disc measurements has been reported across different generations of

OCT. The reproducibility of the first generation OCT (OCT 1, Carl Zeiss Meditec) was reported by Schuman et al. (Schuman et al., 1996). The study evaluated the intraclass correlation coefficients (ICCs) of the average RNFL thickness measurement based on different diameters of scan circles at the optic disc from 10 glaucoma and 11 control subjects. The scan circle of 3.4 mm diameter centered at the optic disc center was found to have highest ICCs among the tested scan circle diameters. The ICCs for the 10 glaucoma and 11 control subjects were 0.52 and 0.56, respectively (Schuman et al., 1996). The reliabilities were only moderate. With the improvement in OCT technology, the reliability of OCT has been improved dramatically. Good to adequate reliability with ICCs of 0.79 - 0.98 has been reported in the average RNFL thickness measured by the Stratus OCT (Carl Zeiss Meditec) for both glaucoma and normal subjects with both standard and fast scan protocols (Paunescu et al., 2004, Budenz et al., 2005, Budenz et al., 2008 Leung et al., 2008). High reliability of RNFL measurement has also been reported in many SD-OCT devices. Vizzeri et al. reported good reliability for Cirrus HD-OCT (Carl Zeiss Meditec, Dublin, California) RNFL measurements with ICCs of 0.98 and 0.96 in glaucomatous and healthy eyes, respectively (Vizzeri et al., 2009). Langenegger et al., reported an ICC of 0.99 for the average RNFL thickness in both glaucoma and normal groups using the Spectralis OCT (Heidelberg Engineering, GmbH, Heidelberg, Germany) (Langenegger et al., 2011). For the 3D-

OCT (Topcon Corporation, Tokyo, Japan), Menke et al. showed the ICCs of average RNFL thickness measured with scan circle of 3.0 mm and 6.0 mm diameters were 0.94 - 0.96 (Menke et al., 2008). González-García et al. reported the ICCs of average RNFL thickness measurement of RTVue (Optovue, Inc, Fremont, CA, USA) were 0.97 in both glaucoma and normal subjects (González-García et al., 2009). The reliability of OCT/SLO (Ophthalmic Technologies Inc, OTI, Toronto, Ontario) was investigated by Hong et al., who reported the intra-session ICCs of the average RNFL thickness were 0.97 and the inter-session ICCs were 0.96 in both the independent and guided re-test scanning modes (Hong et al., 2012).

Many studies have shown that OCT has good diagnostic performance for glaucoma. Medeiros et al. had reported that the average RNFL thickness obtained by Stratus OCT had an area under the receiver operating characteristic curve (AUC) of 0.91 in 75 glaucoma and 66 healthy subjects, which was not significantly difference from those obtained with the HRT and GDx VCC. The average RNFL thickness obtained by Stratus OCT had a sensitivity of 71% with a specificity of 95% and a sensitivity of 84% with a specificity of 80% (Medeiros et al., 2004). Using an average RNFL thickness < the 5th percentile of the RNFL thickness from the reference database for glaucoma diagnosis, a sensitivity of 84% with a specificity of 98% have been reported (Budenz et al., 2005). Large AUC for the average RNFL thickness measurement

(0.952 - 0.978) to discriminate glaucomatous from normal eyes has also been reported using the SD-OCT (Leung et al., 2010, Wu et al., 2012).

1.5 Monitoring Glaucoma Progression

Monitoring glaucoma progression is essential to guide treatment in glaucoma patients. Visual field testing has been a key strategy to follow glaucoma progression and most clinical trials in glaucoma treatment used visual field changes as an outcome measure.

1.5.1 Visual Field Progression

1.5.1.1 Event analysis

In the Advanced Glaucoma Intervention Study (AGIS), a visual field scoring system was developed with reference to the threshold values in the total deviation map provided in the Humphrey 24-2 printout. The visual field was divided into three partitions: the nasal, the superior and the inferior hemifields. In the superior and the inferior hemifields, scores were given separately based on the number of clusters with three or more contiguous depressed points with at least one test location depressed ≥ 12 dB. Clusters of 3-5 points, 6-12 points, 13-20 points and >20 points were given a score from 1 to 4, respectively. For a cluster with at least half of its points depressed by ≥ 12 dB, ≥ 16 dB, ≥ 20 dB, ≥ 24 dB or ≥ 28 dB, a score from 1 to 5 was added, respectively. The score on each hemifield was bounded by 9. In the nasal field, occurrence of a cluster of three or more contiguous depressed points that may cross the

horizontal midline or a cluster of one or more depressed points that did not cross the horizontal midline was given a score of 1. If more than half of the nasal test locations were depressed ≥ 12 dB, a score of 2 was given. A total score ranged from 0 (normal) to 20 (severe visual field loss) was assigned to a visual field. Progression was defined when the visual field score increased by 4 or more and confirmed with 2 consecutive tests. (AGIS investigators, 1994a, AGIS investigators, 1994b)

The Collaborative Initial Glaucoma Treatment Study (CIGTS) is another major clinical trial examining 607 subjects with open-angle glaucoma enrolled at 14 clinical centers in the United States. It used a scoring system based on the total deviation probability plot in the Humphrey 24-2 printout. A test location was defined as a defective point when a probability $\leq 5\%$ was observed in the corresponding location in the total deviation probability plot with at least two adjacent defective points on the sides or corners. The minimum defect was defined as the maximum probability value in the total deviation plot at the given defective point and two most defective neighboring points. A score would be given according to the minimum defect. 1 for a minimum defect $\leq 5\%$, 2 for a minimum defect $\leq 2\%$, 3 for a minimum defect $\leq 1\%$ and 4 for a minimum defect $\leq 0.5\%$. Scores of all the test locations, except for the two test location near to the blind spot, were summed and rescaled (dividing by 10.4) to a range between 0 (no defect) to 20 (all points showing a defect

at 0.5% level of significant). Progression was defined when a score increased by 3 or more and confirmed with two consecutive examinations. (Musch et al., 1999)

In the Early Manifest Glaucoma Trial (EMGT), visual field progression at a test location was defined when the change in visual sensitivity was outside the 95% test-retest variability in the pattern deviation plot, and confirmed with two consecutive tests. An eye was considered to have visual field progression when 3 or more test locations (Leske et al., 1999) had evidence of change.

A study conducted by Heijl et al. (Heijl et al., 2008) shown that the three visual field progression detection criteria (AGIS, CIGTS and EMGT criteria) had a sensitivity of 58%, 75% and 96% and a specificity of 98%, 99% and 89%, respectively. The agreement between the three criteria was only moderate.

1.5.1.2 Trend analysis

Although event analysis is a more popular approach to evaluate glaucoma progression, trend analysis is useful to examine the rate of progression. Linear regression is the most commonly used regression model in modeling glaucoma progression. There are studies suggesting that linear regression provide adequate fit to glaucoma visual field progression (Mikelberg et al., 1986, McNaught et al., 1995, Bengtsson et al., 2009). Mean deviation (MD) has been a commonly used index to

assess the overall severity of visual field damage. A population-based study based on 1066 OAG subjects estimated that the mean progression of visual field in decibels per year was -1.12 dB/year, -1.26 dB/year, -1.33 dB/year and -1.56 dB/year in European, Hispanic, African, and Chinese, respectively. There were no without significant differences between ethnicities (Broman et al., 2008). A study conducted by Heijl et al. reported significant differences in the median rates of MD loss between normal, high-tension glaucoma (HTG), normal-tension glaucoma (NTG) and pseudoexfoliation glaucoma (PEXG) subjects. The median rates of MD loss were -0.40 dB/year overall, and -0.46 dB/year, -0.22 dB/year and -1.13 dB/year in the HTG, NTG and PEXG groups, respectively (Heijl et al., 2009). However, MD can be affected by the presence of media opacity (e.g. cataract). The visual field index (VFI) is an age-corrected index introduced by Bengtsson and Heijl (Bengtsson & Heijl, 2008) quantifying the percentage of visual field preserved. It has been shown that VFI is less likely to be affected by media opacity compared with MD (Bengtsson & Heijl, 2008, Rao et al., 2013). Artes et al. investigated the relationship between MD and VFI in 109 glaucoma subjects and reported the mean rates of change in MD and VFI were -0.27 dB/year and -0.26 %/year, respectively. There was a strong correlation between the rates of change of MD and VFI (Spearman's correlation coefficient of 0.79) (Artes et al., 2011).

In addition to evaluating global change in visual field indices such as MD and VFI, the point-wise linear regression analysis (PLR) (Progressor, OBF Laboratories UK Ltd, Wiltshire, UK) can provide linear regression analysis on individual test locations. It has been shown that the mean rate of change of localized threshold sensitivities in glaucomatous eyes vary from -0.84 dB/year to -5.84 dB/year (Smith et al., 1996, Katz et al., 1997). Therefore, the rate of change of localized threshold sensitivity \leq -1.00 dB/year is usually considered clinically meaningful in glaucoma monitoring. While most studies on PLR were based on linear regression, Caprioli et al. suggested that exponential regression may provide better fit than linear regression for modeling progression of the differential luminance sensitivities at individual test locations (Caprioli et al., 2011).

1.5.2 Optic Disc and RNFL Progression

1.5.2.1 Confocal scanning laser ophthalmoscopy

Topographic Change Analysis (TCA) is a statistical technique introduced by Chauhan (Chauhan et al., 2000) for detecting surface topographic changes in the optic disc with the confocal scanning laser ophthalmoscope (cSLO), Heidelberg Retina Tomograph, (HRT; Heidelberg Engineering, GmbH, Heidelberg, Germany). The HRT image consists of 256x256 pixels (10 μ m/pixel) of topographic height values in the optic disc region. In the TCA, images are divided into arrays of 64x64 superpixels (1 superpixel =4x4 pixels). A nested three-

way analysis of variance (ANOVA) accounted for the effects of topograph scan variability, scan time and the location of the height measurements is applied to compare the baseline and follow-up topographic height values on each superpixel. A significant change is defined as a difference in surface height between the follow-up and the baseline examinations greater than the test-retest variability calculated from the three baseline examinations (Chauhan et al., 2000).

A computer simulation study by Chauhan et al. (Chauhan et al., 2000) suggested that the TCA has an adequate level of sensitivity to detect changes ≥ 2 standard deviation (SD) of topographic height in the optic disc with a high level of specificity. Progression detected by the TCA is also found to be predictive of subsequent visual field progression (Chauhan et al., 2009b). However, a longitudinal study of 77 subjects with early glaucomatous visual field damage showed that only 29% of eyes detected with progression by TCA had also progression detected by the pattern deviation probability plot in SAP. There was a poor agreement between the changes detected by TCA and SAP (Chauhan et al., 2001). Likewise, the agreement of optic disc changes detected by TCA and optic disc photography was poor (Chauhan et al., 2009a, O'Leary et al., 2010).

A statistical image mapping (SIM) approach has been investigated by Patterson et al. SIM is generated by performing pixel-by-pixel analysis of topographic height changes over time using permutation testing at 5%

level of significance. Clusters of contiguous pixels were analyzed through permutation testing by shuffling the images many times. SIM has been shown to have superior performance in detecting change compared with TCA in computer simulation. It has been further confirmed by a longitudinal study following 20 normal and 30 ocular hypertensive subjects. SIM detected a higher proportion of optic disc changes (73%) in ocular hypertensive subjects and a lower proportion of optic disc changes (10%) in normal subjects than TCA (53% and 15%, respectively). (Patterson et al., 2005)

1.5.2.2 Scanning laser polarimetry

The advent of Guided Progression Analysis in GDx VCC and ECC (Carl Zeiss Meditec, Dublin, California) has facilitated detection of progressive RNFL thickness. GPA analyzes RNFL thickness changes in a map with event analysis and performs linear regression analysis of average, superior and inferior RNFL thicknesses. For the map analysis, RNFL thickness measurements in the 4.2x4.2 mm² area at the optic disc region are analyzed. The RNFL thicknesses were compared between the follow-up and the two baseline examinations pixel-by-pixel. There are two different modes of GPA: Fast Mode and Extended Mode. In the Fast Mode, test-retest variability is estimated based on a reference population. In the Extended Mode, the test-retest variability is estimated by the within-subject variability calculated from three baseline images. "Possible progression" of RNFL thickness at individual pixel is

highlighted in yellow, which signifies that the reduction in RNFL thickness between the baseline and the follow-up examination exceeds the test-retest variability of that particular pixel. When the change is confirmed by a consecutive examinations, "Likely progression" is noted and the pixel would be highlighted in red. On the other hand, an increase in RNFL thickness is denoted as "Possible increase" and highlighted in purple when the difference between the baseline and the follow-up examinations exceed the test-retest variability.

A longitudinal study of 431 glaucoma and glaucoma suspect eyes using the Fast Mode GPA in GDxVCC reported that 50% of eyes with progression detected by SAP or optic disc photographs were detected by GPA with a specificity $\geq 96\%$. However, the agreement between the progression detected by GPA and the two standard techniques is only moderate (Agreement Coefficient AC1: 0.44, 95% confidence interval: 0.28 - 0.61) (Alencar et al., 2010). In addition, although the same GPA is available in both GDxVCC and GDxECC, the agreement between the Fast Mode GPA in the two corneal compensation techniques (kappa: 0.41- 0.57) is only moderate (Grewal et. al, 2011).

1.5.2.3 Optical coherence tomography

The first longitudinal study investigating the progressive changes of RNFL thickness measured by OCT was conducted by Wollstein et al. (Wollstein et al., 2005). They investigated 64 eyes of 37 glaucoma and

glaucoma suspect subjects with a median follow-up of 4.7 years. The study reported that the mean rates of change in the average RNFL thickness were $-2.56 \mu\text{m}/\text{year}$ and $-2.21 \mu\text{m}/\text{year}$ in glaucoma suspects and glaucomatous eyes, respectively. There were no significant differences in the rates of change between the groups. By defining OCT RNFL progression as a reduction in average RNFL thickness of at least $20 \mu\text{m}$ and visual field progression as a reduction in MD of at least 2 dB, 22% of eyes were detected to have progression by OCT, 9% of eyes were detected to have progression by visual field, with 3% of eyes were detected to have progression by both techniques (Wollstein et al., 2005).

Lee et al. compared the rates of change of RNFL thickness measured by OCT between 76 progressors and 77 non-progressors (based on the evaluation of serial red-free RNFL photographs) with localized RNFL defects (Lee et al., 2011). They found that the rate of change in affected clock-hour sectors had the highest discrimination power to separate progressive eyes from non-progressive eyes, which reported a sensitivity of 62% with specificity of $\geq 80\%$. Comparatively, the rate of change of average RNFL thickness only provided a discrimination ability between progressors and non-progressors with a sensitivity of 32% and a specificity of $\geq 80\%$ (Lee et al., 2011). Both the global and sectoral RNFL thickness are important parameters in monitoring glaucoma progression.

In the Cirrus HD-OCT (Carl Zeiss Meditec, Dublin, California), progressive RNFL changes can be analyzed in a map using the Guided Progression Analysis (GPA). The RNFL thickness map is compared of 200x200 pixels, representing RNFL measurements in a 6x6 mm² optic disc region. The RNFL thicknesses between the two baseline and the follow-up examination are compared pixel-by-pixel. Possible RNFL thickness progression at individual pixel in the RNFL thickness map is defined when the difference between the two baseline and the follow-up examination exceeds the test-retest variability of that particular pixel. The test-retest variability is estimated based on a reference database. Likely progression is defined when the change is confirmed in the consecutive follow-up examinations. "Likely Loss", "Possible Loss", and "Possible Increase" are highlighted in red, yellow and purple, respectively.

A longitudinal study analyzing serial changes of the RNFL change maps showed that widening of RNFL defects was the most common pattern of RNFL progression (85.7% of all eyes with RNFL progression detected), whereas deepening of RNFL defects was found in 7.1% of eyes, and development of new RNFL defects was found in 17.9%. However, among those eyes with RNFL progression detected by GPA, only 46.4% had visual field progression detected by SAP (Leung et al., 2012).

1.6 Statistical Methods of Progression Analysis

Event-based and trend-based analyses are the two key fundamental approaches for detection of change in disease progression. In the following sessions, the statistical basis of event-based and trend-based analyses and different mathematical models for detection of change are reviewed.

1.6.1 Event-based Analysis

Event-based analysis (EA) refers to the statistical analysis that detects change that exceeds a certain specific threshold compared with the baseline examination. The threshold is commonly computed based on the subject-specific test-retest reliability. Commercially available statistical packages are available for detection of change in glaucoma based on EA. These include the Progression Analysis Probability Plot in the Humphrey Field Analyzer (HFA, Carl Zeiss Meditec, Dublin, California), the TCA provided by HRT (Heidelberg Engineering, GmbH, Heidelberg, Germany), the RNFL thickness change analysis in the GDxVCC (Carl Zeiss Meditec, Dublin, California), GDxECC (Carl Zeiss Meditec) and Cirrus HD-OCT (Carl Zeiss Meditec). On the other hand, there are event analysis using an arbitrary threshold obtained by empirical data has been applied in clinical trials of glaucoma treatment. These include the visual field scoring system developed by the Advanced Glaucoma Intervention Study (AGIS) (AGIS investigators,

1994a) and the Collaborative Initial Glaucoma Treatment Study (CIGTS) (Musch et al., 1999), and the progression detection defined by the Early Manifest Glaucoma Trial (EMGT) (Leske et al., 1999).

1.6.1.1 Event-based analysis using empirical threshold

The statistical basis of event analysis is outlined as follow. Let Y_{it} denotes the measurement of interest for eye i at time t . To compare the baseline measurement at time 0 with the follow-up measurement at time t , the difference $D_{it} = (Y_{it} - Y_{i0})$ is calculated. Using an empirical threshold, D_{it} for all eyes, $i = 1, \dots, n$, can be calculated and arranged in order. Let $D_{(1)t} \leq D_{(2)t} \leq \dots \leq D_{(n)t}$ be the ordered difference obtained from n healthy normal eyes. Assuming the empirical distribution is the same as the population distribution, the probability of the difference between the baseline and follow-up measurements of a normal eye j that is smaller than or equal to $D_{(k)t}$, $P(D_{jt} \leq D_{(k)t})$, equals to k/n .

Using $D_{(k)t}$ as the empirical threshold to detect change, progression can be defined for eye j if $D_{jt} \leq D_{(k)t}$, and the specificity would be $(1 - \frac{k}{n}) \times 100\%$. The sensitivity can be estimated by the percentage of glaucoma progression detected by the empirical threshold from a sample of progressive glaucomatous eyes defined by a reference standard.

Although the empirical distribution is not likely to be the same as the population distribution, based on empirical theory, it will converge to the

population distribution as the sample size increases. Therefore, the use of empirical threshold is suitable for population based studies.

1.6.1.2 Event-based analysis using statistical threshold

The test-retest reliability of the measurement Y_{it} is assumed to follow a certain independent and identical distribution for eye i at time t . With an independent and identical normal distribution with a mean of μ_{it} and a variance of σ_i^2 , denoted by $Y_{it} \sim N(\mu_{it}, \sigma_i^2)$, the difference $D_{it} = (Y_{it} - Y_{i0})$ would also follow a normal distribution with a mean of $\mu_{it} - \mu_{i0}$ and a variance $2\sigma_i^2$, $D_{it} \sim N(\mu_{it} - \mu_{i0}, 2\sigma_i^2)$. By setting the statistical threshold

as $-z_\alpha \sqrt{2\sigma_i^2}$, where z_α is the critical value satisfying $\Phi(-z_\alpha) = \alpha$ and

$\Phi(\cdot)$ denotes the cumulative distribution function of standard normal

distribution, progression can be defined if $D_{it} \leq -z_\alpha \sqrt{2\sigma_i^2}$. The

specificity would be $[1 - \Phi(-z_\alpha)] \times 100\% = (1 - \alpha) \times 100\%$ and the

sensitivity would be $P\left(D_{it} < -z_\alpha \sqrt{2\sigma_i^2} \mid \mu_{it} < \mu_{i0}\right) = \Phi\left(-z_\alpha - \frac{\mu_{it} - \mu_{i0}}{\sqrt{2\sigma_i^2}}\right)$.

σ_i^2 can be estimated by the sample variance $\hat{\sigma}_i^2$ obtained by collecting multiple examinations in the baseline visit. This is eye-specific test-retest variability. For EA using test-retest variability derived from a group of subjects, it is then assumed that all eyes share a similar test-retest reliability (i.e. $\sigma_i^2 = \sigma^2$). Then, σ^2 can be estimated by the mean of $\hat{\sigma}_i^2$ from a sample of normal eyes. The calculation does not require

estimation of the individual variance so that progression can be detected with only one baseline and one follow-up examinations.

1.6.2 Trend-based Analysis

Trend-based analysis (TA) refers to regression analysis that models change of the parameter of interest over time. Linear regression is the most commonly used regression model in modeling glaucoma progression. Examples of commercially available statistical packages based on trend-based analysis include linear regression analysis of mean deviation (MD) and visual field index (VFI) in the Humphrey Field Analyzer (Carl Zeiss Meditec, Dublin, California), point-wise linear regression analysis (PLR) on individual test locations provided by the Progressor (OBF Laboratories UK Ltd, Wiltshire, UK) and linear regression analysis of RNFL thickness measurements in the Guided Progression Analysis (GPA, Carl Zeiss Meditec, Dublin, California) in GDxVCC (Carl Zeiss Meditec), GDxECC (Carl Zeiss Meditec), Stratus OCT (Carl Zeiss Meditec) and Cirrus HD-OCT (Carl Zeiss Meditec).

1.6.2.1 Simple linear model

The statistical basis of linear modeling is outlined as follow. Let Y_{it} denotes the measurement of interest for eye i at time t which follows a normal distribution with a mean of μ_{it} and a variance of σ_i^2 , denoted by $Y_{it} \sim N(\mu_{it}, \sigma_i^2)$. With simple linear modeling, $\mu_{it} = \beta_{0,i} + \beta_{1,i}t$, progression is defined if the estimation of slope $\beta_{1,i}$ is significantly less than zero.

The function, $\mu_{it} = \beta_{0,i} + \beta_{1,i}t$, is known as the link function which specify the relationship between the covariate(s) and mean of the response variables. For measurements obtained at t_1, t_2, \dots, t_n , the least squares estimator of $\beta_{1,i}$ is given by $\hat{\beta}_{1,i} = \frac{\sum_{k=1}^n (t_k - \bar{t})(Y_{ik} - \bar{Y}_i)}{\sum_{k=1}^n (t_k - \bar{t})^2}$ which follows the normal distribution with mean $\beta_{1,i}$ and variance $\sigma_{\hat{\beta}_{1,i}}^2$, $N(\beta_{1,i}, \sigma_{\hat{\beta}_{1,i}}^2)$, where $\bar{t} = \frac{1}{n} \sum_{k=1}^n t_k$ and $\bar{Y}_i = \frac{1}{n} \sum_{k=1}^n Y_{ik}$. The least squares estimator of $\beta_{0,i}$ would be given by $\hat{\beta}_{0,i} = \bar{Y}_i - \hat{\beta}_{1,i} \bar{t}$, which follows a normal distribution with mean $\beta_{0,i}$ and variance $\sigma_{\hat{\beta}_{0,i}}^2$, $N(\beta_{0,i}, \sigma_{\hat{\beta}_{0,i}}^2)$. Progression can be defined if $\hat{\beta}_{1,i} < -z_\alpha \sigma_{\hat{\beta}_{1,i}}$ with a specificity of $(1 - \alpha) \times 100\%$, where z_α is the upper $\alpha \times 100\%$ critical value of the standard normal distribution. The sensitivity would be $P(\hat{\beta}_{1,i} < -z_\alpha \sigma_{\hat{\beta}_{1,i}} | \beta_{1,i}) = \Phi\left(-z_\alpha - \frac{\beta_{1,i}}{\sigma_{\hat{\beta}_{1,i}}}\right)$. If the pattern of progression is exponential, $\mu_{it} = \beta_{0,i} e^{\beta_{1,i}t}$, by assuming the response variable follow a lognormal distribution (i.e. $\log_e Y_{it} \sim N(\log_e \mu_{it}, \sigma_i^2)$), a linear regression model can be fitted into the logarithm transformed data.

1.6.2.2 Multiple linear model

Linear modeling can also take into account multiple covariates (e.g. age and IOP for evaluation of glaucoma progression) to refine the model fitting. This can be performed by modeling the means of the response variables by a linear combination of the covariates, $\mu_{it} = \beta_{0,i} + \beta_{1,i}X_{1,it} +$

$\beta_{2,i}X_{2,it} + \dots + \beta_{k,i}X_{k,it}$, where $(1, X_{1,it}, X_{2,it}, \dots, X_{k,it})$ and $(\beta_{0,i}, \dots, \beta_{k,i})$ represent the covariates and the corresponding coefficients, respectively. Under independent and identical normal distribution assumption $Y_{it} \sim N(\mu_{it}, \sigma_i^2)$, the vector $\tilde{\beta} = (\beta_{0,i}, \dots, \beta_{k,i})$ can be estimated by the maximum likelihood estimator which follows an asymptotically normal distribution with a mean $\tilde{\beta}$ and variance $I(\beta)^{-1}$, where $I(\beta) = -E \left[\frac{\partial^2}{\partial \beta^2} \log_e f(\tilde{X}, \tilde{Y} | \tilde{\beta}) | \tilde{\beta} \right]$ is the Fisher information matrix and $f(\tilde{X}, \tilde{Y} | \tilde{\beta})$ is the likelihood function of the whole sample. Each coefficient can be tested by Wald test or likelihood ratio test and progression can be detected.

1.6.3 Advanced Regression Analysis

There is an increasing trend of using linear mixed model to evaluate progression in glaucoma. Longitudinal studies conducted by Leung et al. (Leung et al., 2012) and Rao et al. (Rao et al., 2013) have used linear mixed model to report age-related change in RNFL measurements in normal eyes. Their studies suggest that the identification of glaucomatous progression should take consideration of age-related change. O'Leary et al. (O'Leary et al., 2012) compared the rates of change of RNFL thickness and visual field mean deviation between normal and glaucoma eyes by linear mixed model. Significant differences were only found in the rates of visual field mean deviation but not in RNFL thickness. This result might be due to the inclusion of

both progressing and non-progressing glaucoma eyes in the analysis. By contrast, a number of studies have shown that the rates of change of RNFL measurements between progressing and non-progressing glaucoma eyes were significantly different, in which stereoscopic photography, red-free RNFL photographs and visual field were adopted as the reference standard (Medeiros et al., 2009a, Medeiros et al., 2009b, Alencar et al., 2010, Na et al., 2013). All these studies were analyzed using linear mixed model.

Although linear regression is the most common model to examine glaucoma progression, glaucoma progression may not always be linear. There is evidence suggesting that faster rate of progression in RNFL thickness is associated with thicker baseline RNFL thickness (Medeiros et al., 2009, Leung et al., 2010, Leung et al., 2012). Autoregressive (AR) model, which regresses current response on previous responses, might provide a useful alternative to model such nonlinearity. In 1999, Rahiala (Rahiala, 1999) introduced an extension of autoregressive model to generalize the variation among individuals in a similar manner as in LMM. However, autoregressive model is not commonly used in biomedical research and has not been reported in glaucoma study.

1.6.3.1 Linear mixed model

Given a collection of longitudinal data from a group of n independent eyes such that each eye follows a linear model:

$$Y_{it} = \beta_{0,i} + \beta_{1,i}X_{1,it} + \beta_{2,i}X_{2,it} + \cdots + \beta_{k,i}X_{k,it} + \varepsilon_{it}$$

where Y_{it} represents the response variable for eye i at time t , $(1, X_{1,it}, X_{2,it}, \dots, X_{k,it})$ and $(\beta_{0,i}, \dots, \beta_{k,i})$ represent the covariates and the corresponding coefficients, respectively, and ε_{it} represents the random residual error. The collection of linear models can be grouped together to form a linear mixed model (LMM), which is expressed by

$$Y_{it} = \beta_0 + \beta_1 X_{1,it} + \cdots + \beta_k X_{k,it} \\ + u_{0,i} + u_{1,i} X_{1,it} + u_{2,i} X_{2,it} + \cdots + u_{k,i} X_{k,it} + \varepsilon_{it}$$

where $(\beta_0, \dots, \beta_k)$ and $(u_{0,i}, \dots, u_{k,i})$ represent the fixed overall and random individual effects of the covariates $(1, X_{1,it}, \dots, X_{k,it})$, respectively. It can be expressed in a matrix form:

$$\tilde{Y}_i = \tilde{X}_i \tilde{\beta} + \tilde{X}_i \tilde{u}_i + \tilde{\varepsilon}_i$$

where $\tilde{Y}_i = (Y_{it_{i,1}}, \dots, Y_{it_{i,m(i)}})^T$, $\tilde{\varepsilon}_i = (\varepsilon_{it_{i,1}}, \dots, \varepsilon_{it_{i,m(i)}})^T$,

$\tilde{X}_i = (\tilde{X}_{it_{i,1}}, \dots, \tilde{X}_{it_{i,m(i)}})^T$, $\tilde{X}_{it} = (1, X_{1,it}, \dots, X_{k,it})$, $\tilde{\beta} = (\beta_0, \dots, \beta_k)^T$ and

$\tilde{u}_i = (u_{0,i}, \dots, u_{k,i})^T$.

It is commonly assumed that $\tilde{u}_i \sim N(\tilde{0}, \Sigma_u)$ and $\tilde{\varepsilon}_i \sim N(0, \sigma^2 I)$ are independent. To avoid singularity of Σ_u and non-free coefficient in $\tilde{\beta}$, consider $\tilde{u}_i = W \tilde{v}_i$ and $\tilde{\beta} = D \tilde{b}$ where W is a $(k \times w)$ matrix with rank w ,

$\tilde{v}_i \sim N(\tilde{0}, \Sigma_v)$, D is a $(k \times d)$ matrix with rank d and \tilde{b} is a d -dimensional vector. The model can be rewritten as

$$\tilde{Y}_i = \tilde{X}_i \tilde{b} + \tilde{Z}_i \tilde{v}_i + \tilde{\varepsilon}_i$$

where $\tilde{X}_i = \tilde{X}_i D$ and $\tilde{Z}_i = \tilde{X}_i W$.

The likelihood function, $L(\tilde{b}, \Sigma_v)$, for the whole sample is proportional to

$$\prod_{i=1}^n |V_i|^{-\frac{1}{2}} \times \exp \left\{ \frac{1}{2} (\tilde{Y}_i - \tilde{X}_i \tilde{b})^T V_i^{-1} (\tilde{Y}_i - \tilde{X}_i \tilde{b}) \right\}$$

where $V_i = \tilde{Z}_i \Sigma_v \tilde{Z}_i^T + \sigma^2 I$. The maximum likelihood estimator (MLE) of \tilde{b} conditional on V_i is given by

$$\hat{b}_{mle} = \left[\sum_{i=1}^n \tilde{X}_i^T V_i^{-1} \tilde{X}_i \right]^{-1} \left[\sum_{i=1}^n \tilde{X}_i^T V_i^{-1} \tilde{Y}_i \right]$$

and the MLE of V_i , \hat{V}_{mle} , can be obtained by maximizing the likelihood function with \tilde{b} replaced by \hat{b}_{mle} . This pair of MLE, $(\hat{b}_{mle}, \hat{V}_{mle})$, simultaneously maximizes the likelihood function, $L(\tilde{b}, \Sigma_v)$ (Laird & Ware, 1982). Based on the properties of MLE, any fixed coefficient \tilde{b} can be tested by Wald test or likelihood ratio test (LRT). Existence of any random coefficient can be tested by linear combination of LRT with different degrees of freedom as described by Self & Liang (Self & Liang, 1987).

Using Bayesian techniques, eye-specific coefficients \tilde{v}_i given \tilde{Y}_i for eye i can be predicted by the posterior mean of \tilde{v}_i , which is given by

$$\hat{v}_i = E[\tilde{v}_i | \tilde{Y}_i] = \Sigma_v \tilde{Z}_i^T V_i^{-1} (\tilde{Y}_i - \tilde{X}_i \tilde{b})$$

with variance-covariance matrix

$$\text{Var}(\hat{v}_i) = \Sigma_v \tilde{Z}_i^T \left\{ V_i^{-1} - V_i^{-1} \tilde{X}_i \left(\sum_{i=1}^n \tilde{X}_i^T V_i^{-1} \tilde{X}_i \right)^{-1} \tilde{X}_i^T V_i^{-1} \right\} \tilde{Z}_i \Sigma_v$$

(Laird & Ware, 1982).

This predictor is called the best linear unbiased predictor (BLUP). It is 'linear' because it is a linear function of \tilde{Y}_i , and 'unbiased' because the expectation of the prediction is equal to the true coefficients \tilde{v}_i . Among all the linear unbiased predictors, it is the 'best' in that its variance is minimal. The unknown parameters (\tilde{b}, Σ_v) in BLUP can be replaced by the MLE of (\tilde{b}, Σ_v) to perform the prediction, such predictor is called an empirical best linear unbiased predictor (EBLUP).

Since the two eyes of any individual are likely to be associated, a nested design LMM can be fitted to model data obtained from both eyes. The nested design LMM can be formulated as follow:

$$\tilde{Y}_{ij} = \tilde{X}_{ij} \tilde{b} + \tilde{Z}_{ij} \tilde{v}_i + \tilde{Z}_{ij}^* \tilde{v}_{ij}^* + \tilde{\varepsilon}_{ij}$$

where \tilde{Y}_{ij} is the vector of responses for individual i and eye j , \tilde{b} is the vector of fixed effect coefficients corresponding to the covariate matrix

\tilde{X}_{ij} , \tilde{v}_i represents the vector of random effect coefficients nested within the same individual i corresponding to the covariate matrix \tilde{Z}_{ij} , \tilde{v}_{ij}^* represents the vector of random effect coefficients nested within the same eye j from the same subject i corresponding to the covariate matrix \tilde{Z}_{ij}^* , and $\tilde{\varepsilon}_{ij}$ is the vector of residual errors.

Assuming $\tilde{v}_i \sim N(\tilde{0}, \Sigma_v)$, $\tilde{v}_{ij}^* \sim N(\tilde{0}, \Sigma_{v^*})$ and $\tilde{\varepsilon}_{ij} \sim N(0, \sigma^2 I)$ are independent, the model parameters can be estimated by MLE, random coefficients can be predicted by EBLUP derived from above.

Using LMM to regress a collection of longitudinal measurements on time, the eye-specific rate of progression can be predicted by EBLUP and progression can be defined based on Wald test.

1.6.3.2 Autoregressive model

In linear and linear mixed models, responses are regressed on a set of covariates measured at the same time points as the responses. For example, to model the longitudinal change of a response over time for eye i , a simple linear regression with link function, $\mu_{it} = \beta_{0,i} + \beta_{1,i}t$, can be applied. The link function is a deterministic function; if $\beta_{0,i}$ and $\beta_{1,i}$ are known, prediction can be made regardless of the historical records of the response Y_{it^-} for all $t^- < t$. Therefore, linear model and linear mixed model are difficult to address the relevance of historical data to subsequent changes. Comparatively, an autoregressive (AR) model,

which regresses a time series of responses on the previous responses, may be a more useful approach. It can be expressed as:

$$Y_{it} = \rho_{1,i}Y_{i(t-1)} + \rho_{2,i}Y_{i(t-2)} + \cdots + \rho_{s,i}Y_{i(t-s)} \\ + \beta_{0,i} + \beta_{1,i}X_{1,it} + \beta_{2,i}X_{2,it} + \cdots + \beta_{k,i}X_{k,it} + \varepsilon_{it}$$

where $(\rho_{1,i}, \dots, \rho_{s,i})$ represents the effects of the previous responses $(Y_{i(t-1)}, \dots, Y_{i(t-s)})$ influencing the response Y_{it} at time point t , which is the stochastic component of the model. The linear model component, $\beta_{0,i} + \beta_{1,i}X_{1,it} + \cdots + \beta_{k,i}X_{k,it}$, corresponds to the deterministic component. This model is known as an autoregressive model of order s (AR(s)); given the previous responses, $(Y_{i(t-1)}, \dots, Y_{i(t-s)})$, the current response, Y_{it} , does not depend on the responses before time $(t - s)$. By determining the lag order s , the number of time points required for prediction can be identified. The parameters can then be estimated by MLE and tested by Wald test.

Consider causality as a cause-effect relationship among variables or events in linear time, multivariate AR model provides a statistical approach to investigate causality among the model variables. For simplicity, consider a bivariate AR(1) model as follow:

$$\begin{bmatrix} X_t \\ Y_t \end{bmatrix} = \begin{bmatrix} \rho_{XX} & \rho_{XY} \\ \rho_{YX} & \rho_{YY} \end{bmatrix} \begin{bmatrix} X_{t-1} \\ Y_{t-1} \end{bmatrix} + \begin{bmatrix} \varepsilon_{t,X} \\ \varepsilon_{t,Y} \end{bmatrix}$$

The coefficient ρ_{XY} (or ρ_{YX}) measures the usefulness of Y_{t-1} to predict X_t (or X_{t-1} to predict Y_t). If $\rho_{XY} = 0$ and $\rho_{YX} \neq 0$, X_t is said to cause Y_t but not the other way round (Figure 1.3). This kind of statistical causality is first introduced by Granger in 1969 (Granger, 1969) and widely applied in economic research.

Although, AR model can provide more realistic modeling than linear modeling, it is not commonly used in biomedical research since it requires data to be measured in regular time intervals which is practically difficult to obtain. Continuous-time autoregressive (CAR) model is an extension of AR model to handle data measured in irregular time intervals. However, due to its model complexity, it is not widely adopted in biomedical research. Therefore, both AR and CAR models are not as popular as linear modeling in applied science.

1.6.3.3 Random coefficient autoregressive model

Similar to the extension from linear model to linear mixed model, given a collection of longitudinal data from a group of individuals, AR model can be extended by introducing random autoregressive coefficients to account for the differences between individuals. This model is introduced by Rahiala (Rahiala, 1999) and is called a random coefficient autoregressive (RCA) model. The RCA model is formulated as below:

$$Y_{it} = \rho_1 Y_{i(t-1)} + \rho_2 Y_{i(t-2)} + \cdots + \rho_s Y_{i(t-s)} \\ + \tau_{1,i} Y_{i(t-1)} + \tau_{2,i} Y_{i(t-2)} + \cdots + \tau_{s,i} Y_{i(t-s)}$$

$$\begin{aligned}
& +\beta_0 + \beta_1 X_{1,it} + \cdots + \beta_k X_{k,it} \\
& +u_{0,i} + u_{1,i} X_{1,it} + u_{2,i} X_{2,it} + \cdots + u_{k,i} X_{k,it} + \varepsilon_{it}
\end{aligned}$$

where (ρ_1, \dots, ρ_s) and $(\tau_{1,i}, \dots, \tau_{s,i})$ represent the fixed and random effects of the previous responses $(Y_{i(t-1)}, \dots, Y_{i(t-s)})$, respectively, and $(\beta_0, \dots, \beta_k)$ and $(u_{0,i}, \dots, u_{k,i})$ represent the fixed and random effects of the covariates $(1, X_{1,it}, \dots, X_{k,it})$ at time t , respectively.

Assuming $(\tau_{1,i}, \dots, \tau_{s,i}, u_{0,i}, \dots, u_{k,i})^T \sim N(\tilde{0}, \Sigma)$ and $\varepsilon_{it} \sim N(0, \sigma^2)$ are independent, the parameters $(\rho_1, \dots, \rho_s, \beta_0, \dots, \beta_k)$, σ^2 and Σ can be estimated by MLE in a similar manner as in LMM by treating the autoregressive covariates, $(Y_{i(t-1)}, \dots, Y_{i(t-s)})$, like the exogenous covariates, $(1, X_{1,it}, \dots, X_{k,it})$, if measurements are obtained in a regular basis with only a few missing observations. Under some regularity conditions, the MLE of the fixed effect coefficients, $(\rho_1, \dots, \rho_s, \beta_0, \dots, \beta_k)$, follows an asymptotic normal distribution with a mean of $(\rho_1, \dots, \rho_s, \beta_0, \dots, \beta_k)$ and a variance equals to the Fisher information matrix. Significance of any fixed effect coefficient can be tested by Wald test and LRT, and the existence of any random coefficient can be tested by linear combination of LRT with different degrees of freedom as in LMM (Rahiala, 1999). Since LMM is more commonly known in biomedical research, and RCA model shares many similarities with LMM,

it is also called random coefficient autoregressive linear mixed model (RCALMM).

For data obtained in irregular time intervals, parameter estimation for a restricted RCALMM model without random autoregressive effect is provided by Funatogawa et al. (Funatogawa et al., 2007). Since this model can be decomposed as a fixed effect AR model and a mixed effect LMM, it is also known as an autoregressive linear mixed model (ARLMM). Currently, there are only a few biomedical studies built on RCALMM (Fried, 2001, Funatogawa et al., 2007, Funatogawa et al., 2008a, Funatogawa et al., 2008b, Funatogawa & Funatogawa, 2012). All of these models are based on the restricted ARLMM and none are unrestricted RCALMM.

1.6.4 Comparison of Trend and Event Analyses to detect structural progression

Fayers et al. (Fayers, Strouthidis, & Garway-Heath, 2007) compared the detection of rim area progression in glaucoma using both event and trend analyses. In the event analysis, progression is defined if the difference between the follow-up and baseline rim area measured by the HRT exceeded its reproducibility coefficient in one or more disc sectors with at least 2 of 3 consecutive tests. With a similar level of specificity at 94% - 95%, they found that event analysis had a higher sensitivity (28%) than trend analysis (12%) and the agreement between event and trend

analyses was poor. By contrast, trend-based change detection analysis based on statistical image mapping (SIM) developed by Patterson et al. (Patterson et al., 2005) was shown to have a better diagnostic precision in detecting change in HRT images than TCA in computer simulation and confirmed by longitudinal data with 20 normal and 30 ocular hypertensive subject. SIM had a higher proportion of change detection (73%) in ocular hypertensive subjects and a lower proportion of change detection (10%) in normal subjects than TCA (53% and 15%, respectively).

The agreement in progression detection between trend and event analyses on RNFL thickness measurements was poor. In the study by Moon et al. (Moon et al., 2012), progression were detected in 24.3% and 12.5% of 152 glaucomatous eyes with event and trend analyses, respectively, with only 3.3% were detected by both strategies. There is no consensus on which change detection strategy should be used to detect glaucoma progression.

1.6.5 Comparison of Trend and Event Analyses to detect Functional Progression

Casas-Llera et al. (Casas-Llera et al., 2009) and Antón et al. (Antón et al., 2013) compared the EMGT criteria and linear regression on VFI for detection of glaucoma progression. Both studies suggested that trend analysis has a lower sensitivity than event analysis with a comparable

specificity. The agreement between trend and event analysis is moderate (0.48 and 0.57, respectively). In the detection of localized visual sensitivity progression, sensitivity of point-wise trend analysis was also found to be less sensitive than event analysis (Vesti et al., 2003, Viswanathan et al., 2003, Kovalska et al., 2008).

1.6.6 Structural and Functional Progression Detection Strategies

The agreement between structural and functional progression has been known to be poor. In the study by Fayers et al. (Fayers et al., 2007), there were 28% and 22% eyes with progression detected by HRT event analysis and by the visual field AGIS criteria, respectively. 16% of eyes detected with progression by the HRT and 10% of eyes detected with progression by the AGIS criteria had no evidence of progression detected by the other technique. Poor agreement between structural and functional progression was also found in trend analysis. There were more than 87% of eyes with progression detected by trend analysis on rim area or VFI which cannot be confirmed by the other technique. In the study conducted by Moon et al. (Moon et al., 2012), 152 eyes of glaucomatous subjects were evaluated based on visual field EMGT criteria, trend analysis on VFI, and trend and event analysis on RNFL thickness measurements obtained with the SLP. Out of 71 eyes with progression detected by any of the four strategies, no more than 11.3% of eyes were detected in any pair of structural and functional detection strategies. Another study conducted by Alencar et al. (Alencar et al.,

2010) based on 453 eyes of 252 individuals with optic disc and RNFL assessment based on stereophotography and SLP and functional assessment based on SAP also observed poor agreement between structural and functional assessment (with Gwet's Agreement Coefficient=0.44) in progressing eyes.

1.7 Project Objectives

Assessment of the optic disc, RNFL and visual field and understanding the association between structural and functional progression are important to the monitoring of glaucoma. Although both event and trend analyses have been used for detection of change, there is no consensus regarding which approach should be used in clinical practice.

Disagreement was often found not only between structural and functional progression, but also between event and trend analyses in studies evaluating structure or function alone (Fayers et al., 2007, Casas-Llera et al., 2009, Alencar et al., 2010, Moon et al., 2012, Antón et al., 2013). We thereby set out to compare the performance of progression detection evaluated by trend and event analyses using the retinal nerve fiber layer measured by the spectral-domain OCT as the parameter of interest, and investigate the effect of detecting progressive RNFL thinning on subsequent change in function.

The research project is composed of three studies with the objectives of:

1. comparing the performance of event- and trend- based analyses to detect progressive reduction of average RNFL thickness in glaucoma;
2. investigating the performance of trend analysis to detect progressive RNFL thinning in the RNFL thickness map and;
3. determining the effect of RNFL measurement on subsequent change in visual function.

In the first study, a computer simulation study was performed to model RNFL progression with reference to the individual's test-retest variability and different patterns and rates of progression. The sensitivity, specificity and accuracy for the detection of progressive reduction of average RNFL thickness between event- and trend- based analyses were compared. The simulation findings were then validated using longitudinal data collected from a group of glaucoma and glaucoma suspect subjects.

In the second study, trend-based analysis of the RNFL thickness map was evaluated (Trend-based Progression Analysis or TPA) and the detection of RNFL progression was compared between TPA and Guided Progression Analysis (GPA), an event-based analysis of the RNFL thickness map provided by the Cirrus HD-OCT (Carl Zeiss Meditec). The specificities of the TPA and GPA were estimated from a group of normal subjects.

In the last study, a relatively new statistical model was used (autoregressive modeling) to investigate the causal relationship between RNFL progression and the visual field MD progression in a group of glaucoma patients and glaucoma suspects. The associations between prior average RNFL thickness or prior visual field MD on subsequent changes of RNFL thickness and visual field MD were investigated.

Figure 1.1 Classification tree of glaucoma

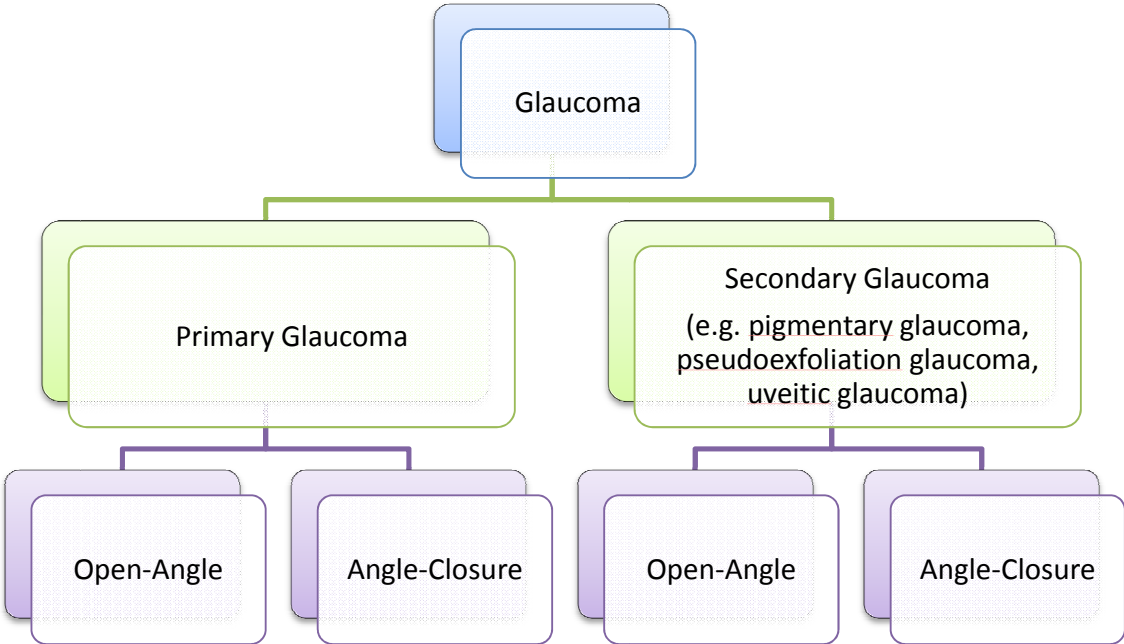
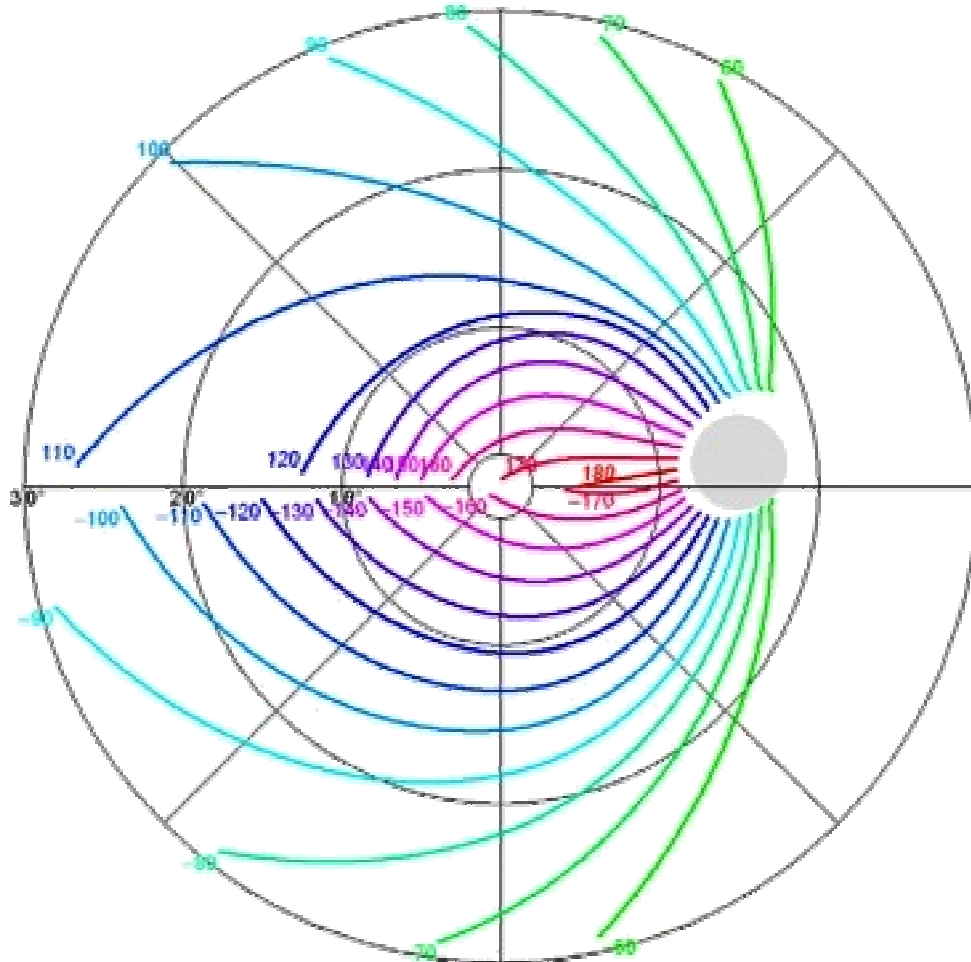
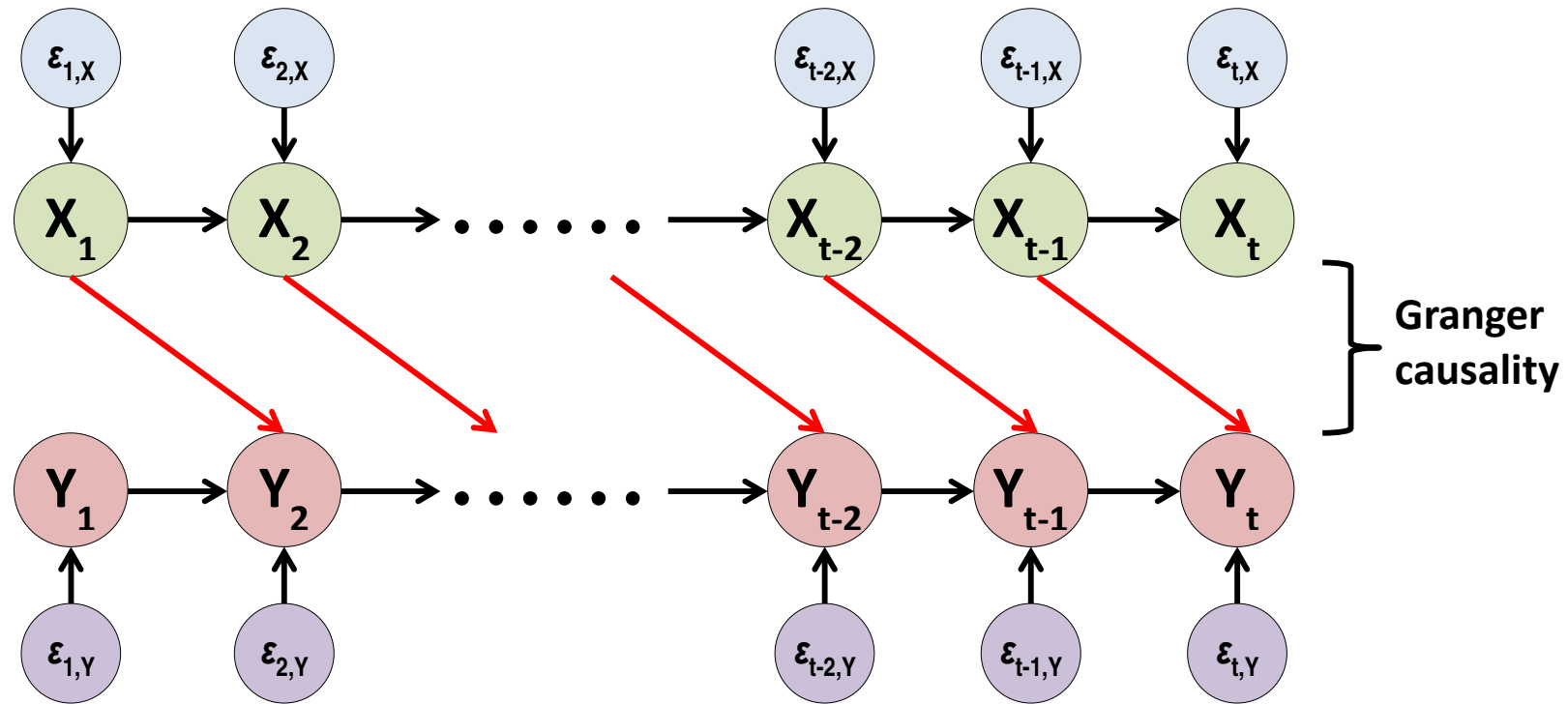


Figure 1.2 Retinal nerve fiber bundle trajectories



Reprinted from Jansonius et al., 2009

Figure 1.3 Visualization of a bivariate autoregressive model of order 1 with X_t causing Y_t .



CHAPTER 2 GENERAL MATERIALS AND METHODS

2.1 Subject Enrollments

Subjects were enrolled between June 2007 and March 2013 at the University Eye Center, the Chinese University of Hong Kong. The number of subjects enrolled in each study varied depending on the specific time period in which the subjects were recruited. All studies were conducted in accordance with the ethical standards stated in the Declaration of Helsinki and approved by a local research ethics committee, the Clinical Research Ethics Committee of Hong Kong Hospital Authority Kowloon West Cluster, with written consent obtained from all participants.

2.2 Inclusion and Exclusion Criteria

All subjects underwent a full ophthalmic examination, including visual acuity, refraction, intraocular pressure measurement with Goldman tonometry, gonioscopy and dilated fundus examination with stereoscopic biomicroscopy of optic nerve head under slit-lamp and indirect ophthalmoscopy. Eyes were included if the visual acuity was at least 20/40. Eyes with macular disease, refractive or retinal surgery, neurological disease or history of diabetes were excluded.

2.3 Humphrey Visual Field Perimetry

Visual field testing was performed using static automated white-on-white threshold perimetry (SAP) with 24-2 Swedish Interactive Threshold Algorithm (SITA) Standard (version 4.1) in the Humphrey Field Analyzer II (HFA II, Carl Zeiss Meditec). The SITA standard testing strategy uses the size III stimuli of 4 mm² with each stimulus presented for 200 ms. 54 locations within the central 24° visual field were tested. Stimulus intensities changed in a 4-2 dB staircase to detect the visual sensitivity at each test location, which initially changed in 4 dB steps until the stimulus can be seen or no longer be seen and then followed by changes in 2 dB steps until turnaround. Threshold values were continuously estimated based on the maximum a posteriori estimator during the 4-2 staircase procedure. Fixations were tested through the blind spot (Heijl-Krakau) test program by checking the visibility of the stimuli projected at the presumed blind spot location. A visual field examination was defined as reliable when fixation losses, false positive and false negative errors were all less than 20%. Average visual field sensitivity was expressed in MD (mean deviation) as calculated by the perimetry software. A visual field defect was defined as having three or more significant ($p < 0.05$) non-edge contiguous points with at least one at the $p < 0.01$ level on the same side of horizontal meridian in the pattern deviation plot and confirmed with at least two consecutive examinations.

2.4 Spectral-Domain OCT RNFL Imaging

Spectral-domain OCT imaging was performed by the Cirrus HD-OCT Model 400 (Carl Zeiss Meditec) (software version 5.0 to 6.0), which is a spectrometer-based OCT using an 840 nm superluminescent light emitting diode as a broadband light source for the generation of interference between the backscattered and backreflected waves resolved by the spectrometer. The acquisition rate of the Cirrus HD-OCT is 27,000 A-scans per second with 2.0 mm A-scan depth. The transverse and axial resolutions are 15 μm and 5 μm , respectively. The “Optic Disc Cube 200x200” exam protocol was used to measure the RNFL thickness in a 6x6 mm² area consisting of 200x200 A-scans (pixels) at the optic disc region. The RNFL thickness at each pixel was measured and the RNFL thickness map was generated. An OCT image was defined as reliable when the signal strength was greater than 7 without motion artifact. Dilation with tropicamide 0.5% and phenylephrine 0.5% each was performed when the pupil size was too small to obtain images with the required quality. Images with poor centration and motion artifact were rescanned in the same visit. Average RNFL thickness was expressed as the average RNFL thickness derived from the scan circle of 3.46 mm diameter centered at the optic disc center consisting of 256 A-scans, where the location of the optic disc center was identified by the built-in algorithm.

2.5 Definition of Glaucoma, Glaucoma Suspects and Normal

Subjects

Glaucoma subjects were identified based on the presence of visual field defects with corresponding optic disc and RNFL changes (narrowing of neuroretinal rim or thinning of the RNFL) in at least one eye. Glaucoma suspects and ocular hypertension subjects, which were simply called as 'glaucoma suspects' in the following studies, were defined as subjects without evidence of visual field defect on Humphrey visual field perimetry but had glaucomatous optic disc and/or RNFL changes and/or intraocular pressure greater than 22 mmHg for at least 3 visits. Normal subjects were defined as having both eyes with normal optic nerve head appearance (symmetric cup/disc ratio of less than 0.5 with uniform neuroretinal rim) in stereoscopic examination under slit lamp and without evidence of visual field defect on Humphrey visual field perimetry and no history of intraocular pressure greater than 22 mmHg.

2.6 Statistical Analysis

Statistical analyses were performed with the numerical computing software MATLAB R2010a (The MathWorks, Inc., Natick, MA) and the statistical computing software R version 2.15.2 (R Foundation, Vienna, Austria). MATLAB was used for computer simulation to evaluate the performance of event- and trend- based analyses, and for the TPA (Trend-based Progression Analysis) developed to evaluate the

progressive RNFL thinning in the RNFL thickness map. R was used for statistical modeling of the structure-function relationship in glaucoma progression. Statistical methods of the three studies are described in the respective session.

**CHAPTER 3 THE INVESTIGATION OF RETINAL NERVE
FIBER LAYER PROGRESSION DETECTION**

3.1 Computer Simulation of Progressive Retinal Nerve Fiber Layer Loss in Glaucoma: A Comparison between Event and Trend Analysis

3.1.1 Abstract

Objectives: Event- and trend- based analyses (EA and TA) have been widely adopted to evaluate glaucoma progression in clinical practice. However, the agreement between the strategies is often poor. With computer simulation of progressive loss of the retinal nerve fiber layer (RNFL), we compared the performance of EA and TA for detection of glaucoma progression.

Methods: RNFL progression was modeled with reference to the individual test-retest variability, the rate of progression, and different patterns of progression. The sensitivity, specificity and accuracy of each scenario were computed from 5000 simulated datasets. Simulation results were then validated with longitudinal RNFL measurements obtained from 107 glaucoma subjects and glaucoma suspects with a median follow-up of 38 months.

Results: In the computer simulation study, TA attained a sensitivity $\geq 80\%$ for detection of RNFL progression earlier than EA. The specificity of TA was 95% and ranged between 80% and 100% for EA. TA had an accuracy $\geq 80\%$ earlier than EA. On the other hand, EA using a group reproducibility coefficient had a higher sensitivity than TA in eyes with a

large test-retest variability in the early follow-up period, albeit at a lower specificity. In the longitudinal study, the detection rate was 42%, 35%, and 3% for TA, whereas it was 11% to 40%, 12% to 28%, and 3% to 23% for EA at 36 months of follow-up in eyes with small, average, and large test-retest variabilities, respectively.

Conclusions: TA generally outperformed EA for the detection of RNFL progression in glaucoma and the test-retest variability was an important determinant in progression analysis.

3.1.2 Background and Objectives

In glaucoma, event- and trend- based analyses have been widely adopted for detection of change in glaucoma progression. In event analysis (EA), progression is commonly defined when the difference of a parameter of interest between the baseline and the follow-up visits is greater than the test-retest variability. In trend analysis (TA), progression is commonly defined when a significant negative trend is detected with linear regression between the parameter of interest and time. In major clinical trials in glaucoma treatment, the key outcome measures have been largely based on event analysis of visual field measurements. In the Advanced Glaucoma Intervention Study (AGIS) and the Collaborative Initial Glaucoma Treatment Study (CIGTS), 20-step visual field scoring system (0 - normal, 20 - advanced visual field loss) was developed based on the extent and the depth of defects in total deviation plot in the visual field printouts (AGIS investigators, 1994a, AGIS investigators, 1994b, Musch et al., 1999). In AGIS, progression was defined when the score increased by 4 or more (95% of glaucomatous eyes showed a test-retest variability of 3) and confirmed with two consecutive examinations (AGIS Investigators, 1994a). In CIGTS, progression was defined when the score increased by 3 or more and confirmed with two consecutive examinations (Musch et al., 1999). In the Early Manifest Glaucoma Trial (EMGT), individual test locations were evaluated. A change in visual sensitivity at a test location was

defined when the change was outside the 95% test-retest variability, and progression was defined if 3 or more test locations showed significant deterioration with two consecutive examinations (Leske et al., 1999).

Comparatively, trend analysis was less popular in clinical trials for evaluation of glaucoma treatment. Although there are a number of statistical packages available to evaluate glaucoma progression based on linear regression of mean deviation (MD), visual field index (VFI) (Guided Progression Analysis, Carl Zeiss Meditec, Dublin, CA), and RNFL measurements (Guided Progression Analysis, Carl Zeiss Meditec), the agreement of progression detection between event and trend analysis for both structure and function is often poor. No consensus has been reached regarding which strategy to be used for progression evaluation.

In this study, computer simulation was used to model progressive loss of the RNFL and the performance of event and trend analyses was compared for detection of RNFL progression. Longitudinal RNFL measurements collected from a cohort of glaucoma patients were also analyzed to validate the finding obtained from the computer simulation study.

3.1.3 Subjects and Methods

3.1.3.1 Subjects

All subjects were consecutively enrolled from June 2007 to March 2011 at the University Eye Center, the Chinese University of Hong Kong. All subjects underwent visual field examination using SAP (SITA Standard 24-2, HFA II, Carl Zeiss Meditec), spectral-domain OCT RNFL imaging (Cirrus HD-OCT, Carl Zeiss Meditec) and full ophthalmic examination, including measurement of visual acuity, refraction, intraocular pressure and fundus examination. Subjects were classified into normal, glaucoma suspects or glaucoma groups according to the definition stated in section 2.5. Based on the inclusion and exclusion criteria stated in section 2.2, 46 eyes of 46 subjects (19 glaucoma and 27 normal subjects) were examined weekly for 8 consecutive weeks for measurement of intervisit test-retest variability. 175 eyes of 81 glaucoma subjects and 26 glaucoma suspects (121 eyes with open-angle glaucoma, 7 eyes with angle-closure glaucoma and 47 eyes with suspected glaucoma) were examined every 4 months for at least 30 months (range 30 - 42 months with median of 38 months) to validate the results of the computer simulation.

3.1.3.2 Simulation of RNFL progression

Computer simulation was performed using MATLAB R2010a (The MathWorks, Inc., Natick, MA) months) to model progressive reduction

and non-progressive condition of average RNFL thickness. Four different patterns (linear, episodic, exponential, and parabolic loss) (Figure 3.1.1) and two different rates ($-2 \mu\text{m}/\text{year}$ and $-4 \mu\text{m}/\text{year}$) of RNFL progression plus a stable non-progressive condition were modeled with three different values of test-retest variability (small, average and large test-retest variabilities). Linear progression referred to a constant rate of change of average RNFL thickness over time. Episodic progression referred to a stepwise loss of average RNFL thickness with a phase of linear progression followed by a phase of no change. Exponential progression had had exponential loss of the average RNFL thickness. Parabolic progression referred to a rate of change which was linearly proportional to the square of time. The modeled rates of RNFL progression were selected with reference to the study by Leung et al. (2011), which showed that the rate of average RNFL thickness progression ranged between $-1.52 \mu\text{m}/\text{year}$ and $-5.03 \mu\text{m}/\text{year}$. Therefore, the modeled rates $-2 \mu\text{m}/\text{year}$ and $-4 \mu\text{m}/\text{year}$ would capture the average rate of slow and fast progressors, respectively. The test-retest variabilities of average RNFL thickness were estimated based on the reproducibility coefficients calculated from the 46 eyes of 46 subjects (19 glaucoma and 27 normal subjects) who had weekly RNFL measurements for 8 consecutive weeks. The within-subject standard deviation (SD) of average RNFL thickness had a mean of $1.77 \mu\text{m}$ and a median of $1.71 \mu\text{m}$, with 95% confidence interval between 1.59 and 1.93

μm , and a range between 0.74 μm and 3.50 μm (Table 3.1.1). The minimum (0.74 μm), median (1.71 μm) and maximum (3.50 μm) within-subject SD were selected to represent eyes with small, average and large RNFL measurement variability in the simulation, respectively

For each simulation scenario, 5,000 datasets were simulated. Each dataset were simulated with 16 average RNFL thickness measurements randomly generated from independent normal distribution with a specified within-subject SD, representing RNFL measurements collected every 4 months over 60 months (Figure 3.1.2). Each dataset was analyzed by five different event- and trend- based strategies described in section 3.1.3.3. The proportions of progression detection from the 5,000 simulated datasets were used to estimate the sensitivities and specificities for the five strategies. A sample size of 5,000 was chosen to satisfy all the SDs of the specificity estimates were <1%.

3.1.3.3 Definitions of progression detection

1. Event analysis with individual reproducibility coefficient

Progression was defined when the difference in average RNFL thickness between the first and the most recent measurements was greater than the individual's reproducibility coefficient (reproducibility coefficient was defined as $2 \times \sqrt{2} \times$ within-subject standard deviation (Bland & Altman, 1996)).

2. Event analysis with group reproducibility coefficient

Progression was defined when the difference in average RNFL thickness between the first and the most recent measurement was greater than the reproducibility coefficient derived from a group of reference individuals ($2 \times \sqrt{2} \times$ mean within-subject standard deviation (1.77 μm)).

3. Event analysis with individual reproducibility coefficient confirmed with a consecutive test

Progression was defined when the differences in average RNFL thickness between the baseline and the most recent two measurements were both greater than the individual's reproducibility coefficient.

4. Event analysis with group reproducibility coefficient confirmed with a consecutive test

Progression was defined when the differences in average RNFL thickness between the baseline and the most recent two visits were both greater than the group's reproducibility coefficient.

5. Trend analysis

Progression was defined when a significant negative trend ($p < 0.05$) was detected between average RNFL thickness and time.

3.1.3.4 Estimation of sensitivity, specificity, and accuracy

Sensitivity, specificity and accuracy were computed and compared among the five progression detection strategies. An ideal strategy would have high sensitivity, specificity and accuracy. Sensitivity was estimated by the proportion of datasets detected with progression (out of 5,000 simulated datasets) with an imposed progression pattern. Specificity was estimated by the proportion of datasets detected with no progression without an imposed progression pattern. Accuracy is the multiplication of sensitivity and specificity. They were computed at 12 months and then every 4 months until 60 months of the simulation.

3.1.4 Statistics

Mathematical Formulas for Sensitivity and specificity

The sensitivity and specificity of each of the progression detection strategies can be derived in mathematical formulas. A list of symbol annotations is summarized as follow:

- Y_i An independent average RNFL thickness measurement obtained at a particular visit and distributes normally with homogenous variance (i.e. $Y_i \sim N(\mu_i, \sigma^2)$).
- μ_i The average RNFL thickness in the i th visit.
- σ The standard deviation of an individual patient.
- σ_g The standard deviation of a group of patients.

- z_α The critical value satisfying $\Phi(-z_\alpha) = \alpha$ (The corresponding z_α for $\alpha=0.05$ is 1.645).
- $\Phi(\cdot)$ The cumulative distribution function of standard normal distribution.
- $\Phi_{2;\Sigma}(\cdot)$ The cumulative distribution function of a bivariate normal with mean $\begin{bmatrix} 0 \\ 0 \end{bmatrix}$ and variance-covariance matrix Σ .

Event analysis with individual reproducibility coefficient

Under the normal distribution assumption,

$D_n = (Y_n - Y_1) \sim N(\mu_n - \mu_1, 2\sigma^2)$, progression was defined when $D_n < -z_\alpha \sqrt{2\sigma^2}$.

Denoting z_α to be the critical value satisfying $\Phi(-z_\alpha) = \alpha$ and $\Phi(\cdot)$ to be the cumulative distribution function of standard normal distribution, the specificity is

$$1 - \Phi(-z_\alpha) = (1 - \alpha),$$

and the sensitivity is

$$P(D_n < -z_\alpha \sqrt{2\sigma^2} \mid \mu_n < \mu_1) = \Phi\left(-z_\alpha - \frac{\mu_n - \mu_1}{\sqrt{2\sigma^2}}\right).$$

Event analysis with group reproducibility coefficient

Progression was defined when $D_n < -z_\alpha \sqrt{2\sigma_g^2}$.

Since $-z_\alpha \sqrt{2\sigma_g^2} = -z_\alpha \frac{\sigma_g}{\sigma} \sqrt{2\sigma^2}$, the specificity is

$$1 - \Phi\left(-z_\alpha \frac{\sigma_g}{\sigma}\right) = \Phi\left(z_\alpha \frac{\sigma_g}{\sigma}\right),$$

and the sensitivity is

$$\Phi\left(-z_\alpha \frac{\sigma_g}{\sigma} - \frac{\mu_n - \mu_1}{\sqrt{2}\sigma^2}\right).$$

Event analysis with individual reproducibility coefficient confirmed with a consecutive test

Under the independent normal distribution assumption of Y_i ,

$$\begin{bmatrix} D_{n-1} \\ D_n \end{bmatrix} \sim N\left(\begin{bmatrix} \mu_{n-1} - \mu_1 \\ \mu_n - \mu_1 \end{bmatrix}, 2\Sigma\sigma^2\right),$$

where

$$\Sigma = \begin{bmatrix} 1 & 0.5 \\ 0.5 & 1 \end{bmatrix}$$

with the correlation between the two differences come from the common term, Y_1 .

Denoting the cumulative distribution function of a bivariate normal with mean $\begin{bmatrix} 0 \\ 0 \end{bmatrix}$ and variance-covariance matrix Σ to be $\Phi_{2;\Sigma}(\cdot)$. To control the specificity at $(1 - \alpha)$, progression was defined if $D_{n-1} < -z_\alpha\sqrt{2}\sigma^2$ and $D_n < -z_\alpha\sqrt{2}\sigma^2$.

The specificity is

$$1 - \Phi_{2;\Sigma}(-z_\alpha, -z_\alpha),$$

and the sensitivity is

$$\begin{aligned} & P\left(D_{n-1} < -z_{\alpha}\sqrt{2\sigma^2}, D_n < -z_{\alpha}\sqrt{2\sigma^2} \mid \mu_n < \mu_1\right) \\ &= \Phi_{2;\Sigma}\left(-z_{\alpha} - \frac{\mu_n - \mu_1}{\sqrt{2\sigma^2}}, -z_{\alpha} - \frac{\mu_{n-1} - \mu_1}{\sqrt{2\sigma^2}}\right) \end{aligned}$$

Event analysis with group reproducibility coefficient confirmed with a consecutive test

Similarly, by replacing the individual standard deviation σ with the group standard deviation σ_g the classification cutoff becomes

$$-z_{\alpha}\sqrt{2\sigma_g^2} = -z_{\alpha}\frac{\sigma_g}{\sigma}\sqrt{2\sigma^2}.$$

Therefore, the specificity and sensitivity are

$$1 - \Phi_{2;\Sigma}\left(z_{\alpha}\frac{\sigma_g}{\sigma}, z_{\alpha}\frac{\sigma_g}{\sigma}\right),$$

and

$$\Phi_{2;\Sigma}\left(-z_{\alpha}\frac{\sigma_g}{\sigma} - \frac{\mu_n - \mu_1}{\sqrt{2\sigma^2}}, -z_{\alpha}\frac{\sigma_g}{\sigma} - \frac{\mu_{n-1} - \mu_1}{\sqrt{2\sigma^2}}\right),$$

respectively.

Trend analysis

Simulated serial RNFL measurements were analyzed by ordinary least square regression. Progression was defined if the slope β was <0 .

The estimate of β is given by

$$\hat{\beta} = \frac{\widehat{\text{Cov}}(X,Y)}{\widehat{\text{Var}}(X)} = \frac{\sum x_i y_i - (\sum x_i)(\sum y_i)/n}{\sum x_i^2 - (\sum x_i)^2/n}.$$

In the model, each RNFL measurement was simulated at regular intervals. The summation of x can be expressed by an arithmetic series $1 + 2 + 3 + \dots + n$ where n represents the n th measurement.

$$x_i = i, \sum x_i = \frac{n(n+1)}{2}, \sum x_i^2 = \frac{n(n+1)(2n+1)}{6}$$

and

$$\hat{\beta} = \sum \left(i - \frac{n+1}{2} \right) y_i / \left(\frac{n(n+1)(2n+1)}{6} - \frac{n(n+1)^2}{4} \right) = \frac{\sum (2i - (n+1)) y_i}{n(n^2 - 1)/6}.$$

Under the normal distribution assumption,

$$\hat{\beta} \sim N \left(\frac{\sum (2i - (n+1)) \mu_i}{n(n^2 - 1)/6}, \frac{2\sigma^2}{n(n^2 - 1)/6} \right).$$

To control the specificity at $(1 - \alpha)$, progression was defined when

$$\hat{\beta} < -z_\alpha \sqrt{\frac{2\sigma^2}{n(n^2 - 1)/6}}$$

and the sensitivity is given by

$$P \left(\hat{\beta} < -z_\alpha \sqrt{\frac{2\sigma^2}{n(n^2 - 1)/6}} \mid \mu_n < \mu_1 \right) = \Phi \left(-z_\alpha - \frac{\sum (2i - (n+1)) \mu_i}{\sqrt{(n(n^2 - 1)/3)\sigma^2}} \right).$$

The duration (years), δ , required to detect progression at a sensitivity ρ with θ observations per year with a yearly reduction of average RNFL thickness at γ is given by:

$$\delta(\theta, \gamma, \rho) = \arg \min_d \left\{ d \left| \Phi \left(-z_\alpha - \frac{\gamma \sum_{i=0,1,\dots, \lfloor \theta d \rfloor} (2i - (\lfloor \theta d \rfloor + 1)) \frac{i}{\theta}}{\sqrt{\left(\frac{\lfloor \theta d \rfloor (\lfloor \theta d \rfloor^2 - 1)}{3} \right) \sigma^2}} \right) \right| \geq \rho \right\}$$

3.1.5 Results

3.1.5.1 Sensitivity of progression detection

Figure 3.1.3 illustrates the sensitivities for detection of average RNFL thickness progression modeled at a rate of $-2 \mu\text{m}/\text{year}$ based on the 5 progression detection strategies (1. EA with individual RC, 2. EA with group RC, 3. EA with individual RC confirmed with a consecutive test, 4. EA with group RC confirmed with a consecutive test, 5. TA) over 60 months under the 4 different progression patterns (1. linear, 2. episodic, 3. exponential, 4. parabolic) for eyes with small ($\text{SD}=0.74 \mu\text{m}$), average ($\text{SD}=1.71 \mu\text{m}$) and large ($\text{SD}=3.50 \mu\text{m}$) test-retest variabilities.

The computer simulation suggested that sensitivity of progression detection depended on the duration of follow-up, pattern of progression, rate of RNFL loss, individual test-retest variability and the analysis strategy. With increasing duration of follow-up, RNFL loss increased, and the sensitivity of progression detection increased independent of other factors. With the dramatic reduction of RNFL thickness in the beginning of the exponential loss, it attained a sensitivity $\geq 80\%$ for progression detection earlier than other progression patterns. By contrast, parabolic RNFL loss required the longest duration to reach the

same sensitivity among the four progression patterns. Linear and episodic progressions had sensitivity profiles in between those of exponential and parabolic progressions. Under the same progression pattern with same progression rate, analyzed by the same strategy, eyes with smaller test-retest variability took shorter time to achieve sensitivity $\geq 80\%$.

For eyes with an average test-retest variability, the sensitivities of EA with individual RC and EA with group RC were almost identical (Figure 3.1.3 E-H). However, eyes with a small test-retest variability had higher sensitivity under EA with individual RC (Figure 3.1.3 A-D), and eyes with a large test-retest variability had higher sensitivity under EA with group RC (Figure 3.1.3 I-L). The same property was founded in EA confirmed with a consecutive test, with sensitivity $\geq 80\%$ always attained later than those without confirmation, independent of the progression pattern and individual test-retest variability.

In all scenarios, TA always attained sensitivity $\geq 80\%$ earlier than the other four EA progression detection strategies, where the differences in sensitivity were minimal compared with EA with individual RC for eyes with a small test-retest variability in the episodic and exponential progression patterns (Figure 3.1.3 B and C). Based on the mathematical formulas shown in section 3.1.4, the minimum duration required to attain a pre-specified sensitivity of RNFL progression detection can be calculated. Figure 3.1.4 shows the minimum duration required to attain a

sensitivity of RNFL progression detection at 80% at various linear reduction rates. For example, for a linear rate of $-1.5 \mu\text{m}/\text{year}$ in eyes with large test-retest variability, TA required 60 months to attain a sensitivity of 80%, but EA with individual RC and with group RC required 100 and 68 months, respectively (Figure 3.1.4 C). In contrast, TA, EA with individual RC and EA with group RC required 20, 24 and 40 months to attain a sensitivity of 80% in eyes with small test-retest variability for the same RNFL reduction rate, respectively (Figure 3.1.4 A). Similar to the finding observed in the computer simulation (Figure 3.1.3), TA generally attained sensitivity of 80% earlier than EA with individual RC and EA with group RC, except for eyes with large test-retest variability, the RNFL reduction rate $<-2.5 \mu\text{m}/\text{year}$ and progression detected by EA with group RC (Figure 3.1.4 C).

Figure 3.1.5 illustrates the sensitivities for detection of average RNFL thickness progression based on the simulation modeled at reduction rate of $-4 \mu\text{m}/\text{year}$. The pattern of sensitivity profiles for each progression detection strategy was similar to those with a rate of $-2 \mu\text{m}/\text{year}$ (Figure 3.1.3), with shorter duration required to attain a sensitivity of 80%.

Some of these findings can be directly observed from the mathematical formulas of the sensitivity of the five strategies:

EA with individual RC:
$$\Phi\left(-z_{\alpha} - \frac{\mu_n - \mu_1}{\sqrt{2\sigma^2}}\right)$$

EA with group RC: $\Phi\left(-z_{\alpha} \frac{\sigma_g}{\sigma} - \frac{\mu_n - \mu_1}{\sqrt{2\sigma^2}}\right)$

EA with individual RC confirmed with a consecutive test:

$$\Phi_{2;\Sigma}\left(-z_{\alpha} - \frac{\mu_n - \mu_1}{\sqrt{2\sigma^2}}, -z_{\alpha} - \frac{\mu_{n-1} - \mu_1}{\sqrt{2\sigma^2}}\right)$$

EA with group RC confirmed with a consecutive test:

$$\Phi_{2;\Sigma}\left(-z_{\alpha} \frac{\sigma_g}{\sigma} - \frac{\mu_n - \mu_1}{\sqrt{2\sigma^2}}, -z_{\alpha} \frac{\sigma_g}{\sigma} - \frac{\mu_{n-1} - \mu_1}{\sqrt{2\sigma^2}}\right)$$

TA: $\Phi\left(-z_{\alpha} - \frac{\sum(2i-(n+1))\mu_i}{\sqrt{(n(n^2-1)/3)\sigma^2}}\right)$.

For example with increasing RNFL loss, $(\mu_n - \mu_1) \ll 0$, the sensitivity of progression detection increased. And with larger individual test-retest variability, $\sigma \uparrow$, the sensitivity of progression detection decreased. Sensitivity of different patterns of progression, rates of progression or test-retest variabilities can also be obtained through the mathematical formulas.

3.1.5.2 Specificity of progression detection

In the mathematical expressions in section 3.1.4, TA and EA with individual RC had the same level of specificity independent of the test-retest variability, which was also observed in the simulation results displayed in Figure 3.1.6. Confirming progression detection with a consecutive test, the specificity of EA with individual RC increased to 99%. The specificity of EA with group RC varied from 80%, 95% to

almost 100% corresponding to eyes with small, average and large test-retest variability, respectively. With confirmation with a consecutive test, the specificity of EA with group RC increased to 91%, 99% and almost 100%, respectively.

3.1.5.3 Accuracy of progression detection

The accuracy is defined as (sensitivity \times specificity). Figure 3.1.7 and Figure 3.1.8 illustrated the simulated accuracy profiles of progression detection of average RNFL thickness at a rate of $-2 \mu\text{m}/\text{year}$ and $-4 \mu\text{m}/\text{year}$ for different scenarios, respectively. Independent of the patterns of progression, the rates of progression and the test-retest variability, TA generally attained accuracy of 80% earlier than the other four EA strategies. The accuracy of TA was bounded above by 95%. On the other hand, EA with group RC and EA with individual RC confirmed with a consecutive test had an accuracy close to 100% for eyes with a small test-retest variability.

3.1.5.4 Validation with prospective longitudinal data

Since the progression pattern, the rate of progression and the test-retest variability usually varies across different individuals, the true sensitivity of TA and EA is difficult to determine. However, it is still feasible to compare the relative performance of the five progression detection strategies by the proportion of eyes detected with progression over time. A total of 1680 longitudinal RNFL measurements obtained by a spectral-

domain OCT were collected longitudinally from 175 eyes of 81 glaucoma and 26 glaucoma suspect subjects followed every 4 months for at least 30 months (range between 30 - 43 months; median of 38 months). Each eye had an average of 10 serial measurements (range between 6 - 11 measurements). Table 3.1.2 shows the demographics, RNFL and visual field measurements of the 175 eyes.

The test-retest variability of each eye was estimated from the residuals of the linear regression fitted on all the available data of the particular eye. 123 eyes (70.3%) were found to have a test-retest variability of $1.77 \mu\text{m}$ at 10% level of significance. The proportion of eyes with progression detection by TA and EA computed from month 12 to month 36 were shown in Figure 3.1.9 A. Similarly, the performance of TA and EA were observed in the initial 30 months. At month 36, 35% of eyes were detected with progression by TA. However, only 12% - 28% of eyes were detected with progression by EA.

Performance of progression detection in eyes with small and large test-retest variability were evaluated by the first 50 eyes with smallest and the last 50 eyes with largest test-retest variability estimated through the residuals of linear regressions, respectively (the cut-off of 50 eyes was arbitrarily defined). EA with individual RC detected more progressing eyes than EA with group RC for eyes with small test-retest variability (Figure 3.1.9 B) and vice versa for eyes with a large test-retest variability (Figure 3.1.9 C). At month 36, TA detected more progressive eyes (42%)

than other strategies (11% - 40%) for eyes with small test-retest variability (Figure 3.1.9 B). For eyes with large test-retest variability, EA with group RC detected more progressive eyes (23%) than other strategies (3% - 17%) at month 36 (Figure 3.1.9 C). With progression confirmed with a consecutive test, fewer progressive eyes were detected (Figure 3.1.9). These findings closely resemble to the simulation results described in section 3.1.5.1.

3.1.6 Discussion

3.1.6.1 TA versus EA

According to the computer simulation results, TA attained a high sensitivity ($\geq 80\%$) earlier than EA in detection of RNFL progression at a comparable level of specificity (TA: 95% versus EA: 80% - 100%). The validation of the simulation results with the longitudinal RNFL measurements obtained from 175 eyes of 107 glaucoma and glaucoma suspect subjects confirmed that TA would be a preferable strategy for following and detecting disease progression in glaucoma.

3.1.6.2 EA with group RC versus EA with individual RC

EA using a group test-retest variability to detect change has been the prevailing approach to analyze glaucoma progression in clinical trials and clinical practice. However, it may fail to detect change for eyes with a small test-retest variability and falsely detect progression for eyes with a large test-retest variability. EA with individual reproducibility coefficient

(RC) provides an eye-specific approach of progression detection. With reference to the computer simulation results, EA with individual RC indeed had a higher sensitivity than EA with group RC for progression detection in eyes with a small test-retest variability. However, it had a lower sensitivity than EA with group RC in eyes with large test-retest variability. The specificity of EA with group RC (80%) was lower than EA with individual RC (95%). For eyes with an average test-retest variability, both EA with individual RC and EA with group RC have comparable sensitivity and specificity profiles. The mathematical calculated sensitivity and specificity are in line with these results and the longitudinal data also confirmed these findings (Figure 3.1.9). Recalling that the sensitivity of EA with individual RC and with group RC are

$$\Phi\left(-z_{\alpha} - \frac{\mu_n - \mu_1}{\sqrt{2\sigma^2}}\right)$$

and

$$\Phi\left(-z_{\alpha} \frac{\sigma_g}{\sigma} - \frac{\mu_n - \mu_1}{\sqrt{2\sigma^2}}\right)$$

respectively. If the individual test-retest variability is smaller than the group test-retest variability, i.e. the ratio $\frac{\sigma_g}{\sigma} > 1$, the classification cut-off of EA with group RC would become more negative and thus resulting in a lower sensitivity (and a higher specificity). On the other hand, if individual test-retest variability is larger than the group test-retest variability, i.e. the ratio $\frac{\sigma_g}{\sigma} < 1$, and the classification cut-off of EA with

group RC would become less negative and thus resulting in a higher sensitivity (but a lower specificity) compared with EA with individual RC (Figure 3.1.10). Generally, EA with individual RC is more sensitive than EA with group RC only in eyes with a small test-retest variability. Having a confirmation with a consecutive test would increase the specificity but reduce the sensitivity for progression detection as expected.

3.1.6.3 Factors affecting the selection between TA and EA

The computer simulation also suggests that EA with group RC may be more sensitive than TA in the early follow-up period for eyes with a large test-retest variability, which is more remarkable when the rate of progression is fast (Figure 3.1.5 I-L). By comparing the calculation of sensitivity between TA and EA with group RC,

$$\Phi\left(-z_{\alpha} - \frac{\sum(2i - (n + 1))\mu_i}{\sqrt{(n(n^2 - 1)/3)\sigma^2}}\right)$$

versus

$$\Phi\left(-z_{\alpha} \frac{\sigma_g}{\sigma} - \frac{\mu_n - \mu_1}{\sqrt{2}\sigma^2}\right)$$

, respectively, TA would be more sensitive than EA when

$$\frac{\sum(2i - (n + 1))\mu_i}{\sqrt{(n(n^2 - 1)/3)}} < z_{\alpha}(\sigma_g - \sigma) + \frac{\mu_n - \mu_1}{\sqrt{2}}$$

The performance of progression detection between the two strategies depends on the relative difference between the group and individual test-retest variability, $(\sigma_g - \sigma)$, and the number of follow-up visits, n . Therefore, TA would be more sensitive than EA with group RC in eyes with small test-retest variability followed for a long duration (i.e. more follow-up visits). This mathematical condition is true for any measurement not just restricted to the average RNFL thickness measurement. Therefore, it is true also for visual field measurements and any localized measurement. In contrast, even though EA with group RC can have a higher sensitivity than TA in the early follow-up period in eyes with large test-retest variability (Figure 3.1.3 I-L), its specificity is relatively low (80%) (Figure 3.1.6 C). As an ideal progression detection strategy should have a high sensitivity as well as specificity, accuracy provides a more comprehensive comparison between the five strategies by combining sensitivity and specificity together into a single index. According to the simulation results, TA always attained an accuracy of 80% earlier than the other four strategies, independent of the test-retest variability, the pattern of progression and the rate of progression (Figure 3.1.7).

3.1.6.4 Specificity

Since the level of significance, α , was chosen as 5%, it is not surprising to observe the specificity of TA and EA with individual RC was 95% in the computer simulation. In EA with group RC, the level of significance,

α , was chosen as 5% with respect to the group RC, the specificity would be 95% in eyes with average test-retest variability. Higher (lower) specificity (99% (80%)) can be obtained in eyes with a smaller (larger) test-retest variability. (Figure 3.1.6)

3.1.6.5 Duration and number of observations required to detect progression with desired sensitivity in TA

TA is preferable than EA in progression detection not only because it can attain a high accuracy earlier than EA, it can also provide an estimation of the rate of progression which is useful to guide treatment and evaluate disease prognosis. A reliable estimation of the rate of progression requires multiple measurements. Therefore, it is important to know how many observations are needed to provide a reliable estimate of the rate of progression. By specifying the level of sensitivity, the pattern and rate of progression, it is possible to work out the number of observations per year and the minimum follow-up duration required to detect progression. Figure 3.1.11 shows the relationship between the number of observations required per year and the minimum duration needed to detect a linear average RNFL thickness progression at rate of $-2 \mu\text{m}/\text{year}$ at a sensitivity of 70% and 80% for eyes with small ($\text{SD}=0.74 \mu\text{m}$), average ($\text{SD}=1.71 \mu\text{m}$), and large ($\text{SD}=3.50 \mu\text{m}$) test-retest variabilities. If three observations are obtained per year for a subject with an average test-retest variability ($\text{SD}=1.71 \mu\text{m}$), it takes 2.7 and 2.9 years to detect a progression with a rate of $-2 \mu\text{m}/\text{year}$ at 70% and 80%

level of sensitivity, respectively. Progression can be detected earlier by increasing the number of observations per year. Eyes with a large test-retest variability require a longer duration to detect the same rate of progression, particularly when the number of observations per year is small. In general, the number of measurements required depends on the rate of progression, the desired level of sensitivity, the individual test-retest variability and the acceptable duration for detection. The suggested optimal number of observations per year is approximately four, which can detect linear average RNFL thickness progression at a rate of $-2 \mu\text{m}/\text{year}$ in 1.5 to 3.8 years with sensitivity of 70% (or in 1.6 to 4.2 years with sensitivity of 80%) for subjects with test-retest variability between $0.74 \mu\text{m}$ and $3.50 \mu\text{m}$. The benefit of shortening the duration of progression detection is small by including additional observations, where the duration of progression detection can be shortened no more than 0.5 years per observation added. Glaucoma monitoring schedule should take the severity of disease and the life expectancy of the individual into consideration.

3.1.6.6 Glaucoma monitoring schedule for TA

The above discussion is based on glaucoma monitoring scheduled at regular time intervals. It is important to understand whether regular scheduling offers any advantage. In linear regression, the null hypothesis,

$$H_0: \beta = 0$$

is rejected if

$$\frac{\hat{\beta}}{\sqrt{\widehat{Var}(\hat{\beta})}} < -t_{\alpha, n-2}$$

where

$$\hat{\beta} = \frac{\sum(x_i - \bar{x})(y_i - \bar{y})}{\sum(x_i - \bar{x})^2}$$

is the ordinary least square (OLS) estimate of β and

$$\widehat{Var}(\hat{\beta}) = \frac{1}{n-2} \times \frac{\sum(\varepsilon_i - \bar{\varepsilon})^2}{\sum(x_i - \bar{x})^2}$$

is the estimated variance of $\hat{\beta}$.

Since $\hat{\beta}$ is an unbiased estimator of β (i.e. $E(\hat{\beta}) = \beta$), varying x_i (the observation time point) would have no effect on the estimation of β . On the other hand, the estimated variance of $\hat{\beta}$, $\widehat{Var}(\hat{\beta})$, can be minimized by maximizing the denominator term, $\sum(x_i - \bar{x})^2$. Therefore, by evenly dividing the number of observations to the beginning and the end of follow-up would provide the highest sensitivity of progression detection. This wait-and-see approach agrees with the computer simulation results conducted by Crabb & Garway-Heath (Crabb & Garway-Heath, 2012). One critical assumption of the OLS is that measurements obtained at each time point should have same variance and time independent.

However, this may not be legitimate in clinical situation when the follow-up duration is long. Development of cataract, surgical interventions, and instrument instability could substantially affect the quality of data collection and the reliability of measurement. The wait-and-see approach may result in a critical bias in estimating the rate of progression compared with scheduling the observations at regular time intervals. Also, any rapid progression experienced in between the follow-up period would be missed. Further investigation is needed to identify the time-dependency factors on progression analysis.

3.1.6.7 Generalization

Although the computer simulation is based on RNFL progression measured by spectral-domain OCT, the current findings can also be applied to other imaging or visual field examinations. Customized analysis strategy may be needed to monitor disease progression in different types of structural and functional tests. This study is limited in evaluating the performance of trend and event analysis on global change in RNFL thickness derived from the scan circle of 3.46 mm diameter centered at the optic disc center. We addressed the application of TA in the RNFL thickness map in the next session.

3.1.6.8 Conclusion

In conclusion, the sensitivity of progression detection in glaucoma depends on the pattern and rate of progression, the test-retest variability,

and the progression detection strategy. An appropriate selection of progression detection strategy and disease monitoring schedule can maximize the probability of progression detection. In general, TA can attain high sensitivity and accuracy earlier than EA at a comparable level of specificity. EA with group RC would have higher sensitive than TA in eyes with large test-retest variability at a cost of a lower specificity.

Table 3.1.1 Demographics, retinal nerve fiber layer (RNFL), and visual field measurements of 46 eyes of 46 subjects who underwent weekly RNFL evaluations for 8 consecutive weeks.

	Glaucoma Group	Normal Group	All
Sample size	19	27	46
Spherical error (D)	-2.7 ± 3.7	-1.3 ± 2.4	-1.9 ± 3.0
Age (year)	48.0 ± 13.8	42.9 ± 13.4	45.0 ± 13.6
Signal strength	8.3 ± 1.0	8.5 ± 0.8	8.4 ± 0.9
Average RNFL thickness (µm)	68.04 ± 13.59	99.88 ± 9.76	86.73 ± 19.50
VFI (%)	81.47 ± 24.19	99.48 ± 0.85	92.04 ± 17.75
MD (dB)	-7.55 ± 8.08	-0.87 ± 0.84	-3.63 ± 6.13
Test-retest variability (µm)			
Median	1.39	1.91	1.71
Minimum	0.83	0.74	0.74
Maximum	2.43	3.50	3.50
Mean	1.80	1.87	1.77

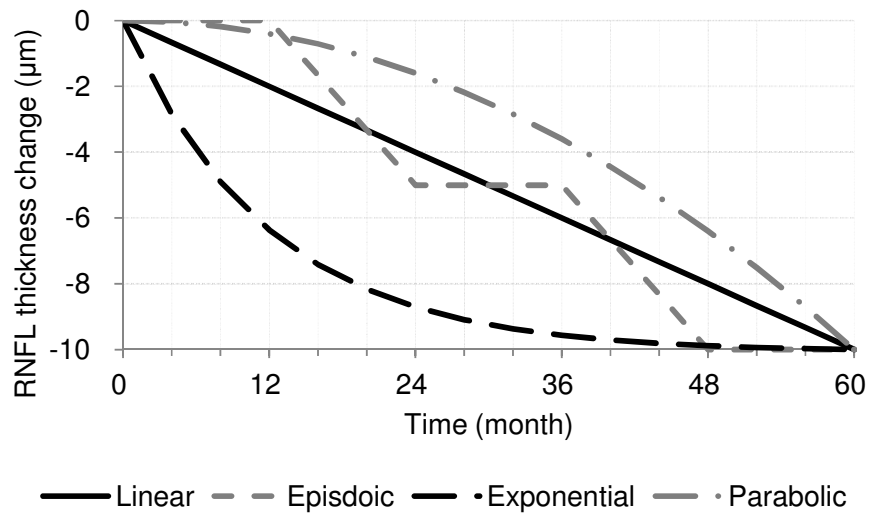
D = diopter; RNFL = retinal nerve fiber layer ; VFI = visual field index; MD = mean deviation

Table 3.1.2 Demographics, retinal nerve fiber layer (RNFL), and visual field measurements of 175 eyes of 107 glaucoma and glaucoma suspect subjects who were followed up every 4 months for at least 30 months.

	Mean ± SD
Spherical error (D)	-2.81 ± 4.15
Age (year)	51.3 ± 15.1
Signal strength	8.4 ± 1.1
<u>Baseline examination</u>	
Average RNFL thickness (µm)	74.07 ± 14.49
VFI (%)	79.54 ± 24.19
Visual field MD (dB)	-7.85 ± 8.22
<u>Final examination</u>	
Average RNFL thickness (µm)	71.99 ± 14.43
VFI (%)	73.01 ± 25.64
Visual field MD (dB)	-10.63 ± 8.27
<u>Duration of follow-up (month)</u>	
Median	38
Minimum	30
Maximum	43

D = diopter; RNFL = retinal nerve fiber layer; VFI = visual field index; MD = mean deviation.

Figure 3.1.1 Progressive average retinal nerve fiber layer (RNFL) thickness reduction modeled in linear, episodic, exponential, and parabolic patterns at an average rate of $-2.0 \mu\text{m}/\text{year}$ over 60 months.



Model	RNFL thickness change function
Linear:	$\mu_m - \mu_0 = -2 \times \frac{m}{12}$
Episodic:	$\mu_m - \mu_0 = \begin{cases} 0 & \text{if } m = 0 \\ (\mu_{m-4} - \mu_0) & \text{if } m = 4, 8, 12, 28, 32, 36, 52, 56, 60 \\ (\mu_{m-4} - \mu_0) = \frac{10}{6} & \text{if } m = 16, 20, 24, 40, 44, 48 \end{cases}$
Exponential:	$\mu_m - \mu_0 = -10 \times \frac{e^{-m/12} - 1}{e^{-60/12} - 1}$
Parabolic:	$\mu_m - \mu_0 = -10 \times \left(\frac{m/12}{60/12}\right)^2$

Figure 3.1.2 Schematics illustrating simulation of 16 serial average retinal nerve fiber layer (RNFL) thickness measurements over 60 months. Each measurement was derived from an independent normal distribution with a mean of $100\ \mu\text{m}$ and a within-subject standard deviation. (A) illustrates a simulation with a small test-retest variability of $0.74\ \mu\text{m}$. (B) illustrates a simulation with a large test-retest variability of $3.50\ \mu\text{m}$. RNFL progression was modeled by imposing a specific pattern of progression at a specific rate of change on the simulated dataset. (C) illustrates a simulation with linear reduction of average RNFL thickness at a rate of $-2.0\ \mu\text{m}/\text{year}$ was imposed in an eye with a small test-retest variability ($\text{SD} = 0.74\ \mu\text{m}$).

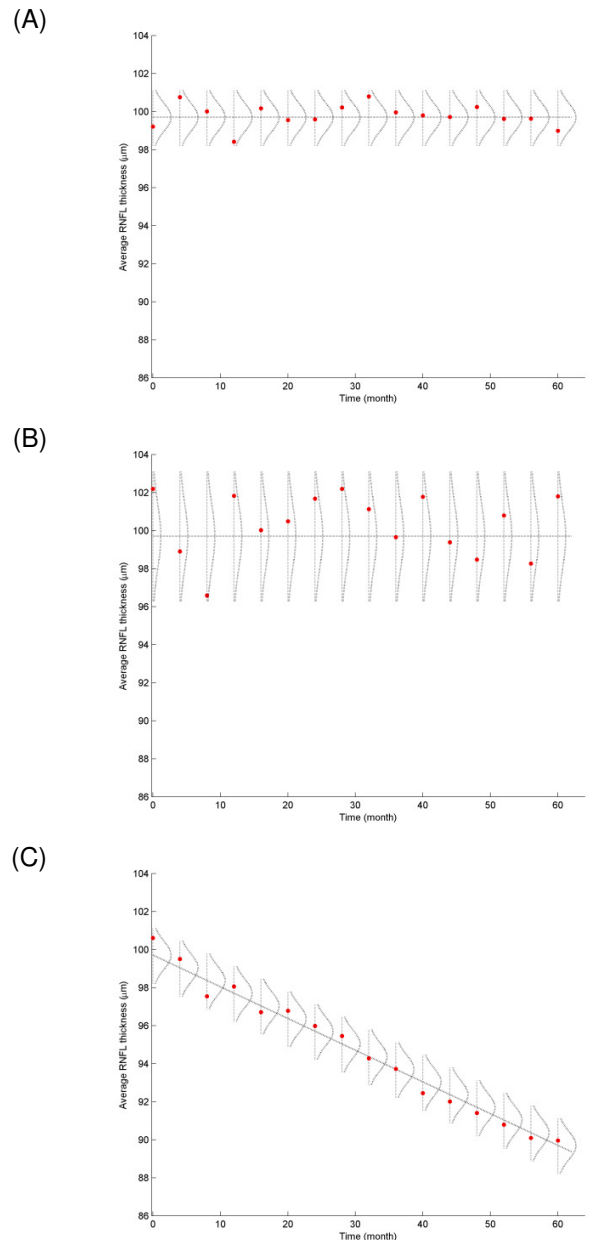


Figure 3.1.3 Sensitivity profiles for detection of retinal nerve fiber layer (RNFL) progression by trend and event analyses computed from month 12 to month 60. Progressive average RNFL thickness reduction was modeled at a rate of $-2 \mu\text{m}/\text{year}$ for linear (A, E, I), episodic (B, F, J), exponential (C, G, K) and parabolic (D, H, L) patterns for eyes with small (A-D), average (E-H) and large (I-L) test-retest variabilities.

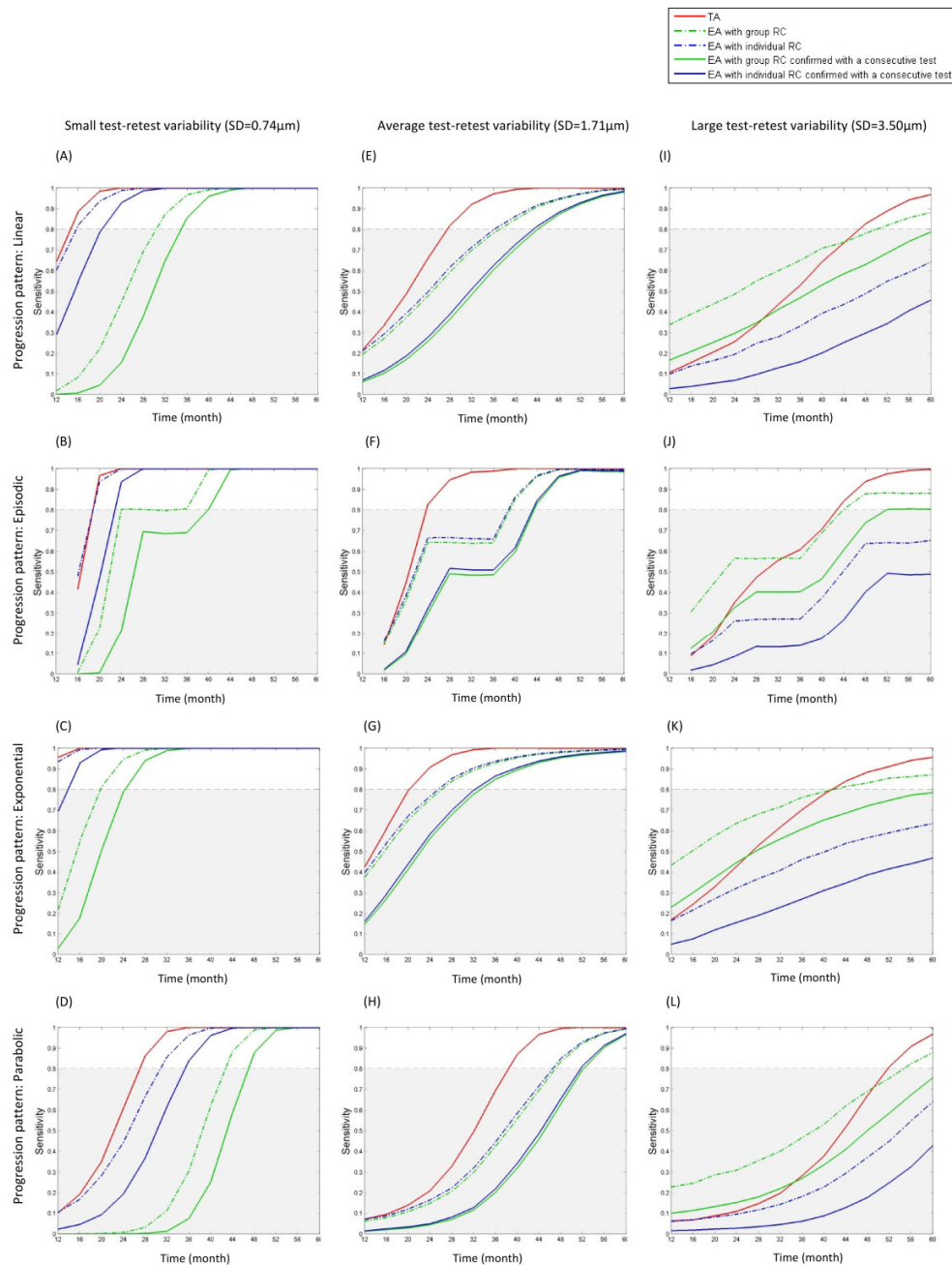
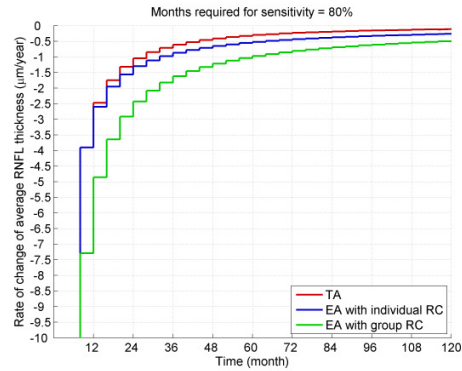
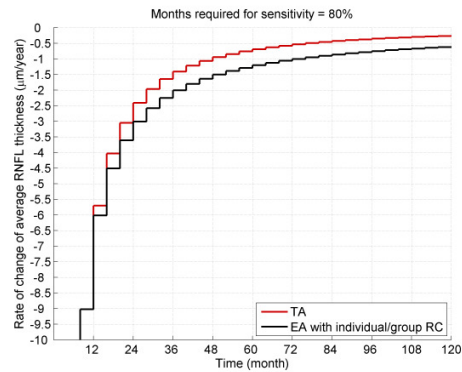


Figure 3.1.4 Relationship between the rate of linear change in average RNFL thickness and the minimum duration required for TA and EA to detect progression at a sensitivity of 80% in eyes with small (A), average (B), and large (C) test-retest variabilities.

(A) Small test-retest variability (SD=0.74 μm)



(B) Average test-retest variability (SD=1.71 μm)



(C) Large test-retest variability (SD=3.50 μm)

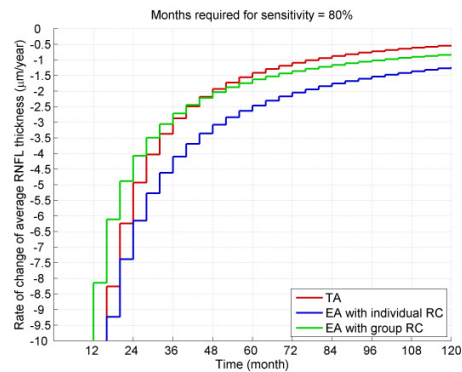


Figure 3.1.5 Sensitivity profiles for detection of retinal nerve fiber layer (RNFL) progression by trend and event analyses computed from month 12 to month 60. Progressive average RNFL thickness reduction was modeled at a rate of $-4 \mu\text{m}/\text{year}$ for linear (A, E, I), episodic (B, F, J), exponential (C, G, K) and parabolic (D, H, L) patterns for eyes with small (A-D), average (E-H) and large (I-L) test-retest variabilities.

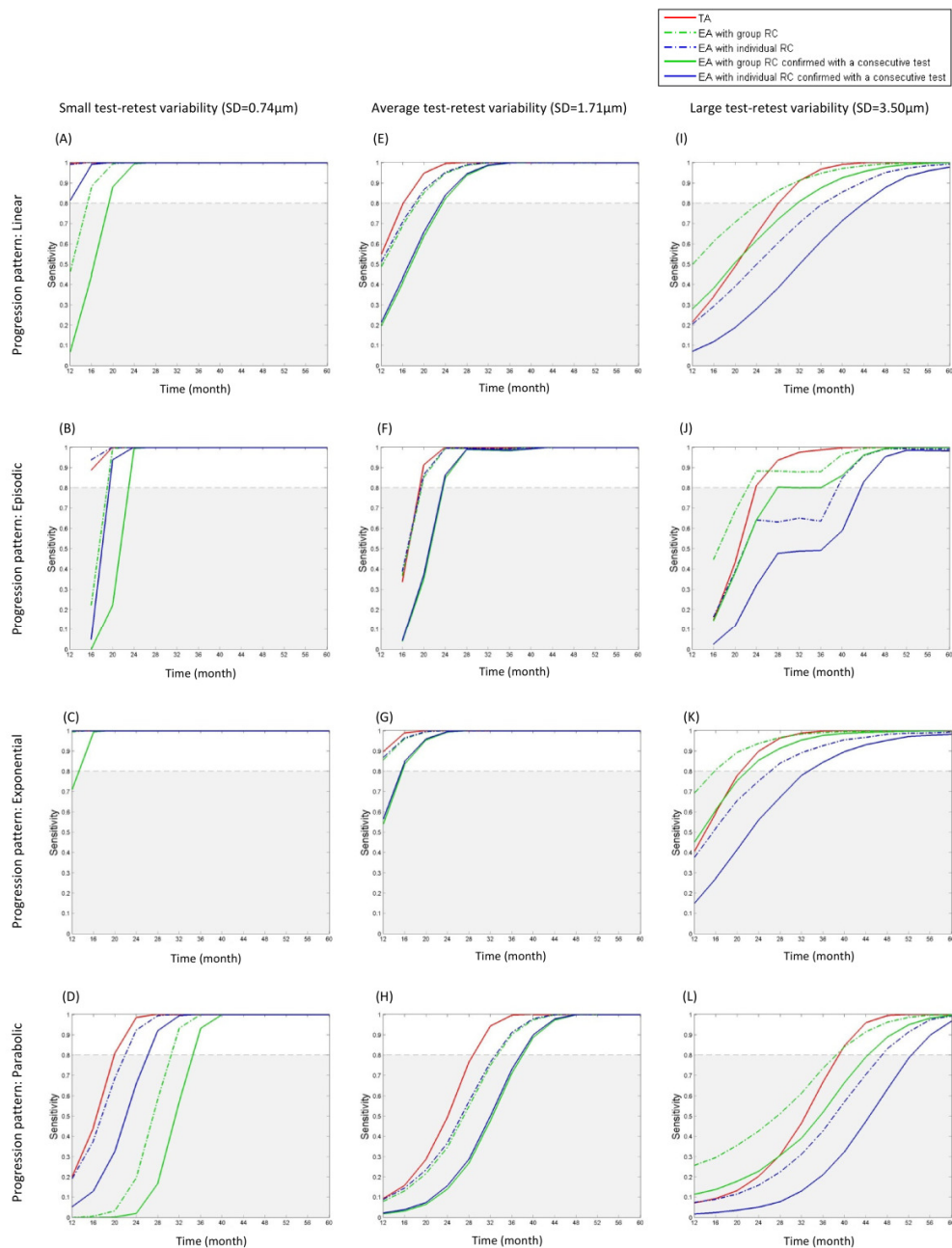
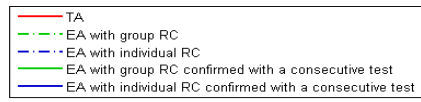
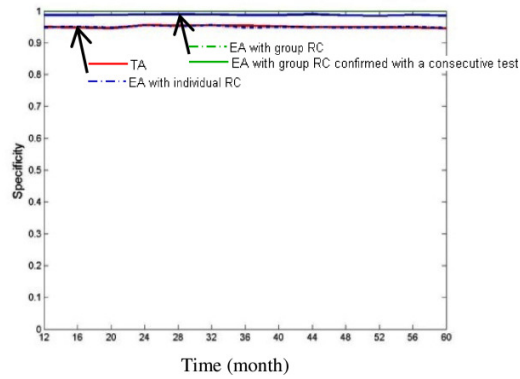


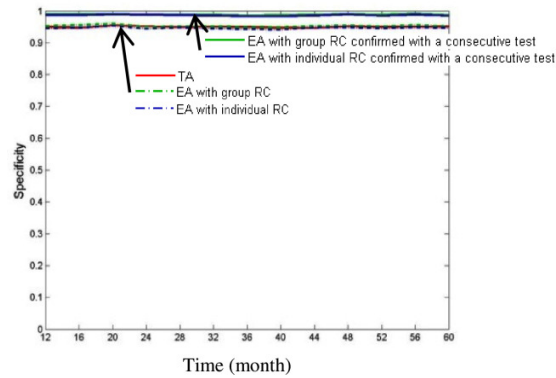
Figure 3.1.6 Specificity profiles of trend and event analyses for eyes with small (A), average (B) and large (C) test-retest variabilities computed from month 12 to month 60.



(A) Small test-retest variability (SD=0.74 μm)



(B) Average test-retest variability (SD=1.71 μm)



(C) Large test-retest variability (SD=3.50 μm)

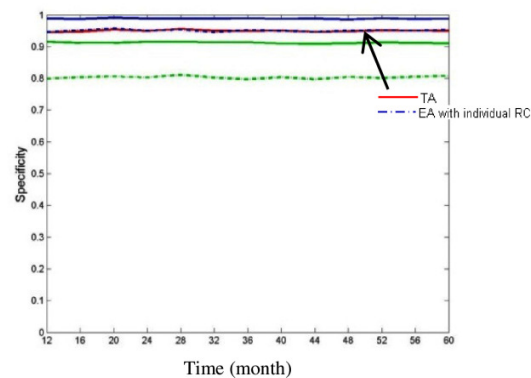


Figure 3.1.7 Accuracy profiles for detection of retinal nerve fiber layer (RNFL) progression by trend and event analyses computed from month 12 to month 60 in the simulation. Progressive average RNFL thickness reduction was modeled at a rate of $-2 \mu\text{m}/\text{year}$ for linear (A, E, I), episodic (B, F, J), exponential (C, G, K) and parabolic (D, H, L) patterns for eyes with small (A-D), average (E-H) and large (I-L) test-retest variabilities.

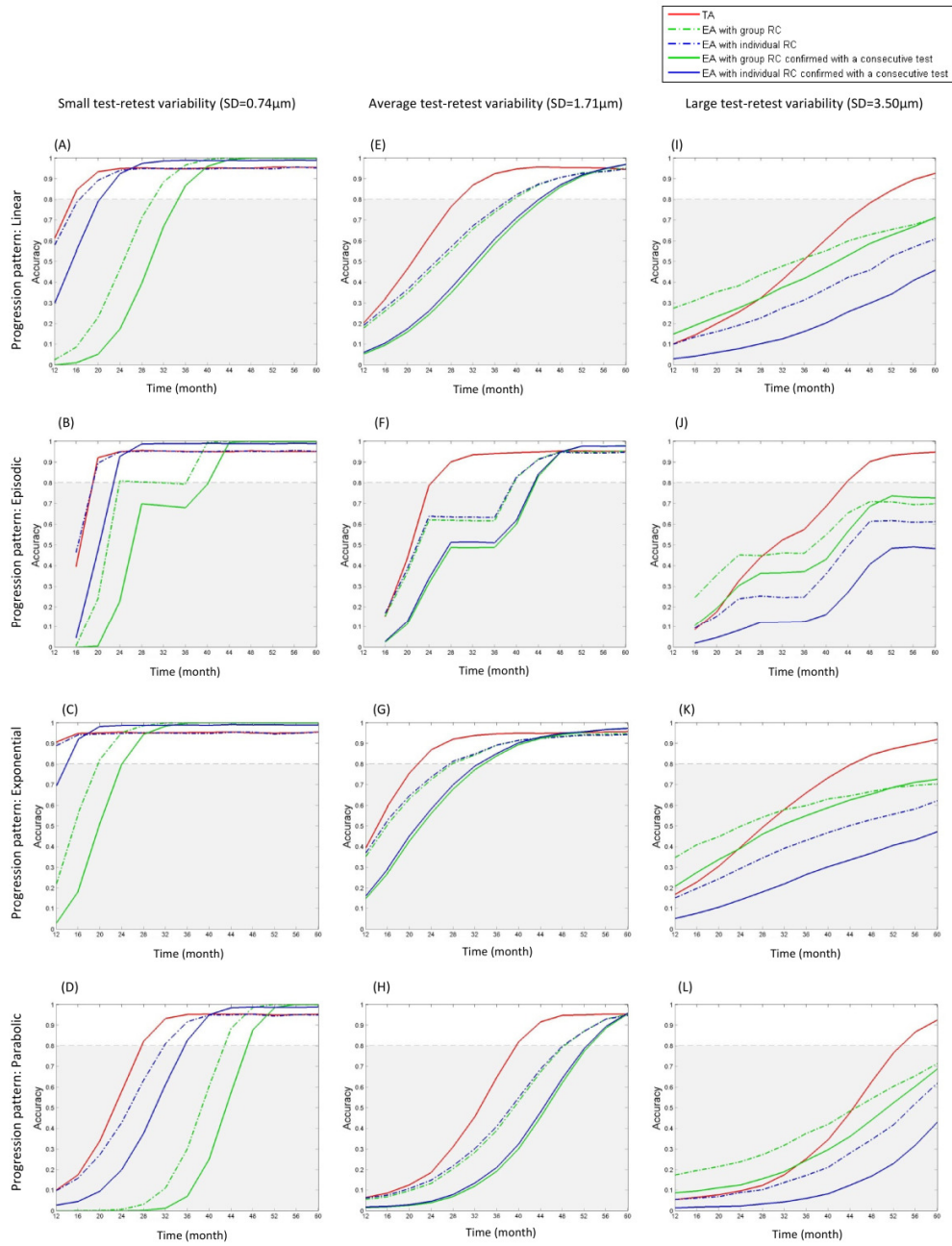


Figure 3.1.8 Accuracy profiles for detection of retinal nerve fiber layer (RNFL) progression by trend and event analyses computed from month 12 to month 60 in the simulation. Progressive average RNFL thickness reduction was modeled at a rate of $-4 \mu\text{m}/\text{year}$ for linear (A, E, I), episodic (B, F, J), exponential (C, G, K) and parabolic (D, H, L) patterns for eyes with small (A-D), average (E-H) and large (I-L) test-retest variabilities.

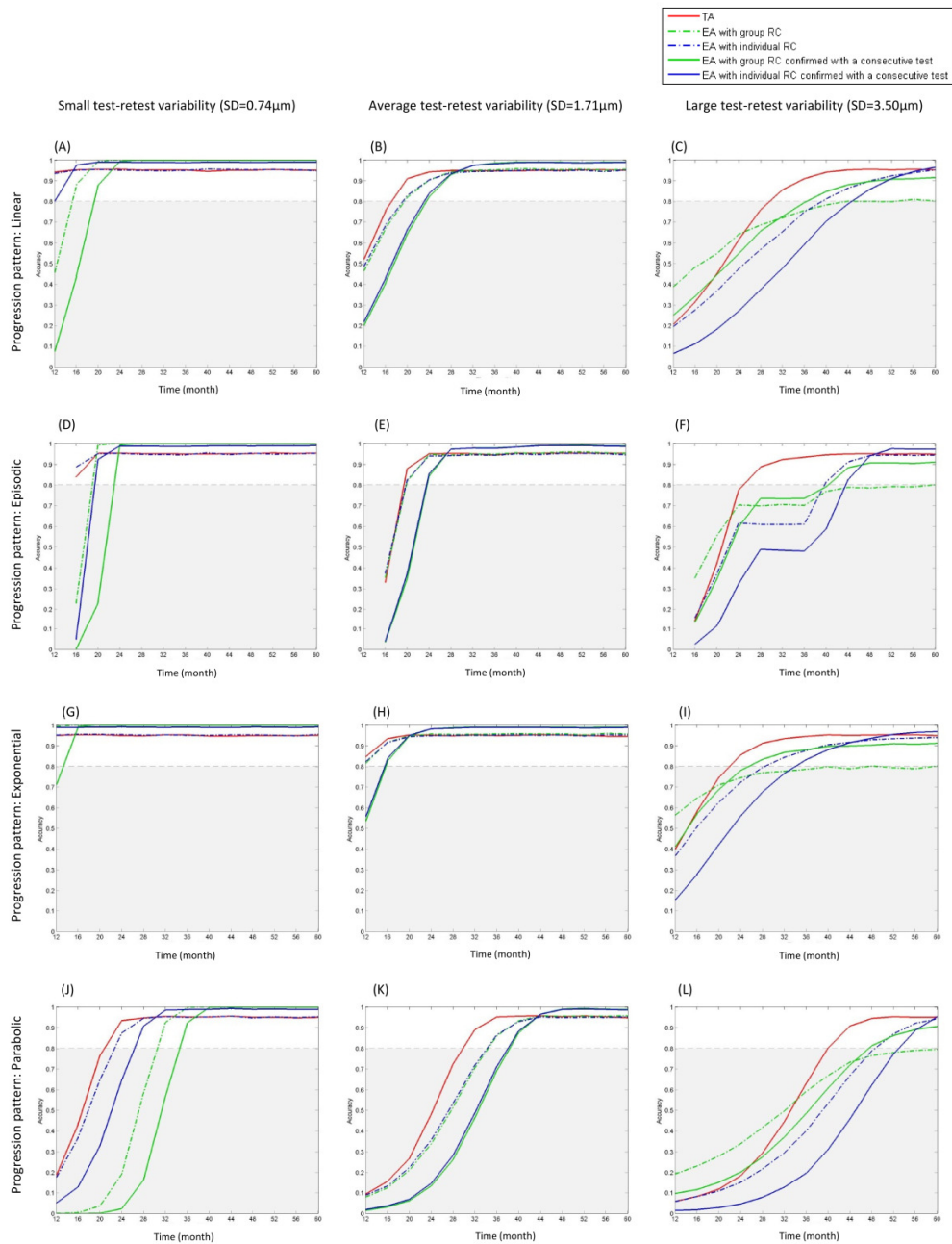


Figure 3.1.9 Proportion of eyes detected with retinal nerve fiber layer progression by TA and EA in 175 eyes of 81 glaucoma and 26 glaucoma suspect subjects (followed every 4 month for a median of 38 months) from month 12 to month 36 with average (A), small (B) and large (C) test-retest variability. Individual test-retest variability was estimated from the residuals of linear regression fitted on all available data of the particular eye. 123 eyes (70.3%) with test-retest variability of $1.77 \mu\text{m}$ at 10% level of significance were defined as the eyes with an average test-retest variability (A). The first 50 eyes with smallest estimated test-retest variability were arbitrarily defined as the eyes with a small test-retest variability (B) and the last 50 eyes with largest estimated test-retest variability were arbitrarily defined as the eyes with a large test-retest variability (C).

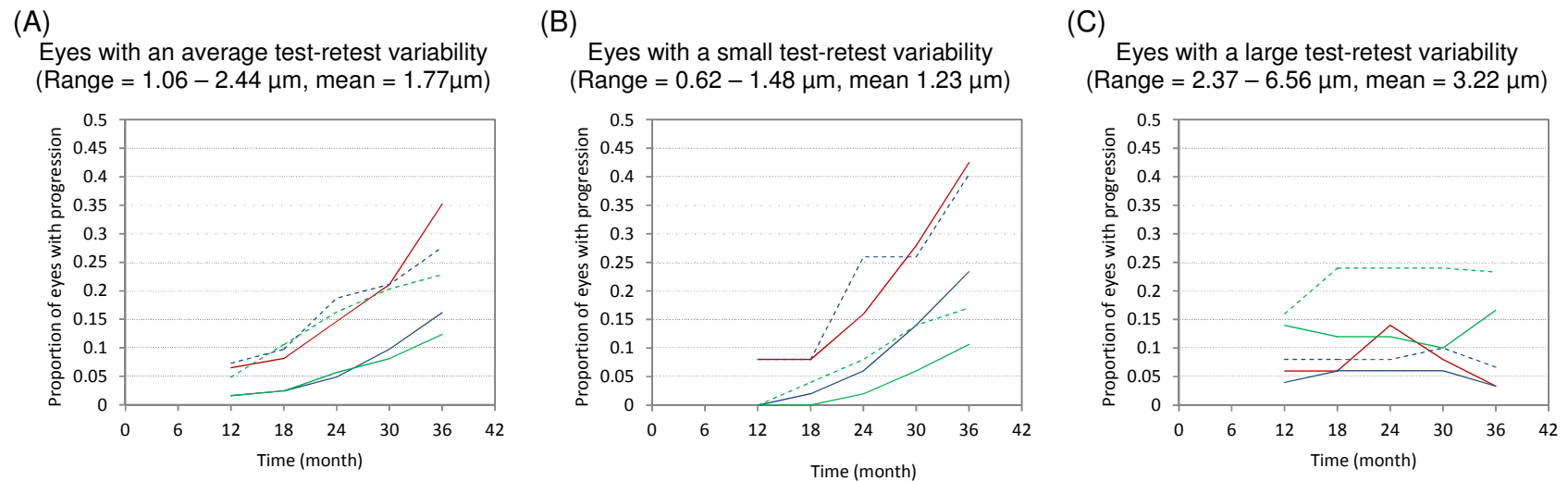


Figure 3.1.10 The impact of individual test-retest variability on the sensitivity and specificity of even analysis with group reproducibility coefficient (EA with group RC). The sensitivity and specificity can be represented by the area under the probability density function of the baseline measurement (mean= μ_1 and SD= σ) and the measurement of the n th visit (mean= μ_n and SD= σ), respectively, and the classification cut-off, $z_\alpha \sigma_g / \sigma$. If the individual test-retest variability, σ , equals to the group test-retest variability, σ_g , the sensitivity and specificity would be the same as EA with individual RC (A). If the individual test-retest variability, σ , is smaller than the group test-retest variability, σ_g , the classification cut-off, $z_\alpha \sigma_g / \sigma$, would shift to left resulting in a lower sensitivity and a higher specificity compared with EA with individual RC (B). If the individual test-retest variability, σ , is larger than the group test-retest variability, σ_g , the classification cut-off, $z_\alpha \sigma_g / \sigma$, would shift to right and resulting in a higher sensitivity and a lower specificity compared with EA with individual RC (C).

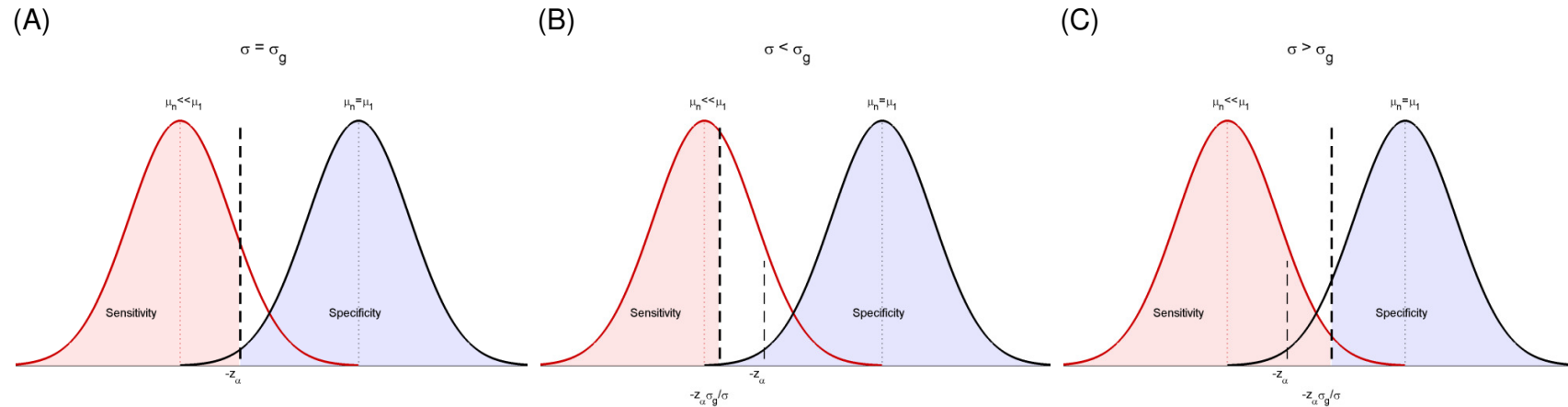
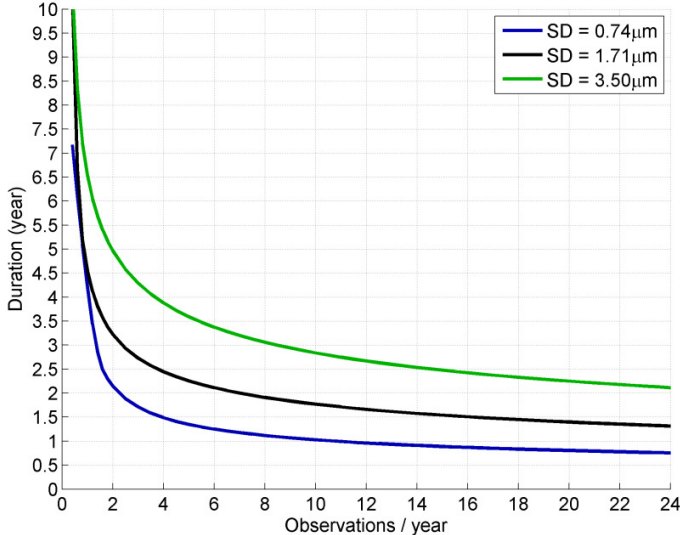
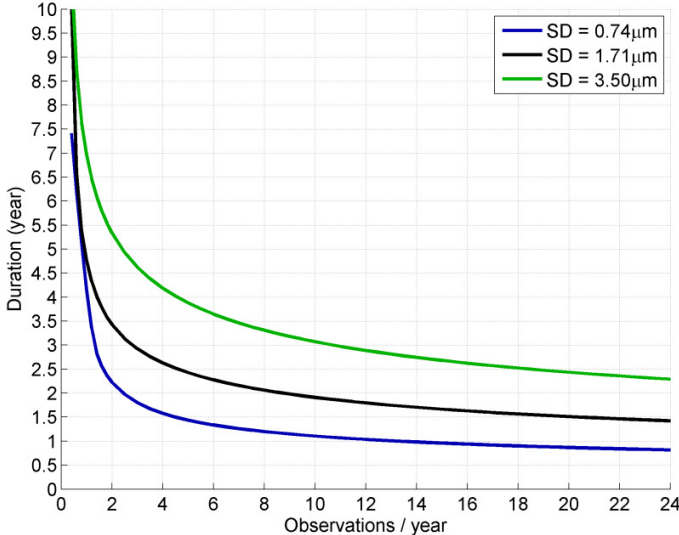


Figure 3.1.11 Relationship between the number of observations required per year and the minimum duration needed to detect a linear average RNFL thickness progression at rate of $-2 \mu\text{m}/\text{year}$ at a sensitivity of 70% (A) and 80% (B) for eyes with small ($\text{SD}=0.74 \mu\text{m}$), average ($\text{SD}=1.71 \mu\text{m}$), and large ($\text{SD}=3.50 \mu\text{m}$) test-retest variabilities.

(A)



(B)



3.2 Detection of Retinal Nerve Fiber Layer (RNFL) Progression using the RNFL thickness map

3.2.1 Abstract

Objectives: In the previous study, we showed that trend-based analysis generally attained high sensitive for detecting progressive reduction of average retinal nerve fiber layer (RNFL) earlier than event-based analysis with comparable specificity. Therefore, we set out to investigate if trend-based analysis on individual pixels data in the RNFL thickness maps (Trend-based Progression Analysis or TPA) would outperform Guided Progression Analysis (GPA) (an event-based counterpart) to detect change.

Methods: Individual pixel data of serial RNFL thickness maps of 68 eyes of 48 glaucoma subjects and 60 eyes of 34 normal subjects followed for a median of 55 months were exported from the Cirrus HD-OCT (Carl Zeiss Meditec). Linear regression analysis was performed on the individual pixels and the detection error in high dimensional multiple testing was quantified and controlled by the false discovery rate. The performance of detecting RNFL thinning was compared between TPA and GPA.

Results: Among the 68 eyes of 48 glaucoma subjects, RNFL progression was detected in 38 eyes (55.9%) by TPA and 23 eyes (33.8%) by GPA. The false discovery rates in the 38 eyes detected with

progression by TPA were all $\leq 5\%$. RNFL progression were detected by both techniques in 19 eyes with 12 eyes (60%) first detected by the TPA and 5 eyes (25%) first detected by the GPA. The survival probability of TPA was significantly lower than that of GPA ($p=0.012$). The proportion of RNFL progression detected by TPA and GPA was similar in the 60 eyes of 34 normal subject in which 4 eyes (6.7%) were detected by the TPA and 2 eyes (3.3%) were detected by the GPA. The survival probabilities between the two algorithms were not significantly different ($p=0.400$).

Conclusions: TPA outperformed GPA in detecting more number of progressing eyes at a similar level of specificity. With the analysis of the false discovery rate of the RNFL change map, TPA can provide a more informative approach to report progressive RNFL damage.

3.2.2 Background and Objectives

Although the advent of spectral-domain optical coherence tomography allows high-speed and high-resolution imaging of the retina nerve fiber layer (RNFL), detection of progressive RNFL thinning in glaucoma has been largely based on global parameters, such as the average, the superior average, and the inferior average RNFL thicknesses obtained from circumpapillary RNFL measurement. One commercially available spectral-domain OCT, the Cirrus HD-OCT (Carl Zeiss Meditec), provides statistical analysis - the Guided Progression Analysis or GPA to analyze progressive RNFL thinning in the RNFL thickness map. In GPA, a statistically significant RNFL thickness change at an individual pixel in the RNFL thickness map is defined when the difference between the two baseline and the follow-up examinations exceeds the test-retest variability of that particular pixel (the test-retest RNFL measurement variabilities of individual pixels are in-house proprietary data from Carl Zeiss Meditec). Significant RNFL thinning is displayed in the "RNFL Change Map". "Likely Loss" (when the change is detected in two consecutive follow-up visits), "Possible Loss" (when the change is detected in one follow-up visit), and "Possible Increase" (when the change is greater than the test-retest variability) are highlighted in red, yellow and purple, respectively, in the RNFL thickness change map. One shortcoming of GPA is the lack of accountability of the potential increase in Type 1 error in testing multiple pixels (50 x 50 superpixels in

the RNFL thickness change map). Without estimating the number of false positives, the interpretation of RNFL thickness change map would be difficult. In our previous study, we demonstrated that trend-based analysis generally attained high sensitivity for progression detection earlier than event-based analysis at a comparable level of specificity. We hypothesized that trend analysis of the RNFL thickness maps would provide a more informative and sensitive approach to detect RNFL change compared with GPA. In this study, Trend-based Progression Analysis (TPA) was developed. We also included the concept of false discovery rate (FDR), which was originally described Benjamini & Hochberg (Benjamini & Hochberg, 1995), to estimate the potential number of false positives in the RNFL thickness change map without sacrificing the potential loss in detection sensitivity as in Bonferroni adjustment. and the performance of TPA and GPA was then compared in a group of 82 subjects (48 glaucoma patients and 34 normal subjects) who had been followed for at least 36 months.

3.2.3 Subjects and Methods

3.2.3.1 Subjects

All subjects were enrolled from June 2007 to March 2013 at the University Eye Center, the Chinese University of Hong Kong. They underwent visual field examination using SAP (SITA Standard 24-2, HFA II, Carl Zeiss Meditec), spectral-domain OCT RNFL imaging (Cirrus

HD-OCT, Carl Zeiss Meditec) and full ophthalmic examination, including measurement of visual acuity, refraction, intraocular pressure and fundus examination as described in section 2.2 to 2.4. Subjects were classified into normal, glaucoma suspect or glaucoma subjects according to the definitions described in section 2.5. Based on the inclusion and exclusion criteria stated in section 2.2, 68 eyes of 48 glaucoma subjects (64 eyes with open-angle glaucoma and 4 eyes with angle-closure glaucoma) were examined every 4 months for at least 36 months (range 36 - 67 months with median of 60 months) for Cirrus HD-OCT RNFL imaging. Sixty eyes of 34 normal subjects followed for at least 36 months (range 36 - 65 months with median of 52 months) were also included to estimate the specificity of GPA and TPA.

3.2.3.2 Algorithm of Trend-based Progression Analysis

Individual pixel RNFL thickness values in the RNFL thickness maps were exported from the Cirrus HD-OCT (Carl Zeiss Meditec) and analyzed in MATLAB (The MathWorks, Inc., Natick, MA). Serial RNFL thickness maps from the same eye were registered with reference to the trajectories of the retinal blood vessels. After registering and aligning the retinal blood vessels in the longitudinal image series, a functional response and a scalar independent variable model was constructed:

$$f(s_0, t) = \alpha(s_0) + \beta(s_0)t + \varepsilon(s_0, t)$$

where t denotes time ($t = 0$ represents the time at the baseline examination); $f(s_0, t)$ denotes the RNFL thickness in a particular superpixel, $s_0 = (x_0, y_0)$, at time t ; $\alpha(s_0)$ is a functional constant representing the RNFL thickness at the baseline examination; $\beta(s_0)$ denotes the rate of change in RNFL thickness and $\varepsilon(s_0, t)$ denotes the random measurement error. (Ramsay & Dalzell, 1991)

Assuming the measurement error, ε , as a Gaussian process independent of time, t , local RNFL thickness change at the geographical location s_0 can be estimated by the ordinary least square (OLS) estimation,

$$\hat{\beta}(s_0) = \frac{\text{Cov}[t, f(s_0, t)]}{\text{Var}[t]},$$

with the baseline measurement estimated by

$$\hat{\alpha}(s_0) = \bar{f}(s_0, t) - \hat{\beta}(s_0)\bar{t}.$$

The null hypothesis of no RNFL thickness change, $H_0: \beta(s_0) = 0$, versus the alternative hypothesis of having RNFL thickness change, $H_0: \beta(s_0) \neq 0$, can be tested by using t-test with $n - 2$ degree of freedom by defining the extreme probability as $\mathcal{P} = \mathbb{P}\{x \geq \mathcal{T}(s_0) | X \sim T_{n-2}\}$, where $\mathcal{T}(s_0) =$

$$\left| \frac{\hat{\beta}(s_0) - \beta(s_0)}{S_{\hat{\beta}(s_0)}} \right|, S_{\hat{\beta}(s_0)} = \sqrt{\frac{\frac{1}{n-2} \sum_{i=1}^n \{f(s_0, t_i) - [\hat{\alpha}(s_0) + \hat{\beta}(s_0)t_i]\}^2}{\sum_{i=1}^n (t_i - \bar{t})^2}},$$

and n represents the number of longitudinal observations used. The hypothesis of no local

RNFL thickness change would be rejected if \mathcal{P} is less than or equal to the predefined level of significance for a single test.

The TPA derived RNFL thickness change map can be generated by performing the functional response regression analysis in individual superpixel of the RNFL thickness map.

The RNFL thickness map obtained by the "Optic Disc Cube 200x200" protocol in the Cirrus HD-OCT (Carl Zeiss Meditec, Dublin, CA) contains 200 x 200 (40,000) localized RNFL thickness measurements in an area of 6x6 mm² around the optic disc. To reduce the amount of model fitting and hypothesis testing without substantial loss of image resolution, the RNFL thickness map was partitioned into 4x4 pixels (a superpixel). Model fitting and hypothesis testing were performed using the average RNFL thickness calculated from each partition.

3.2.3.3 Measurement of False Discovery Rate (FDR)

With multiple regression analyses performed in the high density RNFL thickness map, it is important to quantify and control the detection error of RNFL thickness change. The false discovery rate (*FDR*) introduced by Benjamini and Hochberg was used to quantify the detection error, which is defined as

$$FDR = \mathbb{E} \left[\frac{\text{number of false positive detection}}{\text{number of positive detection}} \right]$$

(Benjamini & Hochberg, 1995).

The supremum of the FDR can be estimated by

$$\widehat{\text{sup}}(FDR) = \frac{\text{number of tests} \times \text{sig. level used for a single test}}{\text{number of positive detection}}$$

False discovery rate can be controlled by the Benjamini Hochberg procedure and the enhanced approach by a two-stage procedure suggested by Benjamini et al. (Benjamini & Hochberg, 1995, Benjamini & Hochberg, 1997, Benjamini & Yekutieli, 2001, Benjamini et al., 2006)

The Benjamini Hochberg FDR controlling procedure

- Set a predefined FDR level (the desired supremum), q . Order all the single location extreme probabilities as

$$\mathcal{P}_{(1)} \leq \mathcal{P}_{(2)} \leq \dots \leq \mathcal{P}_{(m)}$$

- Find $k = \max \left\{ j: \mathcal{P}_{(j)} \leq \frac{jq}{m} \right\}$, and reject the hypotheses of no change in all locations when $\mathcal{P} \leq \frac{kq}{m}$.

By rejecting the k hypotheses of no change in all locations with $\mathcal{P} \leq \frac{kq}{m}$,

the supremum of the $FDR = \frac{m\mathcal{P}}{k}$ would be smaller than the desired level

q .

The two-stage procedure (with equal weighting)

1. Set a predefined FDR level (the desired supremum), q , and define $q' = \frac{q}{q+1}$. Order all the single location extreme probabilities as

$$\mathcal{P}_{(1)} \leq \mathcal{P}_{(2)} \leq \dots \leq \mathcal{P}_{(m)}$$

and find $k = \max\left\{j: \mathcal{P}_{(j)} \leq \frac{j\alpha'}{m}\right\}$, where m is the total number of t-test performed in the whole map.

2. Find $k_2 = \max\left\{j: \mathcal{P}_{(j)} \leq \frac{j\alpha'}{m-k}\right\}$, and reject the hypotheses of no change in all locations when $\mathcal{P} \leq \frac{k_2\alpha'}{m-k}$.

In the TPA RNFL thickness change map, RNFL thinning in a super-pixel would be highlighted in yellow if a significant negative slope was found at 5% level of significance, and in red if a negative slope was found and the hypothesis of no change was rejected at a false discovery rate of 5% controlled by the two-stage procedure (examples are illustrated in Figure 3.2.1 and 3.2.2). A superpixel would be highlighted in purple if a positive slope was found and the hypothesis of no change was rejected at a false discovery rate of 5% controlled by the two-stage procedure.

3.2.3.4 Definition of RNFL progression

In both GPA and TPA, RNFL progression was defined if a contiguous cluster of ≥ 10 superpixels (1 superpixel=4x4 pixels) was coded in red in the corresponding RNFL change maps in the latest follow-up examination.

3.2.3.5 Statistics

Statistical analyses were performed with MATLAB R2010a (The MathWorks, Inc., Natick, MA) and R version 2.15.2 (R Foundation,

Vienna, Austria). Computer programs were written in MATLAB for image registration, detecting progressive RNFL thinning in the RNFL thickness map, and quantifying the false discovery rate. R was used for agreement analysis and comparing the area of detection between GPA and TPA, estimating the rate of change of average RNFL thickness, and non-parametric survival analysis of TPA and GPA. Agreement analysis between GPA and TPA was based on Cohen's kappa (Cohen, 1960). Comparison of the area of detection between GPA and TPA was based on Wilcoxon signed rank test. The rate of change of average RNFL thickness was estimated by linear mixed model with all eyes treated as independent. In the survival analysis, the events of interests were the time to first detection of RNFL progression with a contiguous cluster of ≥ 10 superpixels (1 superpixel=4x4 pixels) coded in red in the TPA and GPA RNFL change maps, respectively, since subjects were enrolled. The survival probabilities were estimated by Kaplan–Meier estimator and compared by log-rank test. $p < 0.05$ were considered statistically significant.

3.2.4 Results

A total of 1690 OCT images from 68 eyes of 48 glaucoma patients (23 eyes with and 45 eyes without evidence of progression detected in the RNFL thickness change map by the GPA) and 60 eyes of 34 normal subjects prospectively followed for at least 36 months (a mean follow-up

period of 55 months) were included. The demographics, visual field and average RNFL measurements are shown in Table 3.2.1.

3.2.4.1 Comparison of detection of progressive RNFL thinning between GPA and TPA in eyes with glaucoma

Among the 23 eyes with evidence of GPA progression, TPA detected progressive RNFL damage in all but 4 eyes. For the 45 eye without GPA progression, 19 had progression by TPA. The false discovery rates in the 38 eyes detected with progression by TPA were all $\leq 5\%$. Among the 19 eyes with progressive RNFL thinning detected by both algorithms, 12 (63.2%) were detected by TPA 4 – 26 months earlier than GPA, 2 (10.5%) were detected by TPA and GPA at the same time, and 5 (26.3%) were detected by GPA 4 – 12 months earlier than TPA. The agreement of progression detection between the two algorithms was fair (kappa: 0.348, 95% confidence interval: 0.132 – 0.565) (Figure 3.2.3). Figure 3.2.4 shows the survival probabilities of GPA and TPA estimated by the Kaplan–Meier estimators. The survival probability of TPA was significantly lower than that of GPA (log-rank test, $p=0.012$), indicating that TPA detected progressive RNFL thinning earlier than GPA. Figure 3.2.5 shows the overlay of the RNFL change maps obtained in the latest follow-up analyzed by GPA and TPA. Notably, while both algorithms indicated that the superotemporal and inferotemporal sector were the most frequent location where progressive RNFL thinning was detected,

TPA detected a greater area of progressive RNFL thinning compared with GPA ($p=0.001$).

Rate of RNFL loss in the RNFL map

The rate of change of average RNFL thickness in the 38 progressing eyes detected by TPA was $-1.00 \mu\text{m}/\text{year}$. For individual pixel RNFL thicknesses, the rates of change ranged between $-42.26 \mu\text{m}/\text{year}$ and $0.23 \mu\text{m}/\text{year}$.

Examples

Figure 3.2.1 is an example of a glaucomatous eye with RNFL progression detected by the Cirrus HD-OCT GPA (Figure 3.2.1 A) and TPA (Figure 3.2.1 B). The same data set was used to illustrate the differences between GPA and TPA. While significant RNFL thinning was detected by GPA in November 2009, it is not known if the detected changes were false positives. By contrast, TPA revealed RNFL progression for the same set of images in July 2009, 4 months earlier than GPA, with a false detection rate of 5% (coded in red). Figure 3.2.1 C shows that the detection can be displayed in a color-coded map indicating the rates of change of RNFL thickness at individual pixel partitions in the latest follow-up visit. Figure 3.2.2 A shows another example of a glaucomatous eye with RNFL progression detected by the GPA in May, 2012. Notably, TPA detected progressive RNFL thinning as early as January 2011 with a false discovery rate of 5%, fully 16

months earlier (Figure 3.2.2 B). The detection was displayed in a color-coded map showing the rates of change of RNFL thickness at individual pixel partitions in the latest follow-up visit in Figure 3.2.2 C. In both examples, TPA detected progressive RNFL thinning earlier than GPA and the area of change was greater TPA than that of GPA.

3.2.4.2 Specificity of GPA and TPA

TPA detected 4 (6.7%) and GPA detected 2 (3.3%) eyes with progressive RNFL thinning in the normal group and the estimated specificity was 93.3% and 96.7%, respectively. One normal eye was detected with progressive RNFL thinning by both algorithms (Figure 3.2.6). There was no significant difference in the survival probability between the TPA and GPA in the normal eyes (log-rank test, $p=0.400$) (Figure 3.2.7).

3.2.5 Discussion

3.2.5.1 Trend-based analysis in detecting RNFL thinning in the RNFL thickness maps

To our knowledge, this is the first investigation to apply trend-based analysis to evaluate progressive RNFL thinning in the RNFL thickness map. With TPA, we showed that progressive RNFL thinning can be detected earlier than GPA (Figures 3.2.1 and 3.2.2) at a comparable level of specificity and there was a significant difference in the survival probability between the two algorithms for detection of RNFL

progression in glaucoma patients. This finding concurs with our previous study demonstrating that trend-analysis outperformed event analysis in detection of RNFL progression in glaucoma.

The GPA of the RNFL thickness map is an event-based analysis which does not provide the rates of change of RNLF thickness in individual pixels. The rates of change of RNFL thickness map derived from the TPA (Figure 3.2.1 C and 3.2.2 C) provides a clear visualization of the distribution pattern of the rates of RNFL loss. These data may provide prognostic information in predicting the severity and location of subsequent visual field loss and guiding treatment in glaucoma management. Investigation is ongoing to address the predictive power of the TPA in locating subsequent visual field damage in glaucoma patients.

3.2.5.2 The importance of reporting false discovery rate

In the detection of RNFL changes in the RNFL thickness map, a large number of hypothesis testing is involved. Defining significant RNFL changes based on individual p values may lead to multiple false detections. Controlling the family-wise error rate (FWER) by algorithm such as Bonferroni adjustment would require a p value less than $0.05/(50 \times 50) = 0.00002$, rendering the detection of change not sensitive. For this reason, we use the false discovery rate introduced by Benjamini & Hochberg (Benjamini & Hochberg, 1995) in the TPA. The

false discovery rate is important for the map analysis because it can provide a more informative interpretation of the detected RNFL changes without sacrificing potential loss in the detection sensitivity. For example, an area of RNFL thinning of 100 superpixels detected with a $FDR = 5\%$ in the RNFL thickness change map suggests that 5 out of the 100 superpixels would likely be false positives. A limitation of the FDR is that it does not account the likelihood of progressive RNFL thinning that occurs in contiguous clusters. One approach to tackle this issue is the statistic image mapping (SIM) technique introduced by Patterson (Patterson et al., 2005). In their study, SIM detected changes in ONH topography images with an algorithm that quantified the occurrence likelihood of contiguous clusters. It is estimated by permutation testing, which is based on shuffling the pixel-wise analyses on the image to obtain the permutation distribution of the largest cluster size. Applying permutation testing for the detected clusters would provide more reliable estimates of RNFL change.

3.2.5.3 Extension of TPA

i. Higher order linear or non-linear models

Although the functional regression model evaluated in this study was limited to simple linear regression on individual pixels of the RNFL thickness maps, it is possible to extend the application to quadratic or higher order linear, or non-linear models.

ii. Discriminating glaucomatous RNFL changes from age-related RNFL changes

Knowledge regarding the age-related RNFL changes in normal eyes can be constructed by point-wise linear mixed model, such as

$$f_i(s_0, t) = (\beta_{0,N}(s_0) + \beta_{1,N}(s_0)t) + (u_{0,N,i}(s_0) + u_{1,N,i}(s_0)t) + \varepsilon_i(s_0, t),$$

where $\beta_{1,N}(s_0)$ represents the overall rate of age-related RNFL change in normal eyes, and $u_{1,N,i}(s_0)$ represents the eye-specific deviation of the rate of age-related for eye i . Eye-specific RNFL change would be considered as glaucomatous loss if the reduction is greater than the $(\alpha \times 100)$ th percentile of the age-related RNFL changes, $\beta_{1,N}(s_0) - z_\alpha \sigma_{\beta_{1,N}}(s_0)$, where $\sigma_{\beta_{1,N}}(s_0)$ represents the eye-specific standard deviation of the random effect $u_{1,N,i}(s_0)$.

iii. Modeling pixel RNFL change with consideration of the adjacent pixels

RNFL thicknesses in the geographical location, s_0 , can take into account the adjacent locations of s_0 (denoted by δ_{s_0} , which is called the geographical neighborhood of s_0) by Functional Autoregressive Moving Average (*functional* ARMA(p, q)) process:

$$f(s_0, t) = \sum_{i=1}^p \int_{s \in \delta_{s_0}} \varphi_i(s_0, s) \times f(s, t - i) ds$$

$$+ \sum_{j=0}^q \{m_j(s_0) \times \varepsilon(s_0, t - j)\} + \beta(s_0, t)$$

where $\varphi_i(s_0, s)$ is the weighting parameter of the i th prior RNFL thickness at location s corresponding to the subsequent RNFL thickness at location s_0 , $m_j(s_0)$ is the weighting parameter of the j th prior measurement error, and $\beta(s_0, t)$ is a time related function representing the general change of RNFL thickness regardless of any prior thickness information. Change in RNFL thickness map can be determined by performing stationary test on $f(s_0, t)$ (i.e. testing $E(f(s_0, t)) = \text{constant}$). However, the application of this model is limited to the measurements of the RNFL thickness are obtained in regular time intervals. On the other hand, if the examination intervals are sporadic, smoothing, such as kernel smoothing or kriging prediction (Kriging, 1951), can be applied to approximate the RNFL thickness profile in regular intervals and the *functional ARMA(p, q)* can be applied. Alternatively, continuous-time *functional ARMA(p, q)* can be applied, which is expressed in form of a stochastic partial differential equation (SPDE):

$$\frac{\partial^p}{\partial t^p} f(s_0, t) = \sum_{i=0}^{p-1} \int_{s \in \delta_{s_0}} \varphi_i(s_0, s) \frac{\partial^i}{\partial t^i} f(s, t) ds$$

$$+ \sum_{j=0}^q \left\{ m_j(s_0) \frac{\partial^j}{\partial t^j} \varepsilon(s_0, t) \right\} + \beta(s_0, t)$$

where $\frac{\partial^n}{\partial t^n}$ is the n -th stochastic partial derivative with respect to t and ε is a white noise process.

iv. Modeling RNFL change with consideration of the shape, smoothness, and the curvature of the RNFL profile

TPA is considered as a functional regression model since the RNFL thickness maps are considered as a spatio-temporal functional data instead of a series of two dimensional array of numerical data. By considering the RNFL thickness map as a functional data, information such as smoothness, $\frac{\partial}{\partial s} f(s, t)$, and curvature, $\frac{\partial^2}{\partial s^2} f(s, t)$, of RNFL thickness map can be modeled in the analysis of RNFL change, where $\frac{\partial^k}{\partial s^k}$ is the k -th ordinary partial derivative with respect to s (Ramsay & Dalzell, 1991). Further investigation is needed for the applications of these extensions of the trend-based analysis on the RNFL thickness maps. In particular, it is believed that investigation about the spatio-temporal correlation, the change in shape, the change in smoothness and the change in curvature of the RNFL thickness map might be able to provide valuable insight for discriminating glaucomatous from age-related changes.

3.2.5.4 Conclusions

TPA outperformed GPA in detecting more number of eyes with progressive RNFL changes in the RNFL thickness change map in an

earlier follow-up time point. With the inclusion of the rates of RNFL change map and the false discovery rate, informative interpretation of significant changes in the RNFL thickness change map can be attained. Further studies are needed to investigate the possible extensions of TPA application and their clinical significance in glaucoma management.

Table 3.2.1 Demographics, RNFL, and visual field measurements of 68 eyes of 48 glaucoma subjects and 60 eyes of 34 normal subjects who were followed up every 4 months for at least 36 months.

	Mean ± SD	
	<u>Glaucoma Group</u>	<u>Normal Group</u>
Spherical error (D)	-2.66 ± 4.15	0.33 ± 3.00
Age (year)	50.8 ± 14.6	67.1 ± 6.5
Signal strength	7.7 ± 0.8	8.4 ± 0.8
<u>Baseline examination</u>		
Average RNFL thickness (µm)	67.91 ± 12.31	102.91 ± 9.59
VFI (%)	73.56 ± 26.85	98.92 ± 1.30
Visual field MD (dB)	-9.81 ± 8.89	-0.88 ± 1.20
<u>Final examination</u>		
Average RNFL thickness (µm)	66.24 ± 12.29	102.50 ± 2.12
VFI (%)	72.14 ± 31.08	98.57 ± 2.07
Visual field MD (dB)	-10.51 ± 10.12	-1.21 ± 0.91
<u>Duration of follow-up (month)</u>		
Median	60	52
Minimum	36	36
Maximum	67	65

D = diopter; RNFL = retinal nerve fiber layer; VFI = visual field index; MD = mean deviation.

Figure 3.2.1 An example of retinal nerve fiber layer progression analysis evaluated the Guided Progression Analysis (GPA) (A) and the Trend-based Progression Analysis (TPA) (B). In the GPA "RNFL Change Maps", RNFL progression was first detected on November 2009 (A). In the TPA, significant localized RNFL loss at 5% level were highlighted in yellow, significant loss with false discovery rate $\leq 5\%$ were highlighted in red, and significant increases with false discovery rate $\leq 5\%$ were highlighted in purple. RNFL progression was first detected on July 2009, which was 4 months earlier than the detection in GPA (B). The rates of change of RNFL thickness at individual superpixels in the latest follow-up with significant changes at 5% false discovery rate are shown in a color-coded map with the color-coded scale on the right (C).

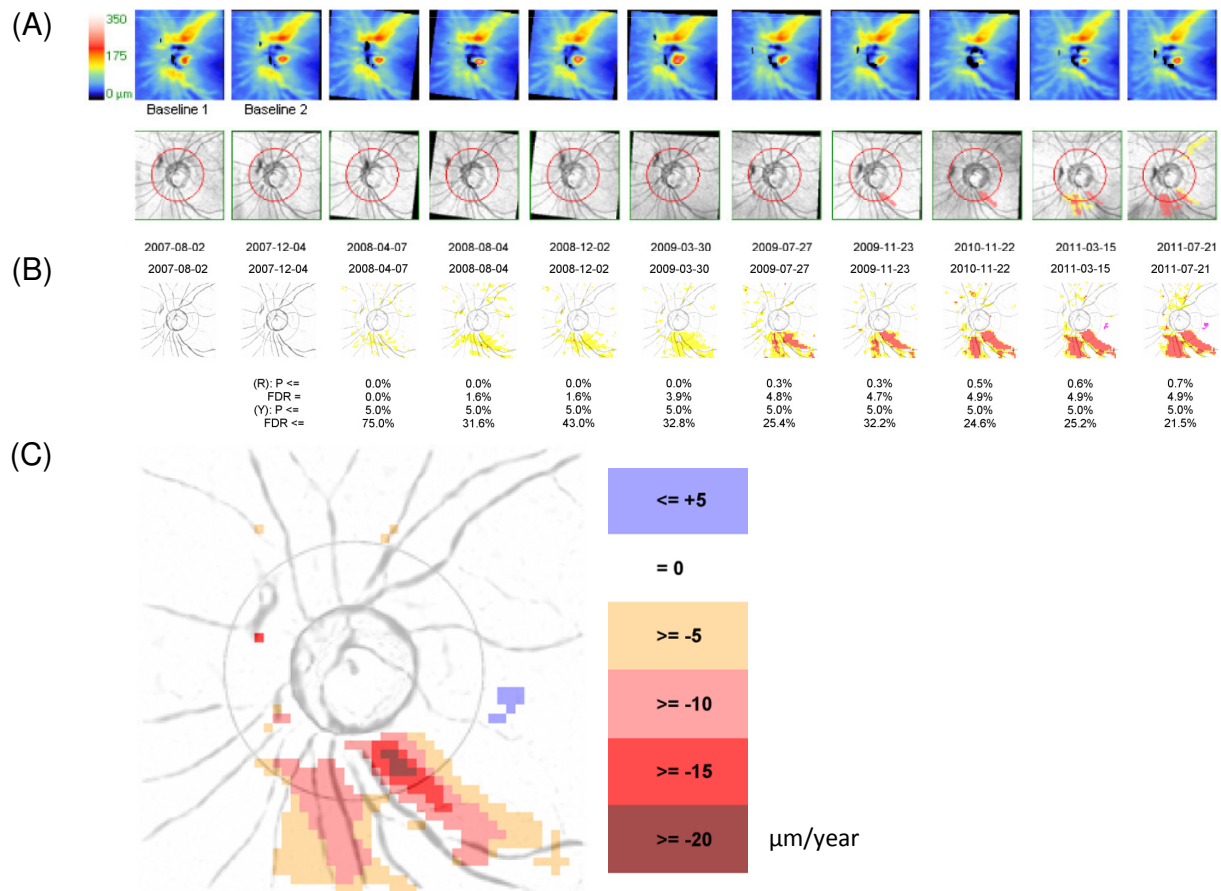


Figure 3.2.2 Another example of retinal nerve fiber layer progression analysis evaluated by the Guided Progression Analysis (GPA) (A) and the Trend-based Progression Analysis (TPA) (B). In the GPA "RNFL Change Maps", RNFL progression was first detected in May 2012 (A). In the TPA, significant RNFL loss at 5% level were highlighted in yellow, and significant loss with false discovery rate $\leq 5\%$ were highlighted in red. RNFL progression was first detected on January 2011, which was 16 months earlier than the detection in GPA (B). The rates of change of RNFL thickness at individual superpixels in the latest follow-up with significant changes at 5% false discovery rate are shown in a color-coded map with the color-coded scale on the right (C).

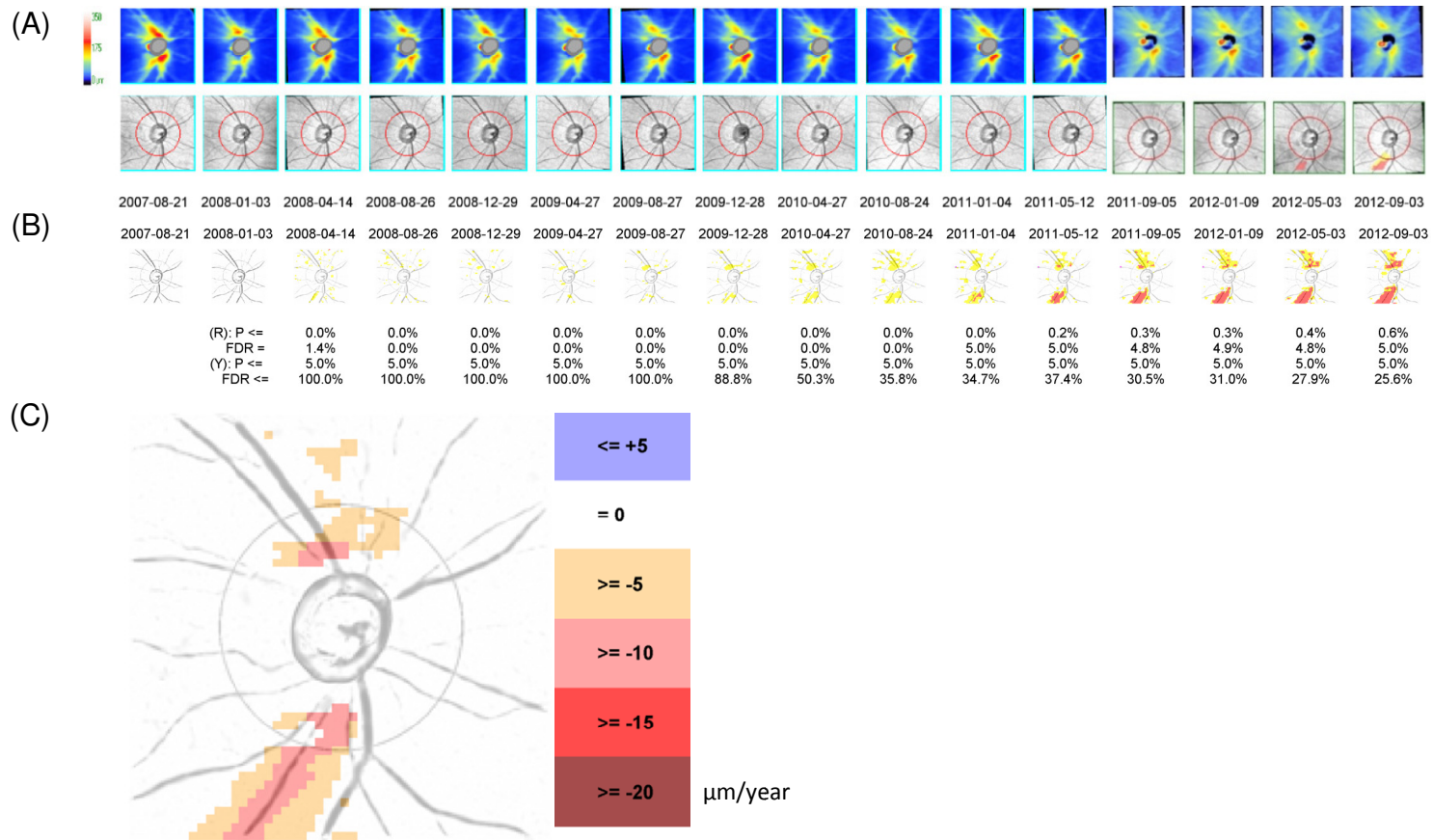
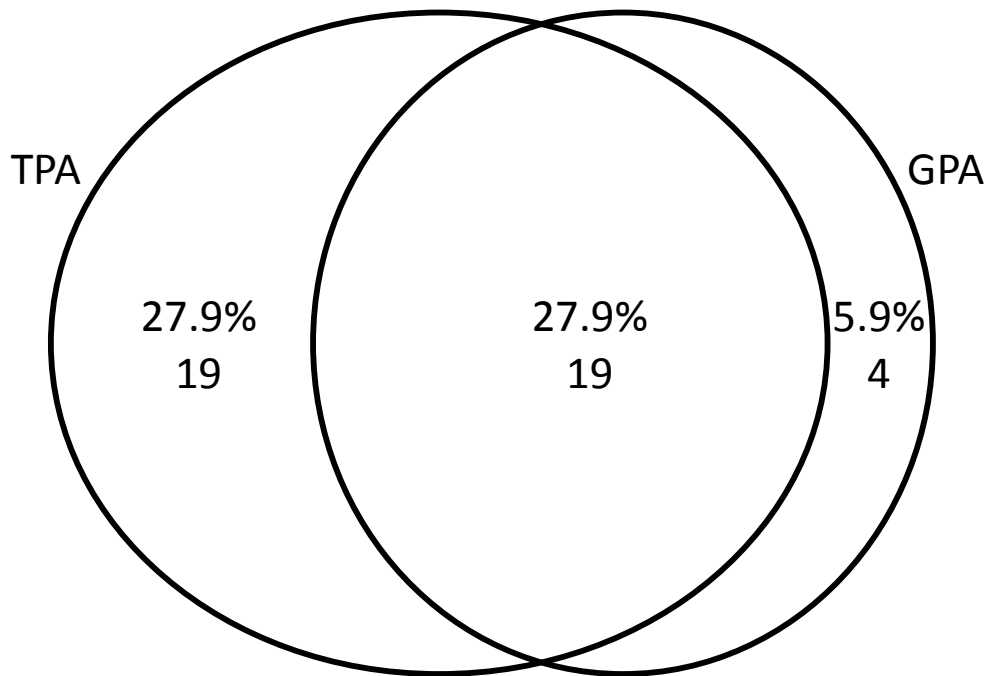


Figure 3.2.3 Agreement of the localized RNFL progression detected by the Trend-based Progression Analysis (TPA) and Guided Progression Analysis (GPA) in the glaucoma group.



Kappa = 0.348 (95% CI: 0.132 – 0.565)

CI=confidence interval.

Figure 3.2.4 Survival probabilities of Trend-based Progression Analysis (TPA) and Guided Progression Analysis (GPA) estimated by the Kaplan–Meier estimators in the glaucoma group.

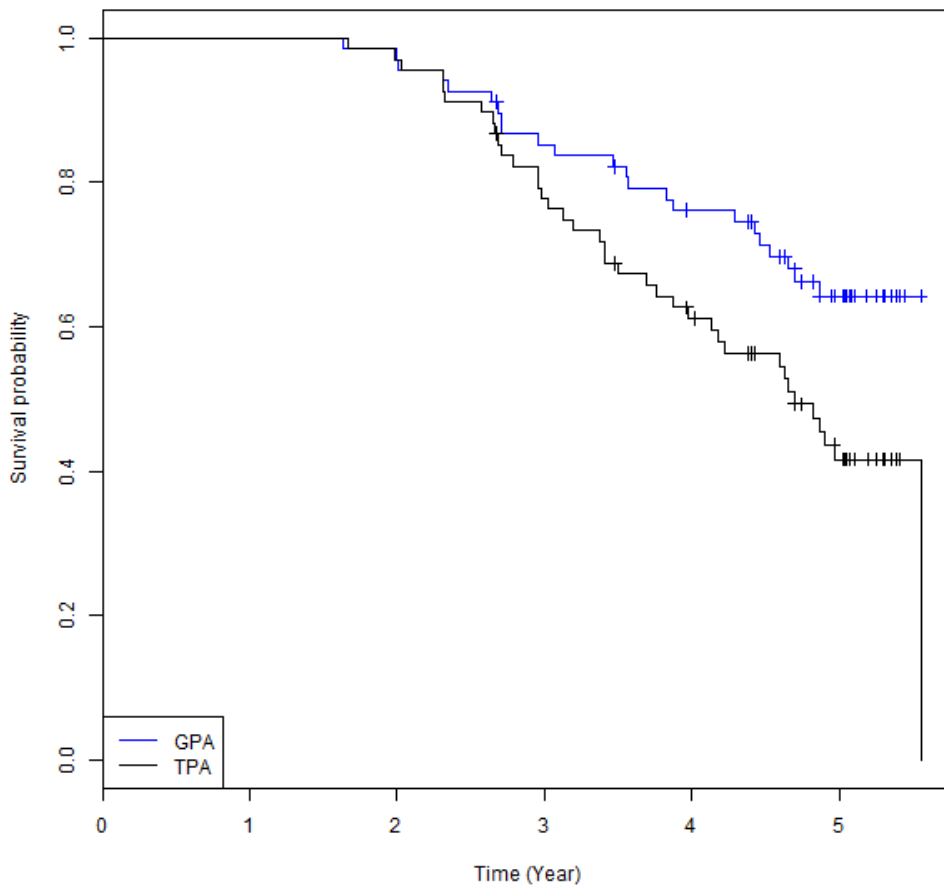


Figure 3.2.5 The overlay of the RNFL change maps obtained in the latest follow-up analyzed by Guided Progression Analysis (GPA) (A) and the Trend Progression Analysis (TPA) (B) in the glaucoma group. Area of RNFL thinning detected by GPA highlighted in red in 23 eyes (A). Area of RNFL thinning detected by by TPA highlighted in red in 38 eyes (B).

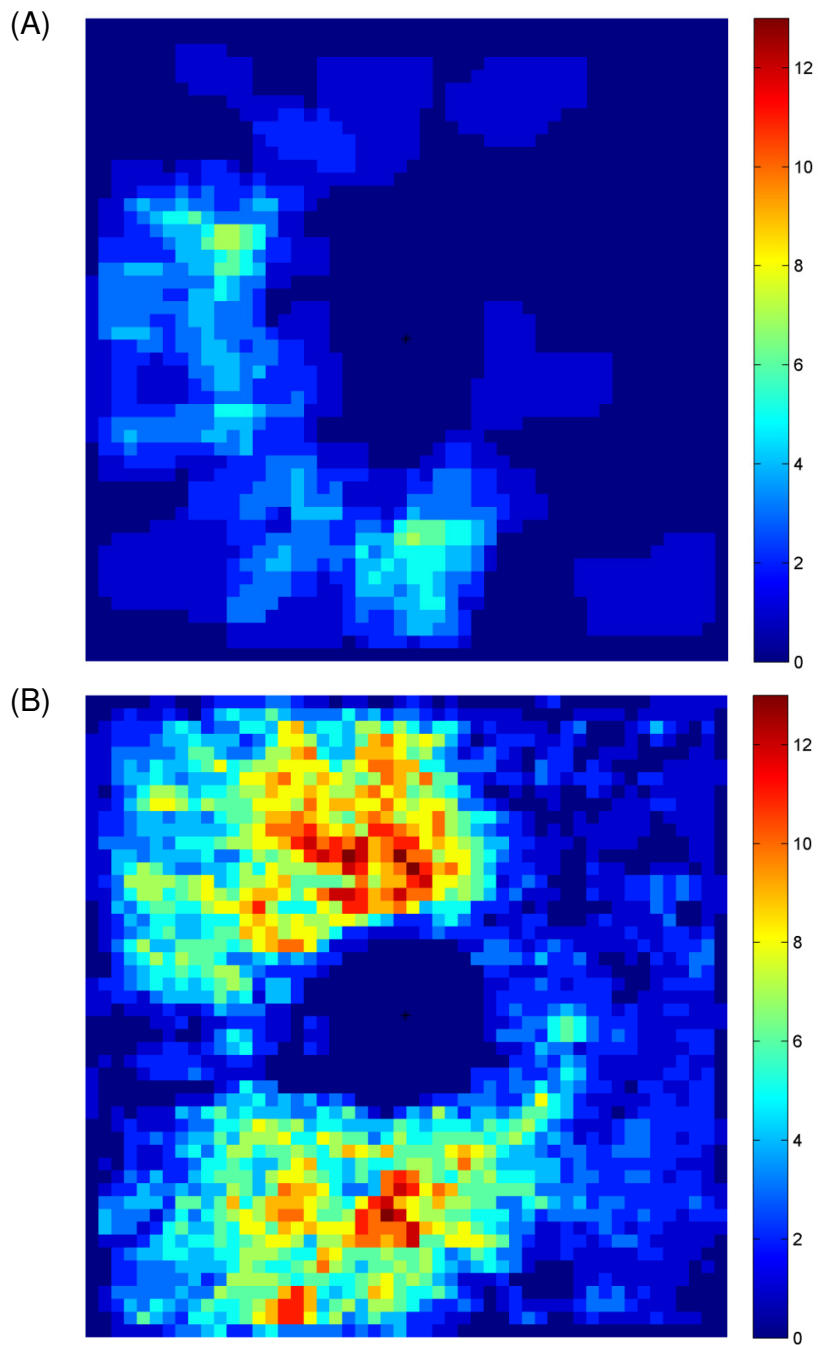
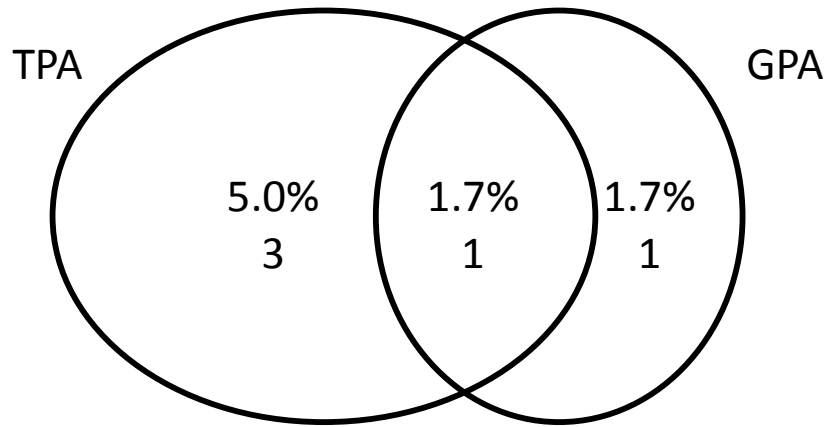


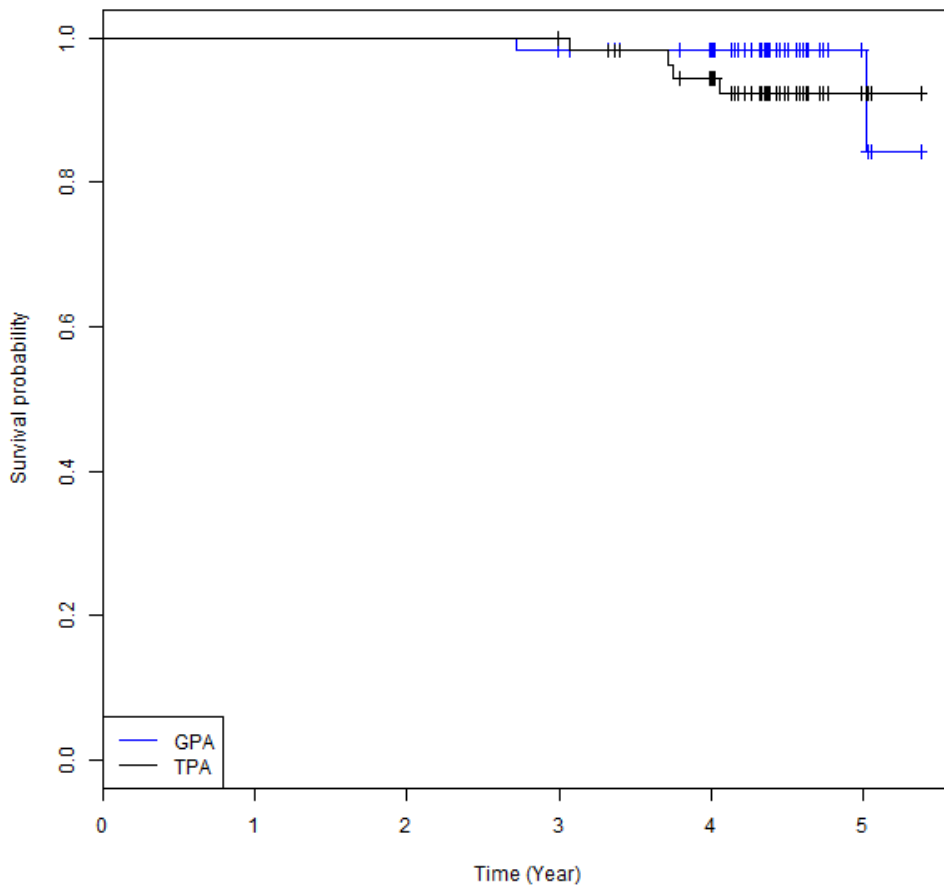
Figure 3.2.6 Agreement of the localized RNFL progression detected by the Trend-based Progression Analysis (TPA) and Guided Progression Analysis (GPA) in the normal group.



Kappa = 0.302 (95% CI: -0.358 - 0.963)

CI=confidence interval.

Figure 3.2.7 Survival probabilities of Trend-based Progression Analysis (TPA) and Guided Progression Analysis (GPA) estimated by the Kaplan–Meier estimators in the normal group.



3.3 Impact of Retinal Nerve Fiber Layer Measurement on Subsequent Change in Visual Function

3.3.1 Abstract

Objectives: To evaluate if prior retinal nerve fiber layer (RNFL) and visual field measurements would affect their subsequent changes during the course of glaucoma progression.

Methods: 84 eyes of 84 glaucoma patients [44 eyes with suspected/early glaucoma (baseline MD \geq -6 dB) and 40 eyes with moderate/advanced glaucoma (baseline MD $<$ -6 dB)] were followed every 4 months for spectral-domain OCT RNFL and visual field measurements for at least 35 months. Random Coefficient Autoregressive Linear Mixed Modeling (RCALMM) was used to investigate the impact of prior average RNFL thickness / visual field MD on subsequent changes in average RNFL thickness and visual field MD (measured at 4 month intervals) in the suspected/early and moderate/advanced glaucoma groups. Statistical causality between the structural and functional measurements were evaluated by statistical testing on the corresponding coefficients.

Results: Among the 84 eyes, RNFL and visual field progression were detected in 27 eyes (32.1%) and 18 eyes (21.4%), respectively, with linear regression analysis. In suspected/early glaucoma, both the prior average RNFL thickness (coefficient: 0.046, 95% confidence interval:

0.017 - 0.075, $p=0.002$) and prior visual field MD (coefficient: -0.680, 95% confidence interval: -0.807 - -0.554, $p<0.001$) were significantly associated with the subsequent change in visual field MD. A greater average RNFL thickness and/or a worse visual field MD were associated with a smaller reduction in the subsequent visual field MD. In moderate/advanced glaucoma, prior visual field MD (coefficient: -0.662, 95% confidence interval: -0.792 - -0.532, $p<0.001$) but not the prior average RNFL thickness (coefficient: 0.020, 95% confidence interval: -0.019 - 0.060, $p<0.310$) was associated with subsequent change in visual field MD. A worse visual field MD was associated with a smaller reduction in the subsequent visual field MD.

Conclusions: Functional change is relatively small whereas structural change is more substantive in the early stages of glaucoma when the RNFL is thick. RNFL measurement is useful to predict subsequent change in visual function.

3.3.2 Background and Objectives

Glaucoma is an optic neuropathy characterized by the progressive optic disc and visual field changes. However, the precise relationship between structural and functional changes in glaucoma remains unclear (Girkin, 2004, Johnson et al., 2000, Harwerth et al., 2005). Specifically, it is largely unclear the association between progression in optic disc / RNFL and progression in function. Although, a number of mathematical models have been described to address the relationship between the structure and function in glaucoma (Johnson et al., 2000, Harwerth et al., 2005, Leung et al., 2005, Bowd et al., 2006, Harwerth & Quigley, 2006, Hood & Kardon, 2007), most studies investigating the structure and function relationship were based on cross-sectional data. As glaucoma is a chronic progressive disease, long-term longitudinal data instead of cross-sectional data may provide more insights into the structure function relationship in glaucoma progression.

In longitudinal studies, the agreement between structural and functional progression in glaucoma often is poor (Fayers et al., 2007, Alencar et al., 2010, Moon et al., 2012). A Bayesian hierarchical linear model combining the rates of structural and functional progression have been proposed to improve detection of glaucoma progression (Medeiros et al., 2011). The use of structural progression detection to predict functional loss has also been investigated through survival analyses (Chauhan et al., 2009, Medeiros et al., 2009). The longitudinal study

conducted by Chauhan et al. followed 81 patients with open-angle glaucoma (OAG) for a median of 11 years (Chauhan et al., 2009). They reported that the time to visual field progression was consistently shorter by 0.8 - 1.7 years in patients with prior optic disc changes detected by confocal scanning laser ophthalmoscopy in the first 3 years. Subsequent visual field progression was more likely to occur in patients with prior optic disc changes (Chauhan et al., 2009). The study conducted by Medeiros et al. investigated 407 glaucoma suspects followed for an average of 8 years (Medeiros et al., 2009). It found that the odds of visual field progression with prior optic disc progression in optic disc photographs was 25.8 times higher those without (Medeiros et al., 2009). In this study, a mathematical model, random coefficient autoregressive linear mixed model (Rahiala, 1999), was used to investigate the causal relationship between structural change (based on OCT average RNFL thickness) and functional change (based on SAP derived MD) in glaucoma.

3.3.3 Subjects and Methods

3.3.3.1 Subjects

Eighty four open-angle glaucoma patients consecutively followed from June 2007 to October 2012 at the University Eye Center, the Chinese University of Hong Kong were included in the analysis. All subjects underwent visual field examination using SAP (SITA Standard 24-2,

HFA II, Carl Zeiss Meditec), spectral-domain OCT RNFL imaging (Cirrus HD-OCT, Carl Zeiss Meditec) and full ophthalmic examination, including measurement of visual acuity, refraction, intraocular pressure and fundus examination. Subjects were selected according to the inclusion and exclusion criteria described in section 2.2. Eighty four subjects (72 glaucoma and 12 glaucoma suspect subjects, classified according to the criteria stated in section 2.5) were followed every 4 months for at least 35 months (range 35 - 64 months with median of 49 months). One eye from each subject was randomly selected in the analysis.

3.3.3.2 Autoregressive modeling

In general, autoregressive modeling specifies that the output variable depends linearly on its own previous values. In this study, Random Coefficient Autoregressive Linear Mixed Model (RCALMM; or simply Random Coefficient Autoregressive (RCA) Model) introduced by Rahiala (Rahiala, 1999) was used to determine if prior average RNFL thickness or prior visual field MD was associated with the subsequent change in average RNFL thickness and visual field MD. Since both visual field MD and average RNFL thickness are non-age-adjusted measurements, the use of visual field MD was believed to be more comparable to average RNFL thickness than the age-adjusted visual field index (VFI). The RCALMM is an extension of the linear mixed model (LMM) including the previous responses into the covariates of the LMM. The mathematical details of the RCALMM model have been described in section 1.6.3.3.

Change in average RNFL thickness and visual field MD (defined as the difference in average RNFL thickness and visual field MD between consecutive follow-up visits) were regressed by RCALMMs on the prior average RNFL thickness and prior visual field mean deviation with random effects accounted at the subject level:

$$\begin{aligned} \begin{bmatrix} \Delta RNFL_{i,j} \\ \Delta MD_{i,j} \end{bmatrix} &= \begin{bmatrix} \beta_{1,0} \\ \beta_{2,0} \end{bmatrix} + \begin{bmatrix} \beta_{1,1} \\ \beta_{2,1} \end{bmatrix} \times RNFL_{i-1,j} + \begin{bmatrix} \beta_{1,2} \\ \beta_{2,2} \end{bmatrix} \times MD_{i-1,j} \\ &+ \begin{bmatrix} u_{1,0,j} \\ u_{2,0,j} \end{bmatrix} + \begin{bmatrix} u_{1,1,j} \\ u_{2,1,j} \end{bmatrix} \times RNFL_{i-1,j} + \begin{bmatrix} u_{1,2,j} \\ u_{2,2,j} \end{bmatrix} \times MD_{i-1,j} + \begin{bmatrix} \varepsilon_{1,i,j} \\ \varepsilon_{2,i,j} \end{bmatrix} \end{aligned}$$

where $(\Delta RNFL_{i,j}, \Delta MD_{i,j})^T$ represents the change in average RNFL thickness and change in visual field MD at examination i for subject j , $(\beta_{1,0}, \beta_{2,0})^T$, $(\beta_{1,1}, \beta_{2,1})^T$ and $(\beta_{1,2}, \beta_{2,2})^T$ represents the fixed effect coefficients corresponding to the intercept, the prior average RNFL thickness and the prior visual field MD, respectively, $(u_{1,0,j}, u_{2,0,j})^T$, $(u_{1,1,j}, u_{2,1,j})^T$ and $(u_{1,2,j}, u_{2,2,j})^T$ represents the random effect coefficients corresponding to the intercept, the prior average RNFL thickness and the prior visual field MD at the subject level, respectively, and $(\varepsilon_{1,i,j}, \varepsilon_{2,i,j})^T$ represents the residual errors. $(u_{1,0,j}, u_{2,0,j})^T$, $(u_{1,1,j}, u_{2,1,j})^T$ and $(u_{1,2,j}, u_{2,2,j})^T$ were assumed to follow identically normal distribution with mean zero and independent across subjects, and $(\varepsilon_{1,i,j}, \varepsilon_{2,i,j})^T$ was assumed to follow independent and identically normal distribution with mean zero.

3.3.3.3 Statistics

Statistical analyses were performed with the statistical computing software R version 2.15.2 (R Foundation, Vienna, Austria). Comparisons of RNFL and visual field MD measurements between the baseline and the final visits were based on paired t-test. The agreement index, Cohen's kappa (Cohen, 1960), was used to evaluate the agreement between structural and functional progression detection. Model fittings were performed using the lme4 package in R (Bates et al., 2012). Goodness of fits of different models was compared by likelihood ratio test (LRT). Significance of the fixed effects was determined by Wald test. $p < 0.05$ were considered statistically significant.

3.3.4 Results

3.3.4.1 Demographics

Eight-four eyes of 84 subjects (72 glaucoma and 12 glaucoma suspect patients) were followed every 4 months for at least 35 months (range: 35–64 months, median=49 months). The baseline average RNFL thickness and visual field MD were $69.78 \pm 13.30 \mu\text{m}$ and $-9.05 \pm 9.06 \text{ dB}$, respectively, which were significantly different from those obtained at the latest follow-up examination ($66.84 \pm 14.17 \mu\text{m}$ and $-9.86 \pm 8.54 \text{ dB}$, respectively, $p \leq 0.019$). A total of 942 OCT and 942 visual field examinations were included. Each eye had an average of 11 serial

measurements (range: 5-16) for analysis. Table 3.3.1 shows the demographics of participants.

3.3.4.2 Agreement between Structural and Functional Progression in Glaucoma

By defining RNFL and visual field progression as having a significant negative slope obtained in linear regression analysis between the average RNFL thickness and the visual field MD and time, respectively, 27 eyes (32.1%) had RNFL progression and 18 eyes (21.4%) had visual field progression. The rate of change of average RNFL thickness varied between $-2.05 \mu\text{m}/\text{year}$ and $-0.43 \mu\text{m}/\text{year}$, and the rate of change of visual field MD was between $-2.12 \text{ dB}/\text{year}$ and $-0.33 \text{ dB}/\text{year}$. Figure 3.3.1 shows the agreement of RNFL and visual field progression.

3.3.4.3 Causal Relationship between Structure and Function in Glaucoma

In order to investigate the statistical causality between the prior RNFL / visual field measurements and the subsequent changes, change in average RNFL thickness and change in visual field MD (measured at 4 month intervals) were regressed by random coefficient autoregressive linear mixed models (RCALMMs) on prior average RNFL thickness and prior visual field MD with random effects accounted at the subject level. As different stages of glaucoma may exhibit different patterns of dependence, 44 eyes with suspected/early glaucoma (baseline MD ≥ -6

dB) and 40 eyes with moderate/advanced glaucoma (baseline MD <-6 dB) were regressed by RCALMM separately.

Table 3.3.2 showed the RCALMM regression on the change in visual field MD. In suspected/early glaucoma, both the prior average RNFL thickness (coefficient: 0.046, 95% confidence interval: 0.017 - 0.075, $p=0.002$) and the prior visual field MD (coefficient: -0.680, 95% confidence interval: -0.807 - -0.554, $p<0.001$) were significantly associated with the subsequent change in visual field MD. A greater average RNFL thickness and/or a worse visual field MD were associated with a smaller reduction in the subsequent visual field MD. In moderate/advanced glaucoma, subsequent change in visual field MD was significantly associated with the prior visual field MD (coefficient: -0.662, 95% confidence interval: -0.792 - -0.532, $p<0.001$) but not with the prior average RNFL thickness (coefficient: 0.020, 95% confidence interval: -0.019 - 0.060, $p<0.310$). A worse visual field MD was associated with a smaller reduction in the subsequent visual field MD.

Table 3.3.3 showed the RCALMM regression on the change in average RNFL thickness. Prior average RNFL thickness was significantly associated with the subsequent change in average RNFL thickness in both suspected/early (coefficient: -0.031, 95% confidence interval: -0.053 - -0.008, $p=0.007$) and moderate/advanced glaucoma (coefficient: -0.731, 95% confidence interval: -0.839 - -0.622, $p<0.001$). A greater average RNFL thickness was associated with a larger reduction in the

subsequent RNFL measurement. No significant associations were observed between the prior visual field MD and the subsequent change in average RNFL thickness ($p \geq 0.083$).

3.3.5 Discussion

3.3.5.1 Structure and function relationship

To our knowledge, this is the first study using prospective longitudinal OCT RNFL and visual field measurements to investigate the impact of prior measurement of structure/function on their subsequent changes. Using the random coefficient autoregressive linear mixed model (RCALMM), we showed that prior average RNFL thickness was positively associated with subsequent change in visual field MD in suspected/early glaucoma (coefficient: 0.046, $p=0.002$ in Table 3.3.2) and negatively associated with subsequent change in average RNFL thickness in both suspected/early (coefficient: -0.031, $p=0.007$ in Table 3.3.3) and moderate/advanced glaucoma (coefficient: -0.731, $p<0.001$ in Table 3.3.3). In other words, in suspected/early glaucoma when the RNFL is thick, the subsequent change in function would be relatively small and the subsequent change in the RNFL would be relatively substantive. By contrast, when the RNFL is thin as in moderate/advanced glaucoma, prior RNFL measurement would be relatively less influential to subsequent change in function. These findings are in agreement with the previous studies suggesting that a

considerable degree of retinal ganglion cell loss would occur before detectable change in visual function (Quigley & Addicks, 1982, Quigley et al., 1982, Harwerth et al., 1999, Kerrigan-Baumrind et al., 2000, Harwerth & Quigley, 2006). For OCT RNFL measurement, floor effect may set in when glaucoma advances, rendering further detection of RNFL thinning difficult (Hood et al., 2007, Leite et al., 2012).

On the other hand, prior visual field MD was negatively associated with subsequent change in visual field MD in both suspected/early (coefficient: -0.680, $p < 0.001$ in Table 3.3.2) and moderate/advanced glaucoma (coefficient: -0.662, $p < 0.001$ in Table 3.3.2), but not associated with subsequent change in average RNFL thickness ($p \geq 0.083$ in Table 3.3.3). In the late stages of glaucoma when the visual field MD is significantly negative, further change in visual field MD would be relatively small. Glaucoma progression likely begins with progressive RNFL thinning with minimal change in visual field. As the disease advances with extensive loss of RNFL and visual function, detection of change in structure and function would both become difficult.

3.3.5.2 Importance of the prior measurements

In the investigation of glaucoma progression, many studies have suggested that linear regression can provide an adequate fit between visual field and time (Mikelberg et al., 1986, McNaught et al., 1995, Bengtsson et al., 2009). Linear regression is simple and provides a

convenient approach to estimate the rate of change for any parameter of interest. However, as described in section 1.6.3.3, the link function in linear modeling is deterministic. In this study, we used an autoregressive model to address the casual relationship between prior and subsequent measurements. In the RCALMM, average RNFL thickness and visual field MD were regressed on prior average RNFL thickness and visual field MD, follow-up duration, age and spherical error. The model fitting was significantly better than fitting with LMMs without including the prior RNFL and visual field MD measurements (Table 3.3.4 and Table 3.3.5). Based on the likelihood ratio test derived by Self & Liang (Self & Liang, 1987), the likelihood ratio statistics comparing the RCALMMs and the corresponding LMMs followed a $\left(\frac{1}{4} : \frac{1}{2} : \frac{1}{4}\right)$ mixture of chi-square distributions with degree of freedom (7,8,9). The goodness of fit measures of both RCALMMs were significantly better ($p < 0.001$) than the two corresponding LMMs. Therefore, the prior average RNFL thickness and the prior visual field MD would be important factors affecting the subsequent measurements after adjusting for the deterministic rate of progression (represented by the coefficients of follow-up duration).

3.3.5.3 Limitation - Order specification and spurious dependency in autoregressive model

In this study, only first order autoregressive teams, the prior average RNFL thickness and the prior visual field MD measured 4 months before

the subsequent measurements, were considered. It is possible that higher order autoregressive terms, measurements obtained in 8,12,16 ... months before the subsequent measurements may also influence the subsequent measurements even when the first order prior measurements are given. A spurious finding incorrectly suggesting causality may occur.

Figure 3.3.2 illustrated an example of spurious causality when an autoregressive model of order 2 is wrongly specified as autoregressive model of order 1. Consider two measurements denoted as Y_t and X_t , and suppose that the value of Y_t depends on the prior values of Y_{t-1} and Y_{t-2} and the value of X_t depends on the prior value of Y_{t-1} . Without modeling the 2nd order term Y_{t-2} for the prediction of Y_t , X_{t-1} , which carries the information of Y_{t-2} , will become informative for the prediction of Y_t . Y_t will be wrongly modeled as depending on Y_{t-1} and X_{t-1} even X_{t-1} does not affect the upcoming value of Y_t .

3.3.5.4 Conclusions

In summary, prior average RNFL thickness and prior visual field MD were associated with subsequent loss in visual field MD. By contrast, only prior average RNFL thickness, but not visual field MD, was associated with subsequent reduction in average RNFL thickness. This study affords evidence in favor of the view that functional change is relatively small whereas structural change is more substantive in the

early stages of glaucoma when the RNFL is thick. Our results suggest that OCT RNFL measurements obtained with the spectral-domain OCT would be useful to predict subsequent visual field progression in glaucoma and may thus be qualified as an outcome measure in clinical trials investigating glaucoma progression.

Table 3.3.1 Demographics, Retinal Nerve Fiber Layer (RNFL), and visual field measurements of 84 eyes of 84 glaucoma and glaucoma suspect subjects who were followed up every 4 months for at least 35 months.

	Mean ± SD
Age	51.7 ± 14.1
Spherical error (D)	-2.54 ± 4.09
Number of examinations	11.2 ± 2.7
Signal strength	7.7 ± 0.8
<u>Baseline examination</u>	
Average RNFL thickness (µm)	69.78 ± 13.30
Visual field mean deviation (dB)	-9.05 ± 9.06
Visual field index (%)	75.9 ± 27.1
<u>Final examination</u>	
Average RNFL thickness (µm)	66.84 ± 14.17
Visual field mean deviation (dB)	-9.86 ± 8.54
Visual field index (%)	74.6 ± 26.0
<u>Duration of follow-up (month)</u>	
Median	49
Minimum	35
Maximum	64

D=dioptr; dB=decibels.

Table 3.3.2 Coefficient estimates of Random Coefficient Autoregressive Linear Mixed Model (RCALMM) for the change in visual field mean deviation (MD) on the prior average RNFL thickness and the prior visual field MD.

Change in Visual Field Mean Deviation						
Suspected/Early Glaucoma						
Overall Level	Fixed Effects				Random Effects	
	Coefficient	SD	95% CI	p	Subject Level	SD
Intercept	-5.981	1.211	(-8.356, -3.607)	<0.001	Intercept	2.433
Prior RNFL thickness	0.046	0.015	(0.017, 0.075)	0.002	Prior RNFL thickness	0.010
Prior visual field MD	-0.680	0.064	(-0.807, -0.554)	<0.001	Prior visual field MD	0.269
					Residual Error	1.161
Moderate/Advanced Glaucoma						
Overall Level	Fixed Effects				Random Effects	
	Coefficient	SD	95% CI	p	Subject Level	SD
Intercept	-11.672	1.676	(-14.957, -8.387)	<0.001	Intercept	5.211
Prior RNFL thickness	0.020	0.020	(-0.019, 0.060)	0.310	Prior RNFL thickness	0.037
Prior visual field MD	-0.662	0.066	(-0.792, -0.532)	<0.001	Prior visual field MD	0.261
					Residual Error	1.249

Eyes were classified into suspected/early glaucoma if baseline MD \geq -6 dB and moderate/advanced glaucoma if baseline MD <-6 dB. Changes in visual field MD were measure at 4 month intervals. Prior measurements were the obtained 4 \pm 1 months prior to the changes in visual field MD. P values are calculated based on Wald test.

Table 3.3.3 Coefficient estimates of Random Coefficient Autoregressive Linear Mixed Model (RCALMM) for the change in average RNFL thickness on the prior average RNFL thickness and the prior visual field MD.

Change in Average RNFL Thickness						
Suspected/Early Glaucoma						
Overall Level	Fixed Effects				Random Effects	
	Coefficient	SD	95% CI	p	Subject Level	SD
Intercept	1.985	0.954	(0.116, 3.854)	0.037	Intercept	0.000
Prior RNFL thickness	-0.031	0.011	(-0.053, -0.008)	0.007	Prior RNFL thickness	0.000
Prior visual field MD	0.009	0.057	(-0.102, 0.120)	0.877	Prior visual field MD	0.000
					Residual Error	2.687
Moderate/Advanced Glaucoma						
Overall Level	Fixed Effects				Random Effects	
	Coefficient	SD	95% CI	p	Subject Level	SD
Intercept	46.210	3.825	(38.713, 53.706)	<0.001	Intercept	2.384
Prior RNFL thickness	-0.731	0.056	(-0.839, -0.622)	<0.001	Prior RNFL thickness	0.129
Prior visual field MD	0.205	0.118	(-0.026, 0.437)	0.083	Prior visual field MD	0.071
					Residual Error	4.376

Eyes were classified into suspected/early glaucoma if baseline MD \geq -6 dB and moderate/advanced glaucoma if baseline MD <-6 dB. Changes in average RNFL thickness were measure at 4 month intervals. Prior measurements were the obtained 4 \pm 1 months prior to the changes in visual field MD. P values are calculated based on Wald test.

Table 3.3.4 Coefficient estimates of Random Coefficient Autoregressive Linear Mixed Models (RCALMMs) for the average RNFL thickness and visual field MD on the prior average RNFL thickness, the prior visual field MD, follow-up duration, age and spherical error.

RCALMM for Average RNFL Thickness *						
Overall Level	Fixed Effects				Random Effects	
	Coefficient	SD	95% CI	p	Subject Level	SD
Intercept	67.583	5.984	(55.855, 79.311)	<0.001	Intercept	6.719
Follow-up duration	-0.511	0.278	(-1.057, 0.035)	0.066	Follow-up duration	2.266
Prior RNFL thickness	0.154	0.033	(0.089, 0.220)	<0.001	Prior RNFL thickness	0.105
Prior visual field MD	0.178	0.090	(0.001, 0.355)	0.049	Prior visual field MD	0.538
Age	-0.130	0.091	(-0.308, 0.048)	0.152		
Spherical Error	0.707	0.324	(0.072, 1.342)	0.029	Residual Error	2.755
RCALMM for Visual Field Mean Deviation (MD) *						
Overall Level	Fixed Effects				Random Effects	
	Coefficient	SD	95% CI	p	Subject Level	SD
Intercept	-10.171	2.453	(-14.978, -5.364)	<0.001	Intercept	7.374
Follow-up duration	-0.057	0.050	(-0.154, 0.040)	0.250	Follow-up duration	0.066
Prior RNFL thickness	0.064	0.016	(0.032, 0.096)	<0.001	Prior RNFL thickness	0.051
Prior visual field MD	0.356	0.046	(0.266, 0.447)	<0.001	Prior visual field MD	0.295
Age	0.013	0.033	(-0.052, 0.077)	0.702		
Spherical Error	0.032	0.109	(-0.182, 0.246)	0.768	Residual Error	1.221

Prior measurements were the obtained 4±1 months prior to the responses. P values are calculated based on Wald test.

*Both models were compare with the corresponding LMMs with all the covariates except the prior measurements. Based on likelihood ratio test (LRT), the goodness of fit of both RCALMMs were significantly better (p<0.001) than those of the corresponding LMMs shown in Table 3.3.5.

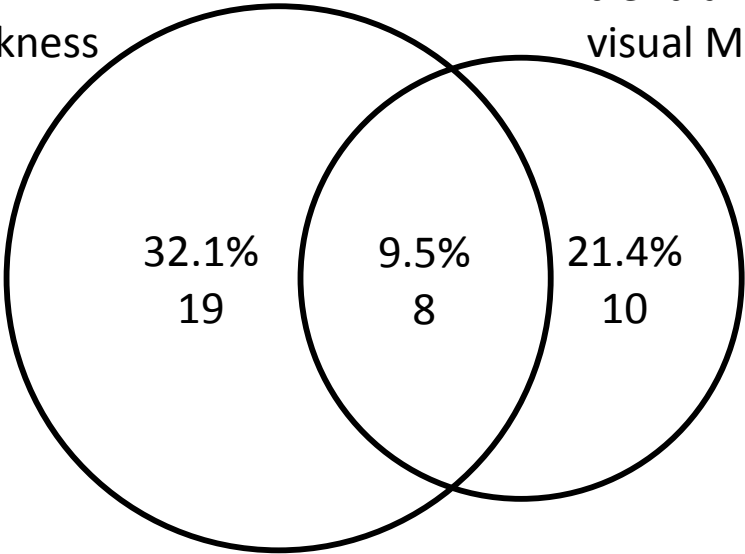
Table 3.3.5 Coefficient estimates of Linear Mixed Models (LMMs) for the average RNFL thickness and visual field MD on the follow-up duration, age and spherical error.

LMM for Average RNFL Thickness						
Overall Level	Fixed Effects				Random Effects	
	Coefficient	SD	95% CI	p	Subject Level	SD
Intercept	81.955	6.820	(68.588, 95.321)	<0.001	Intercept	12.590
Follow-up duration	-0.535	0.208	(-0.943, -0.127)	0.010	Follow-up duration	1.344
Age	-0.188	0.117	(-0.418, 0.041)	0.108		
Spherical Error	1.046	0.405	(0.252, 1.840)	0.010	Residual Error	3.003
LMM for Visual Field Mean Deviation (MD)						
Overall Level	Fixed Effects				Random Effects	
	Coefficient	SD	95% CI	p	Subject Level	SD
Intercept	-9.265	4.439	(-17.964, -0.565)	0.037	Intercept	8.234
Follow-up duration	-0.185	0.095	(-0.371, 0.002)	0.052	Follow-up duration	0.425
Age	0.009	0.076	(-0.140, 0.159)	0.901		
Spherical Error	0.276	0.264	(-0.242, 0.793)	0.297	Residual Error	1.127

Figure 3.3.1 Agreement of RNFL thickness and visual field progression in the 84 eyes of 84 subjects

Progression detection by trend analysis on average RNFL thickness

Progression detection by trend analysis on visual MD

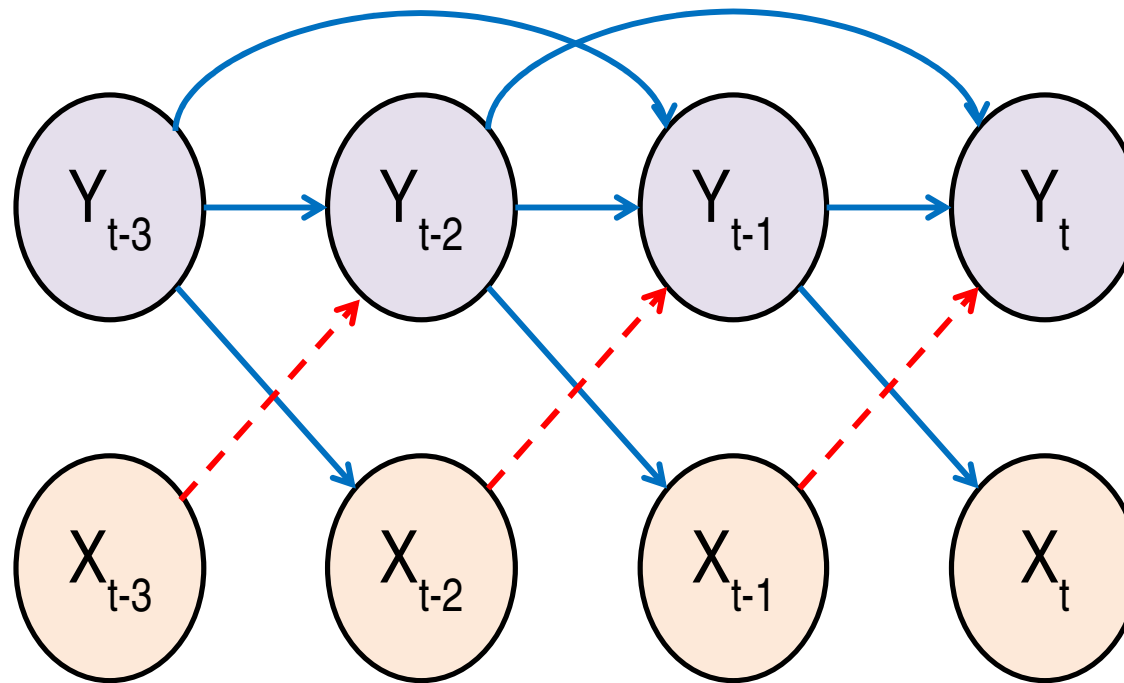


kappa = 0.132 (CI: -0.123 – 0.388)

CI=confidence interval.

Figure 3.3.2 An example of spurious causality when an autoregressive model of order 2 is wrongly specified as autoregressive model of order 1. Suppose the value of Y_t depends on the prior values of Y_{t-1} and Y_{t-2} and the value of X_t depends on the prior value of Y_{t-1} . The blue arrows in solid lines represent the true dependencies between the two measurements.

Without modeling the 2nd order term Y_{t-2} for the prediction of Y_t , X_{t-1} , which carries the information of Y_{t-2} , will become informative for the prediction of Y_t . Y_t will be wrongly modeled as depending on Y_{t-1} and X_{t-1} even X_{t-1} does not affect the upcoming value of Y_t . The red arrows in dashed lines represent the spurious dependencies observed when the 2nd order terms are not considered.



CHAPTER 4 GENERAL CONCLUSIONS

4.1 Conclusions

Detecting progressive retinal nerve fiber layer thinning is relevant and important in monitoring glaucoma progression. This study was designed to address different approaches and statistical models to evaluate progressive RNFL reduction and its impact on subsequent change in visual function. In the computer simulation study, we showed that trend-based analysis generally attained high sensitivity earlier than event-based analysis to detect significant reduction of average RNFL thickness measured by the spectral-domain OCT at a similar level of specificity (Figure 3.1.3 - Figure 3.1.5). However, for subjects with a short follow-up duration and a large test-retest variability, event analysis using a group test-retest variability may have a higher sensitivity to detect change but with a trade-off of a lower specificity compared with trend analysis. These findings were confirmed with longitudinal data collected from glaucoma patients. Following 107 glaucoma patients and glaucoma suspects for a median of 38 months, the detection rate of RNFL progression was 42%, 35%, and 3% for TA, whereas it was 11% to 40%, 12% to 28%, and 3% to 23% for EA in eyes with small, average, and large test-retest variabilities, respectively. For progression detection of the average RNFL thickness using trend analysis, three observations per year was found to be an efficient monitoring schedule (Figure 3.1.11)

although monitoring frequency should be scheduled with reference to the disease severity and the life expectancy.

Having found that trend analysis had a higher sensitivity to detect average RNFL thickness loss, we then extended its application in the RNFL thickness map and introduced the Trend-based Progression Analysis (TPA). TPA was able to detect progressive RNFL thinning earlier than or at the same time as GPA in 75% of 68 eyes in 48 glaucoma patients and the survival probability of TPA was significantly lower than that of GPA ($p=0.012$). The false discovery rates in the 38 eyes detected with progression by TPA were all $\leq 5\%$. With the reporting of the false discovery rate and the rate of change in the RNFL thickness change map, TPA can provide a more informative approach to detect RNFL progression than GPA.

We then investigated the impact of RNFL progression on subsequent change in visual function in glaucoma using autoregressive modeling. We showed that prior average RNFL thickness and prior visual field MD were significantly associated with the subsequent change in visual field MD in early glaucoma. A greater average RNFL thickness was associated with a smaller subsequent change in function but a greater subsequent loss in RNFL thickness. By contrast, in the late stages of glaucoma when the RNFL is thin and visual field is extensively damaged, detecting subsequent reduction in RNFL thickness and visual function would be difficult. RNFL thickness can be an informative biomarker to

predict subsequent change in visual field particularly in the early stages of glaucoma.

4.2 Future Works

Trend analysis was found to be a more sensitive approach to detect change in glaucoma compared with event analysis. Future work is to refine the application of TPA using the shape, smoothness and curvature of the RNFL profiles to improve the detection of glaucoma progression. Although TPA detected more eyes with progression than GPA, it is possible that the detected change may represent age-related change. Analyzing progression with consideration of age-related loss of the RNFL would be important to identify glaucomatous RNFL progression.

The statistical model, RCALMM of order 1, was used to understand the structure and function relationship in glaucoma. The results suggested that prior average RNFL thickness and prior visual field MD were associated with the subsequent changes in visual field MD. However, without considering the higher order autoregressive terms, the statistical causality can be spurious. Collecting longitudinal data with a longer follow-up duration would be important to fully address the issue.

BIBLIOGRAPHY

- Advanced Glaucoma Intervention Study. 2. Visual field test scoring and reliability. (1994). *Ophthalmology*, 101(8), 1445–1455.
- Agarwal, R., Gupta, S., Agarwal, P., Saxena, R., & Agrawal, S. (2009). Current concepts in the pathophysiology of glaucoma. *Indian Journal of Ophthalmology*, 57(4), 257. doi:10.4103/0301-4738.53049
- Airaksinen, P. J., & Heijl, A. (1983). Visual field and retinal nerve fibre layer in early glaucoma after optic disc haemorrhage. *Acta ophthalmologica*, 61(2), 186–194.
- Airaksinen, P. J., Mustonen, E., & Alanko, H. I. (1981a). Optic disc haemorrhages precede retinal nerve fibre layer defects in ocular hypertension. *Acta ophthalmologica*, 59(5), 627–641.
- Airaksinen, P. J., Mustonen, E., & Alanko, H. I. (1981b). Optic disc hemorrhages. Analysis of stereophotographs and clinical data of 112 patients. *Archives of ophthalmology*, 99(10), 1795–1801.
- Alencar, L. M., Zangwill, L. M., Weinreb, R. N., Bowd, C., Sample, P. A., Girkin, C. A., ... Medeiros, F. A. (2010). A comparison of rates of change in neuroretinal rim area and retinal nerve fiber layer thickness in progressive glaucoma. *Investigative ophthalmology & visual science*, 51(7), 3531–3539. doi:10.1167/iovs.09-4350
- Alencar, L. M., Zangwill, L. M., Weinreb, R. N., Bowd, C., Vizzeri, G., Sample, P. A., ... Medeiros, F. A. (2010). Agreement for detecting glaucoma progression with the GDx guided progression analysis, automated perimetry, and optic disc

photography. *Ophthalmology*, 117(3), 462–470.

doi:10.1016/j.ophtha.2009.08.012

Antón, A., Pazos, M., Martín, B., Navero, J. M., Ayala, M. E., Castany, M., ... Bardavío, J.

(2013). Glaucoma progression detection: agreement, sensitivity, and specificity of expert visual field evaluation, event analysis, and trend analysis.

European journal of ophthalmology, 23(2), 187–195.

doi:10.5301/ejo.5000193

Artes, P. H., O'Leary, N., Hutchison, D. M., Heckler, L., Sharpe, G. P., Nicolela, M. T., &

Chauhan, B. C. (2011). Properties of the statpac visual field index.

Investigative ophthalmology & visual science, 52(7), 4030–4038.

doi:10.1167/iovs.10-6905

Azuara-Blanco, A., Katz, L. J., Spaeth, G. L., Vernon, S. A., Spencer, F., & Lanzl, I. M.

(2003). Clinical agreement among glaucoma experts in the detection of glaucomatous changes of the optic disk using simultaneous stereoscopic photographs. *American journal of ophthalmology*, 136(5), 949–950.

Bates, D., Maechler, M., & Bolker, B. (2012). lme4: Linear mixed-effects models using

S4 classes. Retrieved from <http://CRAN.R-project.org/package=lme4>

Bengtsson, B. (1976). The variation and covariation of cup and disc diameters. *Acta*

ophthalmologica, 54(6), 804–818.

Bengtsson, Boel, & Heijl, A. (2008). A visual field index for calculation of glaucoma

rate of progression. *American journal of ophthalmology*, 145(2), 343–353.

doi:10.1016/j.ajo.2007.09.038

- Bengtsson, Boel, Patella, V. M., & Heijl, A. (2009). Prediction of glaucomatous visual field loss by extrapolation of linear trends. *Archives of ophthalmology*, 127(12), 1610–1615. doi:10.1001/archophthalmol.2009.297
- Benjamini, Y., & Hochberg, Y. (1995). Controlling the false discovery rate: a practical and powerful approach to multiple testing. *Journal of the Royal Statistical Society. Series B (Statistical Methodology)*, 57, 289–300.
- Benjamini, Y., & Hochberg, Y. (1997). Multiple Hypotheses Testing With Weights. *Scandinavian Journal of Statistics*, 24, 407–418.
- Benjamini, Y., Krieger, A. M., & Yekutieli, D. (2006). Adaptive linear step-up procedures that control the false discovery rate. *Biometrika*, 93, 491–507.
- Benjamini, Y., & Yekutieli, D. (2001). The control of the false discovery rate in multiple testing under dependency. *Annals of Statistics*, 29, 1165–1188.
- Bill, A., & Sperber, G. O. (1990). Control of retinal and choroidal blood flow. *Eye (London, England)*, 4 (Pt 2), 319–325. doi:10.1038/eye.1990.43
- Bland, J. M., & Altman, D. G. (1996). Measurement error. *BMJ (Clinical research ed.)*, 312(7047), 1654.
- Bonomi, L., Marchini, G., Marraffa, M., Bernardi, P., Morbio, R., & Varotto, A. (2000). Vascular risk factors for primary open angle glaucoma: the Egna-Neumarkt Study. *Ophthalmology*, 107(7), 1287–1293.
- Bowd, C., Zangwill, L. M., Medeiros, F. A., Tavares, I. M., Hoffmann, E. M., Bourne, R. R., ... Weinreb, R. N. (2006). Structure-function relationships using confocal scanning laser ophthalmoscopy, optical coherence tomography, and scanning laser polarimetry. *Investigative ophthalmology & visual science*, 47(7), 2889–2895. doi:10.1167/iops.05-1489

- Broman, A. T., Quigley, H. A., West, S. K., Katz, J., Munoz, B., Bandeen-Roche, K., ... Foster, P. J. (2008). Estimating the rate of progressive visual field damage in those with open-angle glaucoma, from cross-sectional data. *Investigative ophthalmology & visual science*, *49*(1), 66–76. doi:10.1167/iavs.07-0866
- Budenz, D. L., Chang, R. T., Huang, X., Knighton, R. W., & Tielsch, J. M. (2005). Reproducibility of retinal nerve fiber thickness measurements using the stratus OCT in normal and glaucomatous eyes. *Investigative ophthalmology & visual science*, *46*(7), 2440–2443. doi:10.1167/iavs.04-1174
- Budenz, D. L., Fredette, M.-J., Feuer, W. J., & Anderson, D. R. (2008). Reproducibility of peripapillary retinal nerve fiber thickness measurements with stratus OCT in glaucomatous eyes. *Ophthalmology*, *115*(4), 661–666.e4. doi:10.1016/j.ophtha.2007.05.035
- Budenz, D. L., Michael, A., Chang, R. T., McSoley, J., & Katz, J. (2005). Sensitivity and specificity of the StratusOCT for perimetric glaucoma. *Ophthalmology*, *112*(1), 3–9. doi:10.1016/j.ophtha.2004.06.039
- Caprioli, J., & Miller, J. M. (1987). Optic disc rim area is related to disc size in normal subjects. *Archives of ophthalmology*, *105*(12), 1683–1685.
- Caprioli, Joseph, Mock, D., Bitrian, E., Affi, A. A., Yu, F., Nouri-Mahdavi, K., & Coleman, A. L. (2011). A method to measure and predict rates of regional visual field decay in glaucoma. *Investigative ophthalmology & visual science*, *52*(7), 4765–4773. doi:10.1167/iavs.10-6414
- Casas-Llera, P., Rebolleda, G., Muñoz-Negrete, F. J., Arnalich-Montiel, F., Pérez-López, M., & Fernández-Buenaga, R. (2009). Visual field index rate and event-based glaucoma progression analysis: comparison in a glaucoma population. *The*

British journal of ophthalmology, 93(12), 1576–1579.

doi:10.1136/bjo.2009.158097

Cello, K. E., Nelson-Quigg, J. M., & Johnson, C. A. (2000). Frequency doubling technology perimetry for detection of glaucomatous visual field loss.

American journal of ophthalmology, 129(3), 314–322.

Chauhan, B C, Blanchard, J. W., Hamilton, D. C., & LeBlanc, R. P. (2000). Technique for detecting serial topographic changes in the optic disc and peripapillary retina using scanning laser tomography. *Investigative ophthalmology & visual science*, 41(3), 775–782.

Chauhan, B C, LeBlanc, R. P., McCormick, T. A., & Rogers, J. B. (1994). Test-retest variability of topographic measurements with confocal scanning laser tomography in patients with glaucoma and control subjects. *American journal of ophthalmology*, 118(1), 9–15.

Chauhan, B C, McCormick, T. A., Nicolela, M. T., & LeBlanc, R. P. (2001). Optic disc and visual field changes in a prospective longitudinal study of patients with glaucoma: comparison of scanning laser tomography with conventional perimetry and optic disc photography. *Archives of ophthalmology*, 119(10), 1492–1499.

Chauhan, Balwantray C, Hutchison, D. M., Artes, P. H., Caprioli, J., Jonas, J. B., LeBlanc, R. P., & Nicolela, M. T. (2009). Optic disc progression in glaucoma: comparison of confocal scanning laser tomography to optic disc photographs in a prospective study. *Investigative ophthalmology & visual science*, 50(4), 1682–1691. doi:10.1167/iovs.08-2457

- Chauhan, Balwantray C, Pan, J., Archibald, M. L., LeVatte, T. L., Kelly, M. E. M., & Tremblay, F. (2002). Effect of intraocular pressure on optic disc topography, electroretinography, and axonal loss in a chronic pressure-induced rat model of optic nerve damage. *Investigative ophthalmology & visual science*, *43*(9), 2969–2976.
- Chauhan, Balwantray C., Nicolela, M. T., & Artes, P. H. (2009). Incidence and Rates of Visual Field Progression after Longitudinally Measured Optic Disc Change in Glaucoma. *Ophthalmology*, *116*(11), 2110–2118.
doi:10.1016/j.ophtha.2009.04.031
- Chung, H. S., Harris, A., Kagemann, L., & Martin, B. (1999). Peripapillary retinal blood flow in normal tension glaucoma. *The British journal of ophthalmology*, *83*(4), 466–469.
- Cohen, J. (1960). A Coefficient of Agreement for Nominal Scales. *Educational and Psychological Measurement*, *20*(1), 37–46.
doi:10.1177/001316446002000104
- Coleman, A. L., Sommer, A., Enger, C., Knopf, H. L., Stamper, R. L., & Minckler, D. S. (1996). Interobserver and intraobserver variability in the detection of glaucomatous progression of the optic disc. *Journal of glaucoma*, *5*(6), 384–389.
- Coops, A., Henson, D. B., Kwartz, A. J., & Artes, P. H. (2006). Automated analysis of heidelberg retina tomograph optic disc images by glaucoma probability score. *Investigative ophthalmology & visual science*, *47*(12), 5348–5355.
doi:10.1167/iovs.06-0579

- Crabb, D. P., & Garway-Heath, D. F. (2012). Intervals between visual field tests when monitoring the glaucomatous patient: wait-and-see approach. *Investigative ophthalmology & visual science*, *53*(6), 2770–2776. doi:10.1167/iops.12-9476
- Dada, T., Gadia, R., Aggarwal, A., Dave, V., Gupta, V., & Sihota, R. (2009). Retinal nerve fiber layer thickness measurement by scanning laser polarimetry (GDxVCC) at conventional and modified diameter scans in normals, glaucoma suspects, and early glaucoma patients. *Journal of glaucoma*, *18*(6), 448–452. doi:10.1097/IJG.0b013e3181895e2b
- Fayers, T., Strouthidis, N. G., & Garway-Heath, D. F. (2007). Monitoring glaucomatous progression using a novel Heidelberg Retina Tomograph event analysis. *Ophthalmology*, *114*(11), 1973–1980. doi:10.1016/j.ophtha.2007.01.035
- Fechtner, R. D., & Weinreb, R. N. (1994). Mechanisms of optic nerve damage in primary open angle glaucoma. *Survey of ophthalmology*, *39*(1), 23–42.
- Fercher, A. F., Hitzenberger, C. K., Kamp, G., & El-Zaiat, S. Y. (1995). Measurement of intraocular distances by backscattering spectral interferometry. *Optics Communications*, *117*(1-2), 43–48. doi:10.1016/0030-4018(95)00119-S
- Fitzgibbon, T., & Taylor, S. F. (1996). Retinotomy of the human retinal nerve fibre layer and optic nerve head. *The Journal of comparative neurology*, *375*(2), 238–251. doi:10.1002/(SICI)1096-9861(19961111)375:2<238::AID-CNE5>3.0.CO;2-3
- Flammer, J., Orgül, S., Costa, V. P., Orzalesi, N., Krieglstein, G. K., Serra, L. M., ... Stefánsson, E. (2002). The impact of ocular blood flow in glaucoma. *Progress in retinal and eye research*, *21*(4), 359–393.

- Fried, R. (2001). Autoregressive Linear Mixed Models for Investigating Humus Disintegration. *Biometrical Journal*, 43(6), 747. doi:10.1002/1521-4036(200110)43:6<747::AID-BIMJ747>3.0.CO;2-S
- Funatogawa, I., & Funatogawa, T. (2012). An autoregressive linear mixed effects model for the analysis of unequally spaced longitudinal data with dose-modification. *Statistics in medicine*, 31(6), 589–599. doi:10.1002/sim.4456
- Funatogawa, I., Funatogawa, T., & Ohashi, Y. (2007). An autoregressive linear mixed effects model for the analysis of longitudinal data which show profiles approaching asymptotes. *Statistics in medicine*, 26(9), 2113–2130. doi:10.1002/sim.2670
- Funatogawa, I., Funatogawa, T., & Ohashi, Y. (2008). A bivariate autoregressive linear mixed effects model for the analysis of longitudinal data. *Statistics in medicine*, 27(30), 6367–6378. doi:10.1002/sim.3456
- Funatogawa, T., Funatogawa, I., & Takeuchi, M. (2008). An autoregressive linear mixed effects model for the analysis of longitudinal data which include dropouts and show profiles approaching asymptotes. *Statistics in medicine*, 27(30), 6351–6366. doi:10.1002/sim.3417
- Garvin, M. K., Abramoff, M. D., Lee, K., Niemeijer, M., Sonka, M., & Kwon, Y. H. (2012). 2-D Pattern of Nerve Fiber Bundles in Glaucoma Emerging from Spectral-Domain Optical Coherence Tomography. *Investigative Ophthalmology & Visual Science*, 53(1), 483–489. doi:10.1167/iops.11-8349
- Garway-Heath, D. F., Poinoosawmy, D., Fitzke, F. W., & Hitchings, R. A. (2000). Mapping the visual field to the optic disc in normal tension glaucoma eyes. *Ophthalmology*, 107(10), 1809–1815.

- Garway-Heath, D. F., Poinosawmy, D., Wollstein, G., Viswanathan, A., Kamal, D., Fontana, L., & Hitchings, R. A. (1999). Inter- and intraobserver variation in the analysis of optic disc images: comparison of the Heidelberg retina tomograph and computer assisted planimetry. *The British journal of ophthalmology*, 83(6), 664–669.
- Girkin, C. A. (2004). Relationship between structure of optic nerve/nerve fiber layer and functional measurements in glaucoma. *Current opinion in ophthalmology*, 15(2), 96–101.
- Gloster, J. (1981). Incidence of optic disc haemorrhages in chronic simple glaucoma and ocular hypertension. *The British journal of ophthalmology*, 65(7), 452–456.
- González-García, A. O., Vizzeri, G., Bowd, C., Medeiros, F. A., Zangwill, L. M., & Weinreb, R. N. (2009). Reproducibility of RTVue retinal nerve fiber layer thickness and optic disc measurements and agreement with Stratus optical coherence tomography measurements. *American journal of ophthalmology*, 147(6), 1067–1074, 1074.e1. doi:10.1016/j.ajo.2008.12.032
- Granger, C. W. J. (1969). Investigating Causal Relations by Econometric Models and Cross-spectral Methods. *Econometrica*, 37(3), 424. doi:10.2307/1912791
- Greenfield, D. S., Knighton, R. W., & Huang, X. R. (2000). Effect of corneal polarization axis on assessment of retinal nerve fiber layer thickness by scanning laser polarimetry. *American journal of ophthalmology*, 129(6), 715–722.
- Grewal, D. S., Sehi, M., & Greenfield, D. S. (2011). Detecting glaucomatous progression using GDx with variable and enhanced corneal compensation

- using Guided Progression Analysis. *The British journal of ophthalmology*, 95(4), 502–508. doi:10.1136/bjo.2010.180810
- Grieshaber, M. C., & Flammer, J. (2005). Blood flow in glaucoma. *Current opinion in ophthalmology*, 16(2), 79–83.
- Grunwald, J. E., Piltz, J., Hariprasad, S. M., Dupont, J., & Maguire, M. G. (1999). Optic nerve blood flow in glaucoma: effect of systemic hypertension. *American journal of ophthalmology*, 127(5), 516–522.
- Harwerth, R S, Carter-Dawson, L., Shen, F., Smith, E. L., 3rd, & Crawford, M. L. (1999). Ganglion cell losses underlying visual field defects from experimental glaucoma. *Investigative ophthalmology & visual science*, 40(10), 2242–2250.
- Harwerth, Ronald S, Carter-Dawson, L., Smith, E. L., 3rd, & Crawford, M. L. J. (2005). Scaling the structure--function relationship for clinical perimetry. *Acta ophthalmologica Scandinavica*, 83(4), 448–455. doi:10.1111/j.1395-3907.2005.00494.x
- Harwerth, Ronald S, & Quigley, H. A. (2006). Visual field defects and retinal ganglion cell losses in patients with glaucoma. *Archives of ophthalmology*, 124(6), 853–859. doi:10.1001/archopht.124.6.853
- Healey, P. R., Mitchell, P., Smith, W., & Wang, J. J. (1998). Optic disc hemorrhages in a population with and without signs of glaucoma. *Ophthalmology*, 105(2), 216–223.
- Heijl, A., Bengtsson, B., Chauhan, B. C., Lieberman, M. F., Cunliffe, I., Hyman, L., & Leske, M. C. (2008). A comparison of visual field progression criteria of 3 major glaucoma trials in early manifest glaucoma trial patients. *Ophthalmology*, 115(9), 1557–1565. doi:10.1016/j.optha.2008.02.005

- Heijl, A., Bengtsson, B., Hyman, L., Leske, M. C., & Early Manifest Glaucoma Trial Group. (2009). Natural history of open-angle glaucoma. *Ophthalmology*, *116*(12), 2271–2276. doi:10.1016/j.ophtha.2009.06.042
- Hoh, S. T., Ishikawa, H., Greenfield, D. S., Liebmann, J. M., Chew, S. J., & Ritch, R. (1998). Peripapillary nerve fiber layer thickness measurement reproducibility using scanning laser polarimetry. *Journal of glaucoma*, *7*(1), 12–15.
- Hong, J. T., Sung, K. R., Cho, J. W., Yun, S.-C., Kang, S. Y., & Kook, M. S. (2012). Retinal Nerve Fiber Layer Measurement Variability with Spectral Domain Optical Coherence Tomography. *Korean Journal of Ophthalmology*, *26*(1), 32. doi:10.3341/kjo.2012.26.1.32
- Hood, D. C., Anderson, S. C., Wall, M., & Kardon, R. H. (2007). Structure versus function in glaucoma: an application of a linear model. *Investigative ophthalmology & visual science*, *48*(8), 3662–3668. doi:10.1167/iovs.06-1401
- Hood, D. C., & Kardon, R. H. (2007). A framework for comparing structural and functional measures of glaucomatous damage. *Progress in retinal and eye research*, *26*(6), 688–710. doi:10.1016/j.preteyeres.2007.08.001
- Hoyt, W. F., Frisén, L., & Newman, N. M. (1973). Fundoscopy of nerve fiber layer defects in glaucoma. *Investigative ophthalmology*, *12*(11), 814–829.
- Huang, D., Swanson, E. A., Lin, C. P., Schuman, J. S., Stinson, W. G., Chang, W., ... Puliafito, C. A. (1991). Optical coherence tomography. *Science (New York, N.Y.)*, *254*(5035), 1178–1181.
- Izzotti, A., Saccà, S. C., Cartiglia, C., & De Flora, S. (2003). Oxidative deoxyribonucleic acid damage in the eyes of glaucoma patients. *The American journal of medicine*, *114*(8), 638–646.

- Jampel, H. D., Friedman, D., Quigley, H., Vitale, S., Miller, R., Knezevich, F., & Ding, Y. (2009). Agreement among glaucoma specialists in assessing progressive disc changes from photographs in open-angle glaucoma patients. *American journal of ophthalmology*, *147*(1), 39–44.e1. doi:10.1016/j.ajo.2008.07.023
- Jansonius, N. M., Nevalainen, J., Selig, B., Zangwill, L. M., Sample, P. A., Budde, W. M., ... Schiefer, U. (2009). A mathematical description of nerve fiber bundle trajectories and their variability in the human retina. *Vision Research*, *49*(17), 2157–2163. doi:10.1016/j.visres.2009.04.029
- Johnson, C. A., Cioffi, G. A., Liebmann, J. R., Sample, P. A., Zangwill, L. M., & Weinreb, R. N. (2000). The relationship between structural and functional alterations in glaucoma: a review. *Seminars in ophthalmology*, *15*(4), 221–233.
- Jonas, J. B., & Dichtl, A. (1996). Evaluation of the retinal nerve fiber layer. *Survey of ophthalmology*, *40*(5), 369–378.
- Jonas, J. B., Fernández, M. C., & Naumann, G. O. (1992). Glaucomatous parapapillary atrophy. Occurrence and correlations. *Archives of ophthalmology*, *110*(2), 214–222.
- Jonas, J. B., Fernández, M. C., & Stürmer, J. (1993). Pattern of glaucomatous neuroretinal rim loss. *Ophthalmology*, *100*(1), 63–68.
- Jonas, J. B., Gusek, G. C., & Naumann, G. O. (1988a). Optic disc, cup and neuroretinal rim size, configuration and correlations in normal eyes. *Investigative ophthalmology & visual science*, *29*(7), 1151–1158.
- Jonas, J. B., Gusek, G. C., & Naumann, G. O. (1988b). Optic disc morphometry in chronic primary open-angle glaucoma. I. Morphometric intrapapillary characteristics. *Graefe's archive for clinical and experimental ophthalmology =*

Albrecht von Graefes Archiv für klinische und experimentelle Ophthalmologie,
226(6), 522–530.

Jonas, J. B., Gusek, G. C., & Naumann, G. O. (1988c). Optic disc morphometry in chronic primary open-angle glaucoma. II. Correlation of the intrapapillary morphometric data to visual field indices. *Graefes archive for clinical and experimental ophthalmology = Albrecht von Graefes Archiv für klinische und experimentelle Ophthalmologie*, 226(6), 531–538.

Jonas, J. B., & Naumann, G. O. (1989). Parapapillary chorioretinal atrophy in normal and glaucoma eyes. II. Correlations. *Investigative ophthalmology & visual science*, 30(5), 919–926.

Jonas, J. B., Nguyen, X. N., Gusek, G. C., & Naumann, G. O. (1989). Parapapillary chorioretinal atrophy in normal and glaucoma eyes. I. Morphometric data. *Investigative ophthalmology & visual science*, 30(5), 908–918.

Katz, J., Gilbert, D., Quigley, H. A., & Sommer, A. (1997). Estimating progression of visual field loss in glaucoma. *Ophthalmology*, 104(6), 1017–1025.

Kelly, D. H. (1966). Frequency Doubling in Visual Responses. *Journal of the Optical Society of America*, 56(11), 1628. doi:10.1364/JOSA.56.001628

Kerrigan-Baumrind, L. A., Quigley, H. A., Pease, M. E., Kerrigan, D. F., & Mitchell, R. S. (2000). Number of ganglion cells in glaucoma eyes compared with threshold visual field tests in the same persons. *Investigative ophthalmology & visual science*, 41(3), 741–748.

Knighton, R. W., Huang, X., & Zhou, Q. (1998). Microtubule contribution to the reflectance of the retinal nerve fiber layer. *Investigative ophthalmology & visual science*, 39(1), 189–193.

- Kovalska, M., Grieshaber, M. C., Schötzau, A., Katamay, R., Hauenstein, D., Flammer, J., & Orgül, S. (2008). Detection of visual field progression in glaucoma. *Klinische Monatsblätter für Augenheilkunde*, 225(5), 342–345. doi:10.1055/s-2008-1027289
- Krige, D. (1951). A Statistical Approach to Some Basic Mine Valuation Problems on the Witwatersrand. *Journal of the Chemical, Metallurgical and Mining Society of South Africa*, 52(6), 119–139.
- Kruse, F. E., Burk, R. O., Völcker, H. E., Zinser, G., & Harbarth, U. (1989). Reproducibility of topographic measurements of the optic nerve head with laser tomographic scanning. *Ophthalmology*, 96(9), 1320–1324.
- Laird, N. M., & Ware, J. H. (1982). Random-Effects Models for Longitudinal Data. *Biometrics*, 38(4), 963. doi:10.2307/2529876
- Langenegger, S. J., Funk, J., & Töteberg-Harms, M. (2011). Reproducibility of retinal nerve fiber layer thickness measurements using the eye tracker and the retest function of Spectralis SD-OCT in glaucomatous and healthy control eyes. *Investigative ophthalmology & visual science*, 52(6), 3338–3344. doi:10.1167/iovs.10-6611
- Lee, E. J., Kim, T.-W., Weinreb, R. N., Park, K. H., Kim, S. H., & Kim, D. M. (2011). Trend-based analysis of retinal nerve fiber layer thickness measured by optical coherence tomography in eyes with localized nerve fiber layer defects. *Investigative ophthalmology & visual science*, 52(2), 1138–1144. doi:10.1167/iovs.10-5975
- Leite, M. T., Zangwill, L. M., Weinreb, R. N., Rao, H. L., Alencar, L. M., & Medeiros, F. A. (2012). Structure-function relationships using the Cirrus spectral domain

- optical coherence tomograph and standard automated perimetry. *Journal of glaucoma*, 21(1), 49–54. doi:10.1097/IJG.0b013e31822af27a
- Leske, M. C., Heijl, A., Hyman, L., & Bengtsson, B. (1999). Early Manifest Glaucoma Trial: design and baseline data. *Ophthalmology*, 106(11), 2144–2153.
- Leung, C. K., Cheung, C. Y. L., Weinreb, R. N., Qiu, K., Liu, S., Li, H., ... Lam, D. S. C. (2010). Evaluation of retinal nerve fiber layer progression in glaucoma: a study on optical coherence tomography guided progression analysis. *Investigative ophthalmology & visual science*, 51(1), 217–222. doi:10.1167/iavs.09-3468
- Leung, C. K., Cheung, C. Y., Lin, D., Pang, C. P., Lam, D. S. C., & Weinreb, R. N. (2008). Longitudinal variability of optic disc and retinal nerve fiber layer measurements. *Investigative ophthalmology & visual science*, 49(11), 4886–4892. doi:10.1167/iavs.07-1187
- Leung, C. K., Chong, K. K.-L., Chan, W., Yiu, C. K.-F., Tso, M., Woo, J., ... Yung, W. (2005). Comparative study of retinal nerve fiber layer measurement by StratusOCT and GDx VCC, II: structure/function regression analysis in glaucoma. *Investigative ophthalmology & visual science*, 46(10), 3702–3711. doi:10.1167/iavs.05-0490
- Leung, C. K. S., Yu, M., Weinreb, R. N., Ye, C., Liu, S., Lai, G., & Lam, D. S. C. (2012). Retinal nerve fiber layer imaging with spectral-domain optical coherence tomography: a prospective analysis of age-related loss. *Ophthalmology*, 119(4), 731–737. doi:10.1016/j.ophtha.2011.10.010
- Leung, C. K., Ye, C., Weinreb, R. N., Cheung, C. Y. L., Qiu, Q., Liu, S., ... Lam, D. S. C. (2010). Retinal nerve fiber layer imaging with spectral-domain optical

- coherence tomography a study on diagnostic agreement with Heidelberg Retinal Tomograph. *Ophthalmology*, 117(2), 267–274.
doi:10.1016/j.ophtha.2009.06.061
- Leung, C. K.-S., Cheung, C. Y.-L., Weinreb, R. N., Qiu, Q., Liu, S., Li, H., ... Lam, D. S. C. (2009). Retinal nerve fiber layer imaging with spectral-domain optical coherence tomography: a variability and diagnostic performance study. *Ophthalmology*, 116(7), 1257–1263, 1263.e1–2.
doi:10.1016/j.ophtha.2009.04.013
- Leung, C. K.-S., Chiu, V., Weinreb, R. N., Liu, S., Ye, C., Yu, M., ... Lam, D. S.-C. (2011). Evaluation of retinal nerve fiber layer progression in glaucoma: a comparison between spectral-domain and time-domain optical coherence tomography. *Ophthalmology*, 118(8), 1558–1562. doi:10.1016/j.ophtha.2011.01.026
- Leung, C. K.-S., Yu, M., Weinreb, R. N., Lai, G., Xu, G., & Lam, D. S.-C. (2012). Retinal nerve fiber layer imaging with spectral-domain optical coherence tomography: patterns of retinal nerve fiber layer progression. *Ophthalmology*, 119(9), 1858–1866. doi:10.1016/j.ophtha.2012.03.044
- Levkovitch-Verbin, H., Quigley, H. A., Martin, K. R. G., Valenta, D., Baumrind, L. A., & Pease, M. E. (2002). Translimbal laser photocoagulation to the trabecular meshwork as a model of glaucoma in rats. *Investigative ophthalmology & visual science*, 43(2), 402–410.
- Liu, B., & Neufeld, A. H. (2000). Expression of nitric oxide synthase-2 (NOS-2) in reactive astrocytes of the human glaucomatous optic nerve head. *Glia*, 30(2), 178–186.

- Liu, B., & Neufeld, A. H. (2001). Nitric oxide synthase-2 in human optic nerve head astrocytes induced by elevated pressure in vitro. *Archives of ophthalmology*, *119*(2), 240–245.
- Lucas, D. R., & Newhouse, J. P. (1957). The toxic effect of sodium L-glutamate on the inner layers of the retina. *A.M.A. archives of ophthalmology*, *58*(2), 193–201.
- McNaught, A. I., Crabb, D. P., Fitzke, F. W., & Hitchings, R. A. (1995). Modelling series of visual fields to detect progression in normal-tension glaucoma. *Graefe's archive for clinical and experimental ophthalmology = Albrecht von Graefes Archiv für klinische und experimentelle Ophthalmologie*, *233*(12), 750–755.
- Medeiros, F. A., Alencar, L. M., Zangwill, L. M., Bowd, C., Vizzeri, G., Sample, P. A., & Weinreb, R. N. (2009). Detection of Progressive Retinal Nerve Fiber Layer Loss in Glaucoma Using Scanning Laser Polarimetry with Variable Corneal Compensation. *Investigative Ophthalmology & Visual Science*, *50*(4), 1675–1681. doi:10.1167/iovs.08-2712
- Medeiros, F. A., Zangwill, L. M., Bowd, C., & Weinreb, R. N. (2004). Comparison of the GDx VCC Scanning Laser Polarimeter, HRT II Confocal Scanning Laser Ophthalmoscope, and Stratus OCT Optical Coherence Tomograph for the Detection of Glaucoma. *Archives of Ophthalmology*, *122*(6), 827–837. doi:10.1001/archophth.122.6.827
- Medeiros, Felipe A, Alencar, L. M., Zangwill, L. M., Bowd, C., Sample, P. A., & Weinreb, R. N. (2009). Prediction of functional loss in glaucoma from progressive optic disc damage. *Archives of ophthalmology*, *127*(10), 1250–1256. doi:10.1001/archophthalmol.2009.276

- Medeiros, Felipe A, Bowd, C., Zangwill, L. M., Patel, C., & Weinreb, R. N. (2007). Detection of glaucoma using scanning laser polarimetry with enhanced corneal compensation. *Investigative ophthalmology & visual science*, 48(7), 3146–3153. doi:10.1167/iovs.06-1139
- Medeiros, Felipe A, Leite, M. T., Zangwill, L. M., & Weinreb, R. N. (2011). Combining structural and functional measurements to improve detection of glaucoma progression using Bayesian hierarchical models. *Investigative ophthalmology & visual science*, 52(8), 5794–5803. doi:10.1167/iovs.10-7111
- Medeiros, Felipe A, Zangwill, L. M., Alencar, L. M., Bowd, C., Sample, P. A., Susanna, R., Jr, & Weinreb, R. N. (2009). Detection of glaucoma progression with stratus OCT retinal nerve fiber layer, optic nerve head, and macular thickness measurements. *Investigative ophthalmology & visual science*, 50(12), 5741–5748. doi:10.1167/iovs.09-3715
- Menke, M. N., Knecht, P., Sturm, V., Dabov, S., & Funk, J. (2008). Reproducibility of nerve fiber layer thickness measurements using 3D fourier-domain OCT. *Investigative ophthalmology & visual science*, 49(12), 5386–5391. doi:10.1167/iovs.07-1435
- Michelson, G., Langhans, M. J., Harazny, J., & Dichtl, A. (1998). Visual field defect and perfusion of the juxtapapillary retina and the neuroretinal rim area in primary open-angle glaucoma. *Graefe's archive for clinical and experimental ophthalmology = Albrecht von Graefes Archiv für klinische und experimentelle Ophthalmologie*, 236(2), 80–85.
- Mikelberg, F. S., Schulzer, M., Drance, S. M., & Lau, W. (1986). The rate of progression of scotomas in glaucoma. *American journal of ophthalmology*, 101(1), 1–6.

- Mikelberg, F. S., Wijsman, K., & Schulzer, M. (1993). Reproducibility of topographic parameters obtained with the heidelberg retina tomograph. *Journal of glaucoma*, 2(2), 101–103.
- Moncada, S., & Higgs, A. (1993). The L-arginine-nitric oxide pathway. *The New England journal of medicine*, 329(27), 2002–2012.
doi:10.1056/NEJM199312303292706
- Moon, B. G., Sung, K. R., Cho, J. W., Kang, S. Y., Yun, S.-C., Na, J. H., ... Kook, M. S. (2012). Glaucoma progression detection by retinal nerve fiber layer measurement using scanning laser polarimetry: event and trend analysis. *Korean journal of ophthalmology: KJO*, 26(3), 174–181.
doi:10.3341/kjo.2012.26.3.174
- Morgan, J. E., Sheen, N. J. L., North, R. V., Goyal, R., Morgan, S., Ansari, E., & Wild, J. M. (2005). Discrimination of glaucomatous optic neuropathy by digital stereoscopic analysis. *Ophthalmology*, 112(5), 855–862.
doi:10.1016/j.ophtha.2004.11.056
- Musch, D. C., Lichter, P. R., Guire, K. E., & Standardi, C. L. (1999). The Collaborative Initial Glaucoma Treatment Study: study design, methods, and baseline characteristics of enrolled patients. *Ophthalmology*, 106(4), 653–662.
- Na, J. H., Sung, K. R., Lee, J. R., Lee, K. S., Baek, S., Kim, H. K., & Sohn, Y. H. (2013). Detection of Glaucomatous Progression by Spectral-Domain Optical Coherence Tomography. *Ophthalmology*. doi:10.1016/j.ophtha.2012.12.014
- Neal, M. J., Cunningham, J. R., Hutson, P. H., & Hogg, J. (1994). Effects of ischaemia on neurotransmitter release from the isolated retina. *Journal of neurochemistry*, 62(3), 1025–1033.

- Neufeld, A. H. (1999). Nitric oxide: a potential mediator of retinal ganglion cell damage in glaucoma. *Survey of ophthalmology*, *43 Suppl 1*, S129–135.
- O’Leary, N, Artes, P. H., Hutchison, D. M., Nicoletta, M. T., & Chauhan, B. C. (2012). Rates of retinal nerve fibre layer thickness change in glaucoma patients and control subjects. *Eye (London, England)*, *26*(12), 1554–1562.
doi:10.1038/eye.2012.202
- O’Leary, Neil, Crabb, D. P., Mansberger, S. L., Fortune, B., Twa, M. D., Lloyd, M. J., ... Johnson, C. A. (2010). Glaucomatous progression in series of stereoscopic photographs and Heidelberg retina tomograph images. *Archives of ophthalmology*, *128*(5), 560–568. doi:10.1001/archophthalmol.2010.52
- Olney, J. W. (1969). Glutamate-induced retinal degeneration in neonatal mice. Electron microscopy of the acutely evolving lesion. *Journal of neuropathology and experimental neurology*, *28*(3), 455–474.
- Pascolini, D., & Mariotti, S. P. (2011). Global estimates of visual impairment: 2010. *British Journal of Ophthalmology*, *96*(5), 614–618. doi:10.1136/bjophthalmol-2011-300539
- Patterson, A. J., Garway-Heath, D. F., Strouthidis, N. G., & Crabb, D. P. (2005). A new statistical approach for quantifying change in series of retinal and optic nerve head topography images. *Investigative ophthalmology & visual science*, *46*(5), 1659–1667. doi:10.1167/iovs.04-0953
- Paunescu, L. A., Schuman, J. S., Price, L. L., Stark, P. C., Beaton, S., Ishikawa, H., ... Fujimoto, J. G. (2004). Reproducibility of nerve fiber thickness, macular thickness, and optic nerve head measurements using StratusOCT. *Investigative ophthalmology & visual science*, *45*(6), 1716–1724.

- Quigley, H A, & Addicks, E. M. (1982). Quantitative studies of retinal nerve fiber layer defects. *Archives of ophthalmology*, 100(5), 807–814.
- Quigley, H A, Addicks, E. M., & Green, W. R. (1982). Optic nerve damage in human glaucoma. III. Quantitative correlation of nerve fiber loss and visual field defect in glaucoma, ischemic neuropathy, papilledema, and toxic neuropathy. *Archives of ophthalmology*, 100(1), 135–146.
- Quigley, H A, & Broman, A. T. (2006). The number of people with glaucoma worldwide in 2010 and 2020. *The British journal of ophthalmology*, 90(3), 262–267.
doi:10.1136/bjo.2005.081224
- Quigley, H A, Katz, J., Derick, R. J., Gilbert, D., & Sommer, A. (1992). An evaluation of optic disc and nerve fiber layer examinations in monitoring progression of early glaucoma damage. *Ophthalmology*, 99(1), 19–28.
- Quigley, Harry A. (2011). Glaucoma. *Lancet*, 377(9774), 1367–1377.
doi:10.1016/S0140-6736(10)61423-7
- Rahiala, M. (1999). Miscellanea. Random coefficient autoregressive models for longitudinal data. *Biometrika*, 86(3), 718–722. doi:10.1093/biomet/86.3.718
- Ramsay, J. O., & Dalzell, C. J. (1991). Some Tools for Functional Data Analysis. *Journal of the Royal Statistical Society. Series B (Statistical Methodology)*, 53, 539–572.
- Rao, Harsha L, Venkatesh, C. R., Vidyasagar, K., Yadav, R. K., Addepalli, U. K., Jude, A., ... Garudadri, C. S. (2013). Retinal Nerve Fiber Layer Measurements by Scanning Laser Polarimetry With Enhanced Corneal Compensation in Healthy Subjects. *Journal of glaucoma*. doi:10.1097/IJG.0b013e318286ffa5

- Rao, Harsha Laxmana, Jonnadula, G. B., Addepalli, U. K., Senthil, S., & Garudadri, C. S. (2013). Effect of cataract extraction on Visual Field Index in glaucoma. *Journal of glaucoma*, 22(2), 164–168. doi:10.1097/IJG.0b013e31822e8e37
- Resnikoff, S., & Keys, T. (2012). Future trends in global blindness. *Indian Journal of Ophthalmology*, 60(5), 387. doi:10.4103/0301-4738.100532
- Reus, N. J., & Lemij, H. G. (2004). Diagnostic accuracy of the GDx VCC for glaucoma. *Ophthalmology*, 111(10), 1860–1865. doi:10.1016/j.ophtha.2004.04.024
- Saccà, S. C., Pascotto, A., Camicione, P., Capris, P., & Izzotti, A. (2005). Oxidative DNA damage in the human trabecular meshwork: clinical correlation in patients with primary open-angle glaucoma. *Archives of ophthalmology*, 123(4), 458–463. doi:10.1001/archopht.123.4.458
- Schuman, J. S., Pedut-Kloizman, T., Hertzmark, E., Hee, M. R., Wilkins, J. R., Coker, J. G., ... Swanson, E. A. (1996). Reproducibility of nerve fiber layer thickness measurements using optical coherence tomography. *Ophthalmology*, 103(11), 1889–1898.
- Self, S. G., & Liang, K.-Y. (1987). Asymptotic Properties of Maximum Likelihood Estimators and Likelihood Ratio Tests Under Nonstandard Conditions. *Journal of the American Statistical Association*, 82(398), 605. doi:10.2307/2289471
- Smith, S. D., Katz, J., & Quigley, H. A. (1996). Analysis of progressive change in automated visual fields in glaucoma. *Investigative ophthalmology & visual science*, 37(7), 1419–1428.
- Swindale, N. V., Stjepanovic, G., Chin, A., & Mikelberg, F. S. (2000). Automated analysis of normal and glaucomatous optic nerve head topography images. *Investigative ophthalmology & visual science*, 41(7), 1730–1742.

- Tezel, G., Kolker, A. E., Kass, M. A., Wax, M. B., Gordon, M., & Siegmund, K. D. (1997). Parapapillary chorioretinal atrophy in patients with ocular hypertension. I. An evaluation as a predictive factor for the development of glaucomatous damage. *Archives of ophthalmology*, *115*(12), 1503–1508.
- Tezel, G., Kolker, A. E., Wax, M. B., Kass, M. A., Gordon, M., & Siegmund, K. D. (1997). Parapapillary chorioretinal atrophy in patients with ocular hypertension. II. An evaluation of progressive changes. *Archives of ophthalmology*, *115*(12), 1509–1514.
- The Advanced Glaucoma Intervention Study (AGIS): 1. Study design and methods and baseline characteristics of study patients. (1994). *Controlled clinical trials*, *15*(4), 299–325.
- Tóth, M., & Holló, G. (2005). Enhanced corneal compensation for scanning laser polarimetry on eyes with atypical polarisation pattern. *The British journal of ophthalmology*, *89*(9), 1139–1142. doi:10.1136/bjo.2005.070011
- Van der Schoot, J., Reus, N. J., Colen, T. P., & Lemij, H. G. (2010). The ability of short-wavelength automated perimetry to predict conversion to glaucoma. *Ophthalmology*, *117*(1), 30–34. doi:10.1016/j.opthta.2009.06.046
- Vesti, E., Johnson, C. A., & Chauhan, B. C. (2003). Comparison of different methods for detecting glaucomatous visual field progression. *Investigative ophthalmology & visual science*, *44*(9), 3873–3879.
- Viswanathan, A. C., Crabb, D. P., McNaught, A. I., Westcott, M. C., Kamal, D., Garway-Heath, D. F., ... Hitchings, R. A. (2003). Interobserver agreement on visual field progression in glaucoma: a comparison of methods. *The British journal of ophthalmology*, *87*(6), 726–730.

- Vizzeri, G., Weinreb, R. N., Gonzalez-Garcia, A. O., Bowd, C., Medeiros, F. A., Sample, P. A., & Zangwill, L. M. (2009). Agreement between spectral-domain and time-domain OCT for measuring RNFL thickness. *The British journal of ophthalmology*, *93*(6), 775–781. doi:10.1136/bjo.2008.150698
- Vorwerk, C. K., Lipton, S. A., Zurakowski, D., Hyman, B. T., Sabel, B. A., & Dreyer, E. B. (1996). Chronic low-dose glutamate is toxic to retinal ganglion cells. Toxicity blocked by memantine. *Investigative ophthalmology & visual science*, *37*(8), 1618–1624.
- Webb, R. H., Hughes, G. W., & Delori, F. C. (1987). Confocal scanning laser ophthalmoscope. *Applied optics*, *26*(8), 1492–1499.
- Weber, J., & Ulrich, H. (1991). A perimetric nerve fiber bundle map. *International ophthalmology*, *15*(3), 193–200.
- Weinreb, R N, Dreher, A. W., & Bille, J. F. (1989). Quantitative assessment of the optic nerve head with the laser tomographic scanner. *International ophthalmology*, *13*(1-2), 25–29.
- Weinreb, R N, Dreher, A. W., Coleman, A., Quigley, H., Shaw, B., & Reiter, K. (1990). Histopathologic validation of Fourier-ellipsometry measurements of retinal nerve fiber layer thickness. *Archives of ophthalmology*, *108*(4), 557–560.
- Weinreb, R N, Lusky, M., Bartsch, D. U., & Morsman, D. (1993). Effect of repetitive imaging on topographic measurements of the optic nerve head. *Archives of ophthalmology*, *111*(5), 636–638.
- Weinreb, R N, Zangwill, L., Berry, C. C., Bathija, R., & Sample, P. A. (1998). Detection of glaucoma with scanning laser polarimetry. *Archives of ophthalmology*, *116*(12), 1583–1589.

- Weinreb, Robert N, Bowd, C., Greenfield, D. S., & Zangwill, L. M. (2002). Measurement of the magnitude and axis of corneal polarization with scanning laser polarimetry. *Archives of ophthalmology*, 120(7), 901–906.
- Wojtkowski, M., Leitgeb, R., Kowalczyk, A., Bajraszewski, T., & Fercher, A. F. (2002). In vivo human retinal imaging by Fourier domain optical coherence tomography. *Journal of biomedical optics*, 7(3), 457–463. doi:10.1117/1.1482379
- Wollstein, G, Garway-Heath, D. F., & Hitchings, R. A. (1998). Identification of early glaucoma cases with the scanning laser ophthalmoscope. *Ophthalmology*, 105(8), 1557–1563. doi:10.1016/S0161-6420(98)98047-2
- Wollstein, Gadi, Schuman, J. S., Price, L. L., Aydin, A., Stark, P. C., Hertzmark, E., ... Paunescu, L. A. (2005). Optical coherence tomography longitudinal evaluation of retinal nerve fiber layer thickness in glaucoma. *Archives of ophthalmology*, 123(4), 464–470. doi:10.1001/archophth.123.4.464
- Wu, H., de Boer, J. F., & Chen, T. C. (2012). Diagnostic capability of spectral-domain optical coherence tomography for glaucoma. *American journal of ophthalmology*, 153(5), 815–826.e2. doi:10.1016/j.ajo.2011.09.032
- Yamamoto, T., Iwase, A., Kawase, K., Sawada, A., & Ishida, K. (2004). Optic disc hemorrhages detected in a large-scale eye disease screening project. *Journal of glaucoma*, 13(5), 356–360.
- Yaqoob, Z., Wu, J., & Yang, C. (2005). Spectral domain optical coherence tomography: a better OCT imaging strategy. *BioTechniques*, 39(6 Suppl), S6–13. doi:10.2144/000112090

- Zhou, Q. (2006). Retinal scanning laser polarimetry and methods to compensate for corneal birefringence. *Bulletin de la Société belge d'ophtalmologie*, (302), 89–106.
- Zhou, Qienyuan, & Weinreb, R. N. (2002). Individualized compensation of anterior segment birefringence during scanning laser polarimetry. *Investigative ophthalmology & visual science*, 43(7), 2221–2228.

APPENDIX

NON-PROVISIONAL PATENT APPLICATION DETECTION OF DISEASE-RELATED RETINAL NERVE FIBER LAYER THINNING

Inventor(s): Christopher Kai-Shun Leung
21A Grand Excelsior, 83 Waterloo Road, Hong Kong SAR, China

Marco Chak-Yan Yu
2/F, 309
Tseng Tau Tsuen, Sai Kung
Hong Kong SAR, China

Dennis Shun-Chiu Lam
Flat C, 63/F, Tower 1, Sorrento, No.1
Austin Road West
Tsimshatsui, Kowloon,
Hong Kong SAR, China

Assignee: THE CHINESE UNIVERSITY OF HONG KONG
Knowledge Transfer Office
Shatin, N.T., Hong Kong SAR, China

Entity: Small

KILPATRICK TOWNSEND & STOCKTON LLP
Two Embarcadero Center, Eighth Floor
San Francisco, California 94111-3834
Tel: 415-576-0200

Detection of Disease Related Retinal Nerve Fiber Layer Thinning

CROSS REFERENCES TO RELATED APPLICATIONS

- 5 [0001] This application claims priority to U.S. Provisional Application 61/649,896, filed May 21, 2012, and titled “Detection of Retinal Nerve Fiber Layer Thinning,” the disclosure of which is incorporated herein in its entirety and for all purposes.

FIELD OF INVENTION

- 10 [0002] Embodiments of the present invention generally relate to the design and development of novel methods to analyze progressive retinal nerve fiber layer (RNFL) thinning in patients with possible eye abnormalities, such as glaucoma and different types of optic neuropathies.

BACKGROUND

- 15 [0003] Glaucoma is the most common type of optic neuropathies and a leading cause of irreversible blindness worldwide. Characterized by progressive loss of retinal ganglion cells, measurement of their axon bundles – the retinal nerve fiber layer (RNFL) would be useful to detect and track the progression of the disease. The Guided Progression Analysis (GPA) (Carl Zeiss Meditec, Dublin, CA) is a commercially available algorithm to detect longitudinal RNFL changes in the RNFL thickness map using spectral-domain optical coherence tomography (OCT). In the analysis of RNFL thinning, change at individual pixels may be displayed in the RNFL thickness change map if the differences between two baseline visits and one follow visit are statistically greater than the test-retest variability of that particular pixel. However, the ability of GPA on the RNFL thickness map for detection of progressive RNFL thinning can be limited.
- 25

- [0004] It is therefore desirable to provide improved methods and systems for detecting early progressive RNFL thinning. The current invention is designed to address these issues.

SUMMARY

[0005] Embodiments relate to methods, apparatuses, and computer readable media for detecting abnormalities in the retinal nerve fiber thickness (or other characteristic) of an eye using imaging methods, for example spectral-domain optical coherence tomography (OCT).

5 **[0006]** Some embodiments include receiving a plurality of images of the patient's eye, where each image is obtained at a different time. Each image of the plurality of images may be made up of a plurality of pixels, each pixel indicating a time-varying characteristic of a particular location in the patient's eye. Each image may be divided into a plurality of pixel partitions, where each pixel partition includes one or more
10 pixels, e.g., 2x2 pixels, 4x4 pixels, 10x10 pixels, or just one pixel. A plurality of pixel partition sets may be identified, where each pixel partition set includes a pixel partition from each image and the pixel partitions of the same pixel partition set correspond to a common region in the patient's eye. For each pixel partition set, and for each pixel partition of each pixel partition set, a respective value for the respective common region
15 of the pixel partition set may be determined, e.g., an average of the pixel values.

[0007] The respective value may correspond to a time-varying characteristic of the pixel partition at the time of the corresponding image. A regression model for each pixel partition set may then be calculated from the respective values of the pixel partitions, with a computer system. The regression model may include a rate of change value at
20 individual pixel partitions. Then, it may be determined whether the common region that corresponds to the pixel partition set exhibits at least one abnormality in the patient's eye if the rate of change of the regression model is more negative than the age-related change of that particular pixel partition. The age-related changes may be determined from a longitudinal dataset collected from a normal healthy cohort. In some
25 embodiments, a false discovery rate of the detected abnormalities is computed. Once an abnormality has been identified a disease prognosis and a treatment plan can be provided.

[0008] Other embodiments may include functional regression models that include non-linear polynomial terms or autocorrelation terms. Embodiments are also directed to
30 systems and computer readable media associated with methods described herein.

BRIEF DESCRIPTION OF THE DRAWINGS

[0009] A further understanding of the nature and advantages of various embodiments may be realized by reference to the following figures. In the appended figures, similar components or features may have the same reference label. Further, various components
5 of the same type may be distinguished by following the reference label by a dash and a second label that distinguishes among the similar components. If only the first reference label is used in the specification, the description is applicable to any one of the similar components having the same first reference label irrespective of the second reference label.

10 **[0010]** FIG. 1A is a flowchart of a method according to embodiments of the present invention.

[0011] FIG. 1B is a flowchart of additional method steps according to some embodiments.

15 **[0012]** FIGs. 2A-2D, and 3A-3D are illustrative results comparing existing methods (GPA) and methods and apparatuses of embodiments of the present invention.

[0013] FIG. 4 illustrates the importance of accounting for age-related change as part of the embodiments of the present invention.

[0014] FIG. 5 is a graphical illustration showing a regression model according to embodiments of the present invention.

20 **[0015]** FIG. 6 shows a computer system of various embodiments of the present invention.

DETAILED DESCRIPTION

[0016] Embodiments of the present invention describe a functional regressive modeling approach to detect disease-related RNFL changes in individual pixels of
25 RNFL thickness images of a patient's eye, measured at different time points. RNFL changes detected in the patient's eye, as measured by analyzing certain data in the functional regressive models, if greater than the age-related change, may signal eye abnormalities, such as glaucoma.

[0017] Commercially-available algorithms for detecting longitudinal RNFL changes
30 in the RNFL thickness map using spectral-domain optical coherence tomography (OCT)

can be limited. For example, the detection method may not be sensitive enough to detect early change. Second, even if a change is detected, the change may not be disease-related. In other words, the current method may not differentiate disease-related from age-related change. Third, statistical test performed at multiple pixels in the RNFL thickness map would increase the likelihood of detecting false positives. A method providing information about the specificity of the detected changes is important for interpretation of the analysis. Irreversible loss of vision could occur in patients with glaucoma if treatment is not provided at the early stage of disease when progression is detected. On the other hand, patients may be over-treated if the detected changes are age-related or false positives.

[0018] Embodiments of the present invention may solve these and other problems, including differentiating disease-related from age-related change and reporting the false detection rate of the change analysis in a patient's eye.

[0019] For example, embodiments of the present invention may include eight 2-dimensional digital images of a patient's eye, wherein each image is taken every four months over a 3-4 year period, and wherein each image comprises 200 x 200 pixels, each pixel having a value that represents the RNFL thickness at that particular location of the patient's eye. The 200 x 200 pixels are then divided into a plurality of pixel partitions (e.g. 4 x 4 pixels for each partition to form 50 x 50 pixel partitions). The average values of RNFL thickness are calculated in each pixel partition. Embodiments may then calculate a regression model (e.g. least squares linear regression) for each pixel partition by using the RNFL thickness data values from all eight images at the same corresponding location. The regression models of each pixel partition may therefore form a matrix of regression models, arranged in the same order as the partition locations. Each regression model may include a slope value term, which represents the change in RNFL thickness at that particular pixel partition of the patient's eye across the follow-up time period. If a slope value at a pixel partition exceeds the age-related change value of the same pixel location, then it may signal that the RNFL thickness at that location in the eye has an abnormality, such as glaucoma. In some embodiments, the age-related rates of change of RNFL thickness and their 95% confidence intervals at individual pixel partitions are generated from linear mixed modeling on long-term longitudinal RNFL data collected from a cohort of healthy normal eyes.

[0020] Some embodiments may include calculating at least one false discovery rate (FDR) in the matrix of regression models, whose rates of change values signal an abnormality; or controlling the FDR in defining the abnormality threshold for each regression model in the matrix of regression models. The FDR may represent the
5 percent likelihood that the signaled abnormality is a “false positive.” Multiple FDRs in the matrix of the regression models may represent different percent likelihoods (e.g. 5% likely, 25% likely) that the signaled abnormality is a false positive.

[0021] FIGs. 2B-D and 3B-D illustrate some examples of data analysis that may be performed by present embodiments. These examples, among others, will be explained in
10 more detail in the following paragraphs. Specifically, this disclosure is divided into several sections, including detailed descriptions of: I. Method embodiment, II. Regression modeling, III. Regression modeling with error term, IV. False discovery rate, V. Non-linear regression model, VI. Sample data, and VII. Computer system embodiments. First, referring to FIG. 1A, example methods of embodiments of the
15 present invention are described.

I. METHOD

[0022] FIG. 1A is flowchart of a method 100 for identifying regions of abnormalities in a patient’s eye according to embodiments of the present invention. The method includes receiving a plurality of images of a patient’s eye, where each image is
20 composed of a plurality of pixels. Each image is divided into a plurality of pixel partitions, each including at least one pixel of the image. A plurality of pixel partition sets are then determined, each pixel partition set including a pixel partition from each of the images, where each of the pixel partitions correspond to a common region of the patient’s eye. A regression model is then calculated for each pixel partition set, using
25 values determined for each pixel partition of the set. The regression is analyzed to determine whether the common region of the patient’s eye corresponding to the pixel partition set has an abnormality. In some embodiments, this analysis includes measuring a slope value of the regression model.

[0023] In block 102, a plurality of images of the patient’s eye are received. An
30 imaging device may record a plurality of images of a patient’s eye using an imaging device, and these images may be received by a processor or other image repository. Example imaging devices may include magnetic resonance imaging (MRI) devices,

ophthalmology imaging devices (including but not limited to spectral-domain optical coherence tomography, scanning laser polarimetry and polarization sensitive optical coherence tomography), spectral imaging systems, or digital fundus cameras. For clarity, assume that J images of the patient's eye are recorded. Each image may include
5 a plurality of pixels, arranged in any configuration, but may commonly be arranged in a square or rectangular pattern or matrix. Each of the J images is recorded at different times. Certain method embodiments record the J images over a period of years, where each image may be recorded several months apart from each other. One of the purposes of recording the images over such a period may be to create a longer term history of the
10 development of a patient's eye, so that trend analysis can be performed over such a time period.

[0024] The imaging device can then send the images to a computer system. The computer system may include the imaging device, or the imaging device may be networked to the computer system. Alternatively, the images may be recorded on a
15 computer readable medium (e.g. a compact disc), which can be loaded into the computer system. Thus, a computer system can receive the images in various ways. Each of the steps below can be performed by one or various components of a computer system.

[0025] Having obtained the J images, at block 104, each image may be divided into a
20 plurality of pixel partitions, or sub-images, which include one or more pixels. The pixel partitions may be sets of pixels of an image grouped in close proximity to one another. For example, in an image comprised of 40000 pixels arranged in a square 200x200 matrix, the image may be divided by pixel partitions of 4x4 pixels each, for a total of 2500 pixel partitions. The pixel partitions do not have to be uniform in size, and each
25 pixel partition does not have to comprise more than even 1 pixel. The pixel partitions also may not comprise contiguous pixels of the image. For example, in an image comprising 10,000 pixels arranged in a square 100x100 matrix, the image may be divided by pixel partitions comprised of every other pixel in a column and row in a square 10x10 matrix, e.g. the 2nd, 4th, 6th, 8th, and 10th pixels of a row, for each of the
30 2nd, 4th, 6th, 8th, and 10th row comprises one pixel partition. In this example, each pixel partition is arranged in this way, thereby generating 100 pixel partitions of the 100x100 image.

[0026] At block 106, the pixel partitions of each of the J images are grouped with other pixel partitions of every other image, arranged by a correspondence to a common region of the patient's eye. For example, assume there are 8 images of a patient's eye recorded over a span of years, each image comprised of 100 pixels in a 10x10 matrix.

5 The images are divided into pixel partitions of 2x2, with no pixels skipped, for a total of 25 pixel partitions for each image. A pixel partition set, therefore, may comprise the top left pixel 2x2 pixel partition of each of the 8 images, assuming that the top left corner of each image corresponds to the same region of the patient's eye, but recorded at different instances in time. Therefore, the first pixel partition set comprises all of the pixel
10 partitions of each of the 8 images located at the position $\{(1,1), (1,2), (2,1), (2,2)\}$, where (i,j) is the pixel location at the ith row from the top and jth column from the left in a pixel partition matrix. Similarly, another pixel partition set would be the area just to the right of the previously mentioned pixel partition set, at matrix positions $\{(1,3), (1,4), (2,3), (2,4)\}$, comprising 8 pixel partitions, one from each image. Pixel partition sets
15 would be similarly defined in this way, thereby creating 25 pixel partition sets, each comprised of 8 pixel partitions – one from each of the 8 images. In general, it can be seen then that for a plurality J images divided into a plurality of M pixel partitions, M pixel partition sets may be identified, each comprising J pixel partitions.

[0027] Other embodiments may arrange pixel partitions and pixel partition sets in a
20 different way. For example, some may be arranged by matrix location, but others may be aligned where necessary to link the areas of each image corresponding to a common location of the patient's eye. In cases where the location of the patient's eye is slightly skewed or shifted in an image, other analysis and alignment may need to be performed and are not limited in the present invention.

25 **[0028]** In some cases, performing analysis in pixel partitions instead of individual pixels may be preferred. For example, the use of an average value of a pixel partition minimizes alignment error related to imperfect image registration which can be secondary to insistent ocular magnification during the longitudinal follow-up (e.g. patients may undergo cataract surgery and that will change the ocular magnification).
30 Additionally, analyzing data in pixel partition increases the computation efficiency. This is important because the 3D data sets can be very memory-intensive. Analyzing pixel partitions instead of individual pixels would substantially reduce the computation time. Also, there are areas in the retina (e.g. the nasal sector of the optic disc) where RNFL

thinning is unlikely to occur in disease-related or age-related conditions. Using a larger pixel partition in this sector can further improve the computation efficiency.

[0029] Having identified a plurality M of pixel partition sets, at blocks 108, 110 and 112, a regression model analysis is performed for each pixel partition set. As part of the regression model analysis, multiple regression models are calculated. One regression model is calculated for each pixel partition set, and then the regression models are analyzed to determine abnormalities.

[0030] At block 108, a value V for each of the J pixel partitions is determined. Each value V may represent a time variant characteristic of the patient's eye at the location of the pixel partition. For example, the pixels of an image may represent RNFL thickness of a patient's eye, measured in micrometers. A value V then for a pixel partition of 4x4 pixels may be the average RNFL thickness of those 16 pixels. In another example, V may be the RNFL thickness value of the top-left pixel. In an example where pixel partitions comprises a square 3x3 matrix of pixels, V may be defined as simply the RNFL thickness of the central pixel of the 3x3 matrix. The present invention is not limited to the choice of V or how V is derived, but certain methods may rely on the methodology of determining V being made uniformly for all pixel partitions and pixel partition sets.

[0031] At block 110, a regression model is calculated using the values V of each pixel partition in the pixel partition set. The regression model may be a number of different models, including linear regression, ordinary least squares, mean square error regression and the like. The regression model may also trend non-linear curves, and/or be higher ordered polynomial models. More details of the use of regression models in embodiments of the present invention are provided below. However, in general, a purpose of performing regression or trending analysis is to compute and analyze a change in the values V over time.

[0032] At block 112, an analysis of the regression model is performed. In some embodiments, this includes determining whether the values V have changed over time. Such a determination may indicate that the corresponding common region of the pixel partition set exhibits at least one abnormality in the patient's eye. Determining whether there is such a change may be based on analyzing a slope value provided in the regression model. In other embodiments, there may not be a slope value but rather some

sort of non-linear rate of change value that represents a rate of change of the values V for each pixel partition. For example, a regression model running ordinary least squares may comprises a slope value B as a function of time. After calculating an ordinary least squares regression on a pixel partition set, it is found that the slope value B is a

5 statistically significant negative value. However, this may not indicate an abnormality in the particular area of the patient's eye corresponding to the pixel partition set because the change may be age-related. Therefore, the slope value B will be compared with an age-related slope value corresponding to the particular area. If the slope value B is more negative than the lower 95% confidence limit of the age-related slope value in the pixel

10 partition, a disease related change is detected. If the pixel partition set measures RNFL thickness of the patient's eye, this may mean that the patient is suffering from glaucoma or some other eye disease. The slopes of age-related change may vary from pixel partition to pixel partition. These values may be generated from long-term (at least 3 years) longitudinal data obtained from healthy normal eyes with no evidence of any

15 ocular diseases. In some embodiments, a composite model of typical changes due to aging in healthy normal eyes is generated using data sets from multiple healthy patients. This model may be further extended by subdividing the data sets by certain characteristics, e.g. gender, ethnicity, occupation, or other common characteristic.

[0033] In some embodiments, the regression model includes an error value. The error

20 value may be used to represent the concept that the measurements taken from the recorded images may be merely approximate, and therefore the conclusions reached in the regression models have a slight amount of uncertainty. In some embodiments, the error values of a regression model may be modeled as having a Gaussian distribution. Such an assumption may allow certain embodiments to make more precise conclusions,

25 based on known theory in statistical analysis. Embodiments may also include determining a degree of certainty in the detection results by performing hypothesis testing and/or computing a false detection rate. These methods may be explained more in the following paragraphs, and may be exemplified in test results as shown in FIGs 2B and 3B.

30 **[0034]** As previously stated, the methods described in blocks 108, 110 and 112 may be repeated for each pixel partition set. For example, if there are 2500 pixel partition sets each comprised of 16 pixel partitions from 8 images of a patient's eye, then 2500 regression models are calculated, one for each pixel partition set. Each regression model

conducted therefore measures whether an abnormality may exist in the patient's eye at the particular corresponding region to the particular pixel partition set. Advantages of methods described herein include being able to not only localize and isolate regions of a patient's eye, but also to differentiate disease-related from age-related change and
5 include a false detection rate for interpretation of the results.

II. REGRESSION MODEL

[0035] As described above at block 110, embodiments may generate a regression model for each of the M pixel partition sets of the J images. Any suitable regression model may be used. In general terms, a regression model describes a relationship
10 between one range variable y and at least one explanatory variable X. Regression models utilizing only one explanatory variable are called simple regression models, while having more than one explanatory variable is called multiple regression. Here, the explanatory variable X may represent the time domain of a common location of the patient's eye, recorded at distinct intervals by each of the J images. The data points of X
15 therefore correspond to the times at which the J images in block 102 of FIG. 1A were recorded. The range variable Y may be the values V in block 108 of FIG. 1A, determined for each of the pixel partitions in the pixel partition set.

[0036] In some embodiments, V represents an average RNFL thickness of a pixel partition. Hence, a simple regression model of some embodiments will plot the RNFL
20 thickness of a common region of a patient's eye as a function of the health of the patient's eye over time. For each regression model, there would be J data points (X,Y), one data point for each of the J images corresponding to a common region of the patient's eye.

[0037] One purpose of regression modeling is to generate a mathematical function
25 that accurately describes a "curve fit" to the sample data. While there are finite, discreet data points in real-life sample data, it is easier to analyze data if a continuous function accurately or approximately represents the discreet data points. This curve fit that regression modeling generates may describe such data, and is reflected in the method step at block 110. Some embodiments use a "linear curve fit" to model the data. The
30 linear curve fit regression model may be described as $Y = BX + A$, where Y again is the range variable describing RNFL thickness of a common region of the patient's eye, X is

the time domain, B is a slope value that describes how the RNFL thickness has changed over time, and A is the initial RNFL thickness at base time = 0.

[0038] By generating a regression model using the J data points of a pixel partition set, one may be able to analyze the data to determine how the RNFL thickness in the patient's eye has changed over time. The value B may represent precisely this change, and thus if the change is negative (e.g. B is a negative value), the regression model may then indicate that the RNFL thickness has been degrading or weakening over the sample period of time. Block 112 reflects the aforementioned analysis of what the value B may be and determination of whether the data in the regression model signals an abnormality in the patient's eye.

[0039] Blocks 110 and 112 of FIG. 1A may include more sophisticated calculations and analysis. For example, instead of a simple linear regression model, a more precise curve fit may be calculated, including multiple explanatory variables or including higher ordered curve fits. Other statistical methods may be employed that may minimize the effects of outlier data, and/or may accurately express the degree of error or uncertainty in the curve fits. Various modeling techniques may be used, including ordinary least squares, generalized least squares, Bayesian linear regression, etc. Additional statistical methods may be incorporated to improve analysis, such as calculating a false detection rate for multiple testing. Again, the regression modeling techniques described herein are not limiting, and all techniques devised by persons of ordinary skill in the art related to the techniques described herein may be included in certain embodiments.

[0040] FIG. 5 illustrates an example regression model 500 of one pixel location in a pixel partition set. The dots 510 may represent data points of RNFL thickness of a single pixel location over a period of time. The horizontal axis 520 may represent the time dimension, taken over a period years, with units in months. The vertical axis may represent the RNFL thickness, or the value V in block 108 of FIG. 1A. A regression analysis is performed on this particular pixel to generate the regression line 540. A slope value may be determined from the regression line 540 to demonstrate that the RNFL thickness is gradually decreasing of the measured period of time.

[0041] Again, each pixel location in the pixel partition set may have a regression analysis 500 performed, to similarly obtain a regression line 540. Each regression model thus allows a determination of how the RNFL thickness at that pixel location may have

changed over time. When the entire set of pixel locations has regression models performed on them, an RNFL thickness map showing potential changes over the entire region can be determined.

[0042] Referring to FIG. 1B, flowchart 150 illustrates further analysis for determining whether the common region of the pixel partition set exhibits at least one abnormality, according to some embodiments. That is, according to some embodiments, flowchart 150 may provide further details of block 112 of FIG. 1A, by taking into account age-related rates of change that may be typical in a patient's eye and does not necessarily constitute a disease-related change. At block 152, a rate of change of RNFL thickness of the patient's eye may be determined at the J individual pixel partitions. In some embodiments, the rate of change of RNFL thickness of the patient's eye may be based on the regression model computed at block 110 of FIG. 1A.

[0043] At block 154, the rate of change from block 152 may be compared with an age-related rate of change for each of the J pixel partitions. The age-related rate of change may be obtained from a longitudinal dataset collected from a normal healthy cohort. In some embodiments, a composite model of typical changes due to aging in healthy normal eyes is generated using data sets from multiple healthy patients. The age-related data may be further extended by subdividing the data sets by certain characteristics, e.g. gender, ethnicity, occupation, or other common characteristic. Thus, more specific age-related rates of change may be used to fit a more common profile of the particular patient, in some embodiments.

[0044] At block 156, in some embodiments, a disease-related abnormality may be determined if the rate of change of the patient's eye is more negative than the age-related rate of change being compared against. The age-related rate of change follows a normal distribution. Disease related change may be defined when the rate of change of the patient's eye in a pixel or pixel partition is more negative than the lower 95% confidence limit of the age-related change in the corresponding region. Other cutoff values of the confidence intervals of the age-related change may be used to define the change. In other words, the rate of change of the patient's eye may not be fully accounted for just by the age-related rate of change, and thus it is more likely that the rate of change is disease-related. In some embodiments, as discussed more below, other factors may be used to determined disease-related rates of change, including

incorporating a false detection rate for rates of change at individual pixel partition sets. In other cases, error terms may be introduced into the regression model. In other cases, non-linear regression models may be used. In other cases, any and all of these examples may be used in combination with one another. Embodiments are not so limited.

5 III. REGRESSION MODEL WITH ERROR TERM

[0045] As mentioned above, more sophisticated regression modeling can include an error term and are included in some embodiments. A regression model with an error term is described in more detail here. As mentioned above, the error value may be used to represent the concept that the measurements taken from the recorded images may be
 10 merely approximate, and therefore the conclusions reached in the regression models, e.g. whether there is an abnormality in a region of the patient's eye, have a slight amount of uncertainty.

[0046] Serial RNFL thickness maps are registered with reference to a baseline with reference to the trajectory of the retinal blood vessels. After registering and aligning the
 15 retinal blood vessels in all the images, a functional response and a scalar independent variable model may be constructed:

$$f(s_0, t) = \alpha(s_0) + \beta(s_0)t + \varepsilon(s_0, t)$$

where t denotes time ($t = 0$ represents the time at the baseline); $f(s_0, t)$ denotes the RNFL thickness in a particular geographical location, $s_0 = (x_0, y_0)$, at time t ; $\alpha(s_0)$ is a functional constant representing the true RNFL thickness at the baseline; $\beta(s_0)$
 20 denotes the rate of change of RNFL thickness and $\varepsilon(s_0, t)$ denotes the random measurement error.

[0047] Assuming the measurement error, ε , as a Gaussian process independent of time, t , local RNFL thickness changes at the geographical location s_0 can be estimated by ordinary least square estimation, $\hat{\beta}(s_0) = \frac{Cov[t, f(s_0, t)]}{Var[t]}$, with baseline estimated by
 25 $\hat{\alpha}(s_0) = \bar{f}(s_0, t) - \hat{\beta}(s_0)\bar{t}$. The measurement error ε may be determined based on the linear model used to perform the regression.

IV. HYPOTHESIS TESTING AND FALSE DETECTION RATE

[0048] In some embodiments, the degree of (un)certainty of each conclusion based on the regression models, e.g. whether there is an abnormality in a region of the patient's eye, is determined. Methods for calculating this degree of (un)certainty may include performing hypothesis testing and false detection rate (FDR) error analysis. Other
5 methods for calculating the degree of (un)certainty may be employed, and embodiments of the invention may not be so limited. These calculations may be included in block 112 of FIG. 1A, where the calculations may be used to improve the accuracy of detecting abnormalities.

[0049] In some embodiments where hypothesis testing is used, a null hypothesis may
10 be devised, and statistical analysis may be employed to determine if a slope or rate of change value in the regression model does not satisfy (e.g. can reject) the null hypothesis. For example, a null hypothesis (H_0) may be that the rate of change of RNFL thickness at a region in question does not change, e.g. slope = 0. Typically, hypothesis testing makes determinations based on confidence intervals. For example, the question
15 of whether the null hypothesis of slope = 0 is true (or false) is determined to a degree of confidence, e.g. 95% confidence. In other words, the regression analysis may determine whether the slope value representing change in RNFL thickness has actually changed (e.g. slope is not equal to 0), and whether that determination is accurate to a degree of confidence of 95%. If the slope value is in fact not 0, and the conclusions satisfy the
20 95% confidence interval, then it can be said that we are at least 95% certain the RNFL thickness has been changing, indicating most likely some abnormality in the patient's eye. Thus, in some embodiments, for each region of abnormality, a likelihood the abnormality detected is a false positive may be determined, based on the false detection rate for each region of abnormality. Additionally, in some embodiments, determining
25 whether the common region that corresponds to the pixel partition set exhibits at least one abnormality in the patient's eye is based further on the likelihood the abnormality detected is a false positive, consistent with the false detection rate analysis described herein.

[0050] The hypothesis of no local RNFL thickness change, $H_0: \beta(s_0) = 0$, can be
30 tested by using t-test with $n - 2$ degree of freedom by defining the extreme probability (P-value) as $\mathcal{P} = \mathbb{P}\{|x| \geq \mathcal{T}(s_0) | X \sim T_{n-2}\}$ (the probability of obtaining an absolute value larger than $\mathcal{T}(s_0)$ under t distribution with $n - 2$ degree of freedom), where

$$\mathcal{T}(s_0) = \left| \frac{\hat{\beta}(s_0) - \beta(s_0)}{S_{\hat{\beta}(s_0)}} \right|, S_{\hat{\beta}(s_0)} = \sqrt{\frac{\frac{1}{n-2} \sum_{i=1}^n \{f(s_0, t_i) - [\hat{\alpha}(s_0) + \hat{\beta}(s_0)t_i]\}^2}{\sum_{i=1}^n (t_i - \bar{t})^2}}, \text{ and } n$$

represents the number of longitudinal observations used. The hypothesis of no local RNFL thickness change is rejected if \mathcal{P} is less than or equal to a predefined threshold, which is the significant level of the single test.

5 **[0051]** In other embodiments, a false detection rate (FDR) is also included to further measure the degree of (un)certainty. Generally, FDR measures the number of false abnormalities detected as a ratio of the total number of abnormalities detected. It can be seen, therefore, that the FDR is a useful indicator to show that, given the number of supposed abnormalities detected, how likely is it that the detections are truly legitimate
10 abnormalities. If FDR is relatively low then, and there are a relatively high number of abnormalities detected, then one may be very confident that the patient has a serious eye problem. Persons with ordinary skill in the art may make judgments that differ from this exemplary analysis, and in any case embodiments of the present invention are not so limited. FDR calculations and analysis may be explained in more detail below.

15 **[0052]** Due to the large amount of hypotheses testing involved in the high density RNFL thickness map, it is important to quantify and control the detection error of RNFL thickness change. The false discovery rate (*FDR*) introduced by Benjamini and Hochberg would be an appropriate index to quantify the detection error, which is defined as

20
$$FDR = \mathbb{E} \left[\frac{\text{number of false positive detection}}{\text{number of positive detection}} \right].$$

[0053] The exact FDR may be difficult to be estimated. However, the supremum of the *FDR* can be estimated by $\widehat{sup}(FDR) = \frac{\text{number of tests} \times \text{sig.level used for a single test}}{\text{number of positive detection}}$, where supremum is defined as the least upper bound such that a condition still remains true. In this case, the supremum of the FDR may be an accurate approximation because
25 the FDR is a value that can be pre-defined but may not be reached exactly.

[0054] Other than quantifying the false discovery rate of the multiple significance testing, the FDR can be controlled by various techniques such as the Benjamini Hochberg procedure, and enhanced by a two-stage procedure suggested by Benjamini et al through appropriate adjustment to the significance level used in each significance

test. These two techniques may be included in some embodiments of the present invention, and more techniques may also be included.

The two-stage procedure (with equal weighting):

[0055] Set a predefined *FDR* level (the desired supremum), q , and define $q' = \frac{q}{q+1}$.

5 Order all the single location extreme probabilities $\mathcal{P}_{(1)} \leq \mathcal{P}_{(2)} \leq \dots \leq \mathcal{P}_{(m)}$ and find $k = \max \left\{ j: \mathcal{P}_{(j)} \leq \frac{j q'}{m} \right\}$, where m is the total number of t-test performed in the whole map, j is the value to be maximized such that the inequality after the colon holds.

[0056] Find $k_2 = \max \left\{ j: \mathcal{P}_{(j)} \leq \frac{j q'}{m-k} \right\}$, and rejecting the hypotheses of no change in all locations with $\mathcal{P} \leq \frac{k_2 q'}{m-k}$.

10 [0057] In situations where the units of interest are the thickness change in spatial clusters, the cluster testing and trimming procedure suggested by Benjamini and Heller can be adopted to detect partitions with significant change as well as the specific locations of significant change in those partitions without changing the test statistics.

[0058] By evaluating different pixel partition sizes (1x1, 2x2, 4x4, 8x8 and 10x10
15 pixels) of the RNFL thickness map or image, embodiments of the present invention reveal that the regression analysis is robust to the partition sizes when using the average RNFL thickness within each partition to regress against time. The regression approach is also robust to missing data at locations where scan quality is insufficient for reliable segmentation of the RNFL.

20 **V. NON-LINEAR REGRESSION MODEL**

[0059] As previously alluded to, the functional regressive model calculated at block 110 of FIG. 1A can be extended to quadratic or higher order linear model. When the evaluation of the RNFL is performed in regular intervals, the rate of change of RNFL thickness can be modeled into a Functional Autoregressive Moving Average

25 [*functional ARMA*(p, q)] process:

$$f(s_0, t) = \sum_{i=1}^p \int_{s \in \delta_{s_0}} \varphi_i(s_0, s) \times f(s, t - i) ds + \sum_{j=0}^q \{m_j(s_0) \times \varepsilon(s_0, t - j)\} + \beta(s_0, t)$$

where φ_i and m_i are the weighting parameters related to the previous measures and measurement errors, respectively.

[0060] Given the order of the autoregressive component $p \geq 1$, a more representative form can be obtained by taking the first difference, $\Delta f(s, t) = f(s, t) - f(s, t - 1)$, and
5 the *functional ARMA*(p, q) model becomes:

$$\begin{aligned} \Delta f(s_0, t) = & 1\{p > 0\} \times \int_{s \in \delta_{s_0}} \pi(s_0, s) \times f(s, t - 1) ds \\ & + \sum_{i=1}^{p-1} \int_{s \in \delta_{s_0}} \phi_i(s_0, s) \times \Delta f(s, t - i) ds + \sum_{j=0}^q \{m_j(s_0) \times \varepsilon(s_0, t - j)\} \\ & + \beta(s_0, t) \end{aligned}$$

where π and ϕ_i are the weighting parameters representing the contributions of the latest RNFL thickness and changing pattern in the δ -neighborhood of the geographical location s_0 to current local RNFL thickness change, $\Delta f(s_0, t)$, the higher the absolute value of the parameters, the more the influence power to the progression of the testing
10 location; m_j are the weighed parameters related to the spatio-temporal correlation of measurement errors across time; $1\{\cdot\}$ is an indicator function which equals to 1 if the enclosed criteria is satisfied and 0 otherwise. In some embodiments, lattice data is observed instead of functional data. In such situation, the above model is also known as a Spatio-Temporal Autoregressive Moving Average *STARMA*(p, q) model.

15 [0061] By modeling the RNFL thickness into the above model, the effect of surrounding RNFL thickness and their changes can also be examined. Under the *functional ARMA*(1,1) with $\pi(s_0, s) = 0$ and $\beta(s_0, t) = \beta^*(s_0)$, the functional Autoregressive Moving Average model would able to capture the functional response and a scalar independent variable model mentioned above.

20 [0062] If a sufficiently large sample of images or video data can be collected, it is even possible to extend it into a dynamic process, commonly refer as a continuous-time *ARMA*(p, q), in form of a stochastic partial differential equation (SPDE):

$$\frac{\partial^p}{\partial t^p} f(s_0, t) = \sum_{i=0}^{p-1} \int_{s \in \delta_{s_0}} \phi_i(s_0, s) \frac{\partial^i}{\partial t^i} f(s, t) ds + \sum_{j=0}^q \left\{ m_j(s_0) \frac{\partial^j}{\partial t^j} \varepsilon(s_0, t) \right\} + \beta(s_0, t)$$

where $\frac{\partial^n}{\partial t^n}$ is the n -th stochastic partial derivative with respect to t ; ε is a white noise process (usually assumed to be a Wiener process / Brownian motion).

[0063] On the other hand, if the examination intervals are sporadic, smoothing, such as kernel smoothing, or kriging prediction, builds on Krige (1951), can be applied to approximate the RNFL thickness profile in regular intervals and the *functional ARMA* or the *STARMA* model can be applied.

[0064] In addition, large sample of longitudinal images can be analyzed by adding the mixed effects into the *ARMA* model to form a Functional Autoregressive Moving Average Linear Mixed Model. Biomedical studies using autoregressive linear mixed model have been proposed and developed in Feried (2001) and Funatogawa, et al (2007 & 2008).

VI. EXAMPLE DATA

[0065] FIGs. 2 & 3 are examples of patients' eye images and subsequent detection of RNFL progression using existing OCT methods and embodiments of the present invention. Specifically, FIGs. 2A and 3A show results from the Guided Progression Analysis on the RNFL Thickness Maps performed by the Cirrus HD-OCT (Carl Zeiss Meditec, Dublin, CA), a commercially available OCT product, and FIGs. 2B and 3B show results from embodiments of the present invention. For each A & B pair, the same data set is used to illustrate improvements by embodiments over the commercially available techniques. Each figure includes a series of RNFL thickness maps recorded over a period of time, where the total span of time ranges from August 2007 to July 2011 for FIG. 2 and from August 2007 to September 2012 for FIG. 3.

[0066] Referring to FIGs. 2A & 2B, at item 202, an RNFL thickness map of a patient's eye was first shown to be recorded on August 2, 2007 (Exam 1). At item 204, a total of 11 RNFL thickness images were recorded, the last recording occurring on July 21, 2011 (Exam 11). Images 206 are blue, yellow, and red images, where the color represents RNFL thickness, according to the scale 208, ranging from 0-350 micrometers.

[0067] In FIG. 2A, test results 200 from an existing technique, Cirrus HD-OCT, were obtained in order to detect for an eye abnormality glaucoma. The substantially black and white images below the colored figures in FIG. 2A represent the analysis performed by

the Cirrus HD-OCT technique. Item 210 of FIG. 2A shows that at Exam 8, an eye abnormality was detected, colored by the red blotch in the substantially black and white photo. This detection is based on the Guided Progression Analysis of the Cirrus HD-OCT product. It highlights the areas where the differences in RNFL thickness between the follow-up visit and the baseline 1 and baseline 2 visits are greater than the test-retest variability of RNFL thickness in those areas. Thus, using previously existing methods, an eye abnormality could be detected based on different time-variant images spanning over two years and three months. However, it is not known if the changes represent age-related change and the probability that the changes detected are false positive.

10 **[0068]** In contrast, FIG. 2B illustrates example test results generated by embodiments of the present invention. Here, 11 eye exams, from image 220 to image 224, were received, and regression model analysis as described in FIG. 1A was used to determine eye abnormalities. The test results of FIG. 2B show that embodiments reveal eye abnormalities for the same set of images 206 in FIG. 2A in July 2009 with a false detection rate <5% (coded in red), at item 228, or 4 months earlier than previously existing methods. The substantially black and white images 224, with spots of yellow and red, represent detection results of abnormalities for various embodiments of the present invention.

[0069] For FIG. 2B, detection may have been determined following the regression modeling analysis as described in FIG. 1A, at blocks 108-112. Specifically, the 11 images of FIG. 2B may have been divided into pixel partitions, say 4x4 pixel partitions. Pixel partition sets were then identified, each including a pixel partition from each of the 11 images corresponding to a common region of the patient's eye. The RNFL thickness of each pixel partition would be calculated and used in a regression model. Calculating the regression model for each pixel partition set, by plotting the RNFL thickness over the time period of the 11 images, would then determine a rate of change value for the RNFL thickness of the common region corresponding to the pixel partition set.

25 **[0070]** The red regions of image 224 represent regions of RNFL thickness that changed sufficiently, according to the regression modeling, and were determined to be sufficiently abnormal according to a fixed FDR threshold, described above at Section IV. Specifically, regions highlighted as red may represent locations with RNFL

progression where false discovery rate is less than 5%. Similarly, the yellow regions of the images in FIG. 2B represent regions of RNFL thickness that changed sufficiently, according to the regression modeling, and were determined to be sufficiently abnormal according to hypothesis testing without a fixed FDR threshold, described above at

5 Section IV. Specifically, regions highlighted as yellow represent locations with RNFL progression at 5% significant level without controlling the false discovery rate. Thus, in some embodiments that detect for abnormalities using a t-test without controlling for false discovery rate, the yellow portions of images 224 show that there are abnormalities to a confidence level of 95% in the yellow regions as early as April 7, 2008, image 222

10 (Exam 3).

[0071] With progressively worsening results, controlling for the false detection rate using at least one of the techniques described herein, reveal an even clearer detection of abnormalities. These results are illustrated in the red portions of images 224, most noticeably seen in the images from July 27, 2009 to July 21, 2011.

15 **[0072]** At Item 226, FIG. 2B also illustrates the degree of confidence of detecting abnormalities, based on computing t-tests with the results shown. These steps may be included in the method step of block 112 of FIG. 1A, and may be based on techniques described in Section IV. For example, under image 222, recorded on April 7, 2008, there are two sets of numbers: (R) and (Y), where (R) represents additional detection

20 results when controlling for the false detection rate, and (Y) represents additional results without controlling for the false detection rate. For (R) at item 222, $FDR \leq 0.0\%$, meaning that controlling for the false detection rate may not yet yield any noticeable results. Indeed, there is no red yet shown at the time of this image. However, for (Y), $P \leq 0.050$, meaning all areas of image 222 colored in yellow are $1 - P = 1 - 0.050 = 95\%$

25 confident to show an abnormality at those regions. Given the total number of spots colored in yellow, analysis using embodiments of the present invention also showed a false detection rate (FDR) out of all of these yellow spots to be 75.0%. Given then that $100\% - 75.0\% = 25.0\%$ of the yellow area is *not* a false detection (to a confidence level of 95%), those with ordinary skill in the art would still determine that an abnormality is

30 present, even as early as April 2008.

[0073] Image 228, recorded on July 27, 2009 (Exam 7), may illustrate another example of the degree of confidence of detecting abnormalities. Here, there are red and

yellow areas present after detection analysis using techniques of the present invention. The yellow regions may be interpreted as above, since $P \leq 0.050$. FDR = 25.4%, meaning 74.6% of the yellow region is highly likely (to a confidence level of 95%) that there is an abnormality in those areas. However, the areas in red are even more
5 convincing. $P \leq 0.003$ for red; in other words, all areas in red are $1 - P = 1 - 0.003 = 99.7\%$ confident to show an abnormality at those regions. Also, since red controls for the number of false detections, FDR is set at 4.8%, meaning only 4.8% of the red area is a false detection at the 99.7% confidence level. Therefore, the red region even more convincingly shows that there may be a serious abnormality with the patient's eye.

10 **[0074]** Referring to FIG. 2C, image 240 shows that the detection may be displayed in a color-coded map indicating the rates of change of RNFL thickness at individual pixel partitions in the latest follow-up visit. The rates of change of RNFL thickness are shown in a color-coded scale on the right.

[0075] Referring to FIG. 2D, image 260 illustrates that not all the detected changes
15 are disease-related. After removing the pixel partitions that represent age-related change, it is possible to generate a map showing disease-related change. The area showing disease-related change is smaller than the one showing both disease- and age-related change (FIG. 2C). Thus, in some embodiments, methods may account for age-related change in the eye in order to generate a more accurate determination of disease-
20 related change.

[0076] FIGs. 3 A-D are other illustrative results comparing various techniques of the present invention and previously existing methods. These illustrations can all be interpreted using similar analysis described for FIGs. 2A-D, above.

[0077] Referring to FIG. 3A, test results 300 shows detection of abnormalities using
25 the Cirrus HD-OCT Guided Progression Analysis. An abnormality may be detected on May 3, 2012, based on the earliest image in August 2007. However, based on techniques of the present invention, shown in test results 320, detection of abnormalities may be evident as early as January 2011 with a false discovery rate $<5\%$, fully 16 months earlier (FIG. 3B).

30 **[0078]** Referring to FIG. 3C, as shown in image 340, detection may be displayed in a color-coded map showing the rates of change of RNFL thickness at individual pixel partitions in the latest follow-up visit.

[0079] Referring to FIG. 3D, image 360 illustrates RNFL changes that are disease-related. A significant portion of the detected changes in FIG. 3C was age-related.

[0080] Referring to FIG. 4A, images 400 show an example of a healthy normal eye followed from July 11, 2008 to November 27, 2012. Significant progressive RNFL
5 thinning was detected on July 30, 2012 with a false detection rate <5%. Detection may be displayed in a color-coded map showing the rates of change of RNFL thickness at individual pixel partitions in the latest follow-up visit (FIG. 4B). Those with ordinary skill in the art would determine that an abnormality is present, according to typical techniques in the industry. However, embodiments of the present invention are able to
10 illustrate that there was no disease-related change after adjusting for age-related losses (FIG. 4C).

[0081] Referring to FIG. 4B, as mentioned previously, image 420 may illustrate a detection of an abnormality in the eye according to existing commercial methods. However, referring to FIG. 4C, as mentioned earlier, image 440 may take the same
15 patient and data, but determine that there is no disease-related change after adjusting for age-related losses.

[0082] Embodiments of the present invention are unique and advantageous in that it is believed no one has differentiated disease-related change from age-related change in the eye using a plurality of regression models, each for a different region of the eye. Current
20 methods include calculating the rates of change of RNFL thickness over the entire image as a whole, using pixel partitions of each image and comparing these calculated rates of change with the expected age-related rates of change at the corresponding pixel partitions. Also, it is believed no one has measured false discovery rates for each measurement, nor used the false discovery rate to identify an abnormality.

[0083] The spectral-domain optical coherence tomography is a relatively new
25 technology (introduced in 2006) for retinal nerve fiber layer (RNFL) imaging, allowing for much growth in improving detection methods and apparatuses. With high speed and high resolution imaging, objective and reproducible measurement of the retinal nerve fiber layer has been shown feasible. Measurement of progressive retinal nerve fiber
30 layer changes has become an important paradigm for detection of progression in glaucoma patients. Embodiments of the present invention therefore have enormous market potential as there are currently a number of companies who specialize in this

field. The need for a more robust and sensitive algorithm for detection of RNFL progression is eminently needed in the market. Embodiments of the present invention has been shown to detect abnormalities in RNFL thickness levels in the eye up to 16 months before existing commercial applications do, representing a superior advantage over existing brands.

VII: COMPUTER SYSTEM

[0084] Having described multiple aspects of determine whether abnormalities may exist in a patient's eye using regression models, an example of a computing system in which various aspects of the disclosure may be implemented may now be described with respect to FIG. 6. According to one or more aspects, a computer system as illustrated in FIG. 6 may be incorporated as part of a computing device, which may implement, perform, and/or execute any and/or all of the features, methods, and/or method steps described herein. For example, computer system 600 may represent some of the components of a medical device or imaging device. A medical device may be any computing device with an input sensory unit, such as a camera and/or a display unit. Examples of a medical device include but are not limited to slit lamp digital imaging cameras, ophthalmic photographers, optical biometers and related computer systems and software. In one embodiment, the system 600 is configured to implement the methods of flowchart 100 or 150 described above. FIG. 6 provides a schematic illustration of one embodiment of a computer system 600 that can perform the methods provided by various other embodiments, as described herein, and/or can function as the host computer system, a remote kiosk/terminal, a point-of-sale device, a mobile device, a set-top box, and/or a computer system. FIG. 6 is meant only to provide a generalized illustration of various components, any and/or all of which may be utilized as appropriate. FIG. 6, therefore, broadly illustrates how individual system elements may be implemented in a relatively separated or relatively more integrated manner.

[0085] The computer system 600 is shown comprising hardware elements that can be electrically coupled via a bus 605 (or may otherwise be in communication, as appropriate). The hardware elements may include one or more processors 610, including without limitation one or more general-purpose processors and/or one or more special-purpose processors (such as digital signal processing chips, graphics acceleration processors, and/or the like); one or more input devices 615, which can

include without limitation a camera, a mouse, a keyboard and/or the like; and one or more output devices 620, which can include without limitation a display unit, a printer and/or the like.

[0086] The computer system 600 may further include (and/or be in communication with) one or more non-transitory storage devices 625, which can comprise, without limitation, local and/or network accessible storage, and/or can include, without limitation, a disk drive, a drive array, an optical storage device, a solid-state storage device such as a random access memory (“RAM”) and/or a read-only memory (“ROM”), which can be programmable, flash-updateable and/or the like. Such storage devices may be configured to implement any appropriate data storage, including without limitation, various file systems, database structures, and/or the like.

[0087] The computer system 600 might also include a communications subsystem 830, which can include without limitation a modem, a network card (wireless or wired), an infrared communication device, a wireless communication device and/or chipset (such as a Bluetooth® device, an 802.11 device, a WiFi device, a WiMax device, cellular communication facilities, etc.), and/or the like. The communications subsystem 830 may permit data to be exchanged with a network (such as the network described below, to name one example), other computer systems, and/or any other devices described herein. In many embodiments, the computer system 600 may further comprise a non-transitory working memory 635, which can include a RAM or ROM device, as described above.

[0088] The computer system 600 also can comprise software elements, shown as being currently located within the working memory 635, including an operating system 640, device drivers, executable libraries, and/or other code, such as one or more application programs 645, which may comprise computer programs provided by various embodiments, and/or may be designed to implement methods, and/or configure systems, provided by other embodiments, as described herein. Merely by way of example, one or more procedures described with respect to the method(s) discussed above, for example as described with respect to FIG. 1A or 1B, might be implemented as code and/or instructions executable by a computer (and/or a processor within a computer); in an aspect, then, such code and/or instructions can be used to configure and/or adapt a general purpose computer (or other device) to perform one or more operations in

accordance with the described methods. The computer system 600 may also comprise various hardware elements, such as imaging device 650. The imaging device 650 may perform various functions, such as recording images or other forms of data.

[0089] A set of these instructions and/or code might be stored on a computer-readable storage medium, such as the storage device(s) 625 described above. In some cases, the storage medium might be incorporated within a computer system, such as computer system 600. In other embodiments, the storage medium might be separate from a computer system (e.g., a removable medium, such as a compact disc), and/or provided in an installation package, such that the storage medium can be used to program, configure and/or adapt a general purpose computer with the instructions/code stored thereon. These instructions might take the form of executable code, which is executable by the computer system 600 and/or might take the form of source and/or installable code, which, upon compilation and/or installation on the computer system 600 (e.g., using any of a variety of generally available compilers, installation programs, compression/decompression utilities, etc.) then takes the form of executable code.

[0090] Substantial variations may be made in accordance with specific requirements. For example, customized hardware might also be used, and/or particular elements might be implemented in hardware, software (including portable software, such as applets, etc.), or both. Further, connection to other computing devices such as network input/output devices may be employed.

[0091] Some embodiments may employ a computer system (such as the computer system 600) to perform methods in accordance with the disclosure. For example, some or all of the procedures of the described methods may be performed by the computer system 600 in response to processor 610 executing one or more sequences of one or more instructions (which might be incorporated into the operating system 640 and/or other code, such as an application program 645) contained in the working memory 635. Such instructions may be read into the working memory 635 from another computer-readable medium, such as one or more of the storage device(s) 625. Merely by way of example, execution of the sequences of instructions contained in the working memory 635 might cause the processor(s) 610 to perform one or more procedures of the methods described herein, for example a method described with respect to FIG. 1A or 1B.

[0092] The terms “machine-readable medium” and “computer-readable medium,” as used herein, refer to any medium that participates in providing data that causes a machine to operate in a specific fashion. In an embodiment implemented using the computer system 600, various computer-readable media might be involved in providing instructions/code to processor(s) 610 for execution and/or might be used to store and/or carry such instructions/code (e.g., as signals). In many implementations, a computer-readable medium is a physical and/or tangible storage medium. Such a medium may take many forms, including but not limited to, non-volatile media, volatile media, and transmission media. Non-volatile media include, for example, optical and/or magnetic disks, such as the storage device(s) 625. Volatile media include, without limitation, dynamic memory, such as the working memory 635. Transmission media include, without limitation, coaxial cables, copper wire and fiber optics, including the wires that comprise the bus 605, as well as the various components of the communications subsystem 630 (and/or the media by which the communications subsystem 630 provides communication with other devices). Hence, transmission media can also take the form of waves (including without limitation radio, acoustic and/or light waves, such as those generated during radio-wave and infrared data communications).

[0093] In one or more examples, the functions described may be implemented in hardware, software, firmware, or any combination thereof. If implemented in software, the functions may be stored on or transmitted over as one or more instructions or code on a computer-readable medium. Computer-readable media may include computer data storage media. Data storage media may be any available media that can be accessed by one or more computers or one or more processors to retrieve instructions, code and/or data structures for implementation of the techniques described in this disclosure. “Data storage media” as used herein refers to manufactures and does not refer to transitory propagating signals. By way of example, and not limitation, such computer-readable media can comprise RAM, ROM, EEPROM, CD-ROM or other optical disk storage, magnetic disk storage, or other magnetic storage devices, flash memory, or any other medium that can be used to store desired program code in the form of instructions or data structures and that can be accessed by a computer. Disk and disc, as used herein, includes compact disc (CD), laser disc, optical disc, digital versatile disc (DVD), floppy disk and blu-ray disc where disks usually reproduce data magnetically, while discs

reproduce data optically with lasers. Combinations of the above should also be included within the scope of computer-readable media.

[0094] The code may be executed by one or more processors, such as one or more digital signal processors (DSPs), general purpose microprocessors, application specific
5 integrated circuits (ASICs), field programmable logic arrays (FPGAs), or other equivalent integrated or discrete logic circuitry. Accordingly, the term “processor,” as used herein may refer to any of the foregoing structure or any other structure suitable for implementation of the techniques described herein. In addition, in some aspects, the functionality described herein may be provided within dedicated hardware and/or
10 software modules configured for encoding and decoding, or incorporated in a combined codec. Also, the techniques could be fully implemented in one or more circuits or logic elements.

[0095] The techniques of this disclosure may be implemented in a wide variety of devices or apparatuses, including a wireless handset, an integrated circuit (IC) or a set of
15 ICs (e.g., a chip set). Various components, modules, or units are described in this disclosure to emphasize functional aspects of devices configured to perform the disclosed techniques, but do not necessarily require realization by different hardware units. Rather, as described above, various units may be combined in a codec hardware unit or provided by a collection of interoperative hardware units, including one or more
20 processors as described above, in conjunction with suitable software and/or firmware stored on computer-readable media.

[0096] Various examples have been described. These and other examples are within the scope of the following claims.

WHAT IS CLAIMED IS:

- 1 1. A method for identifying regions of abnormalities in a patient's
2 eye, the method comprising:
 - 3 receiving a plurality of images of the patient's eye, each image obtained
4 at a different time, wherein each image of the plurality of images is comprised of a
5 plurality of pixels, each pixel indicating a time-varying characteristic of a particular
6 location in the patient's eye;
 - 7 dividing each image into a plurality of pixel partitions, each pixel
8 partition including one or more pixels;
 - 9 identifying a plurality of pixel partition sets, each pixel partition set
10 comprising a pixel partition from each image, wherein the pixel partitions of the pixel
11 partition set correspond to a common region in the patient's eye;
 - 12 for each pixel partition set:
 - 13 for each pixel partition of the pixel partition set:
 - 14 determining a respective value for the respective common region
15 of the pixel partition set, wherein the respective value corresponds to the
16 time-varying characteristic of the pixel partition at the time of the
17 corresponding image;
 - 18 calculating, with a computer system, a regression model from the
19 respective values of the pixel partitions of the pixel partition set, wherein the
20 regression model comprises a rate of change value; and
 - 21 determining whether the common region that corresponds to the pixel
22 partition set exhibits at least one abnormality in the patient's eye, based on whether
23 the rate of change value of the regression model is more negative than a rate of age-
24 related change.
- 1 2. The method of claim 1, wherein:
 - 2 the rate of change value comprises a slope value, the slope value being a
3 coefficient of a term in the regression model; and

4 detecting one or more regions of abnormalities is based further on
5 determining whether the slope value exceeds the slope value of age-related change.

1 3. The method of claim 2, wherein:
2 the time-varying characteristic is a retinal nerve fiber layer (RNFL)
3 thickness;
4 the slope value represents the rate of change in the RNFL thickness; and
5 the regression model further comprises a baseline value that represents
6 the RNFL thickness of the earliest recorded image, and an error value.

1 4. The method of claim 3, wherein the respective value for the
2 respective common region of the pixel partition set is the average RNFL thickness of
3 the pixel partition for the respective common region.

1 5. The method of claim 3, wherein the error value follows a
2 Gaussian distribution;
3 the method further comprising:
4 determining a false detection rate for each region of abnormality
5 detected, based on the error value; and
6 determining, for each region of abnormality, a likelihood the abnormality
7 detected is a false positive, based on the false detection rate for each region of
8 abnormality,
9 wherein determining whether the common region that corresponds to the
10 pixel partition set exhibits at least one abnormality in the patient's eye is based further
11 on the likelihood the abnormality detected is a false positive.

1 6. The method of claim 1, wherein the regression model is a
2 polynomial of order at least one, and wherein the rate of change value is a coefficient of
3 the linear term or greater term of the polynomial.

1 7. The method of claim 1, wherein the plurality of images comprises
2 at least three images that are recorded successively over time.

1 8. The method of claim 1, wherein the pixel partitions comprise at
2 least a single pixel.

1 9. The method of claim 1, further comprising:
2 recording the plurality of images of the patient's eye using an imaging
3 device.

4 10. An apparatus for identifying regions of abnormalities in a
5 patient's eye, comprising
6 a processor configured to:
7 receive a plurality of images of the patient's eye, each image obtained at
8 a different time, wherein each image of the plurality of images is comprised of a
9 plurality of pixels, each pixel indicating a time-varying characteristic of a particular
10 location in the patient's eye;

11 divide each image into a plurality of pixel partitions, each pixel partition
12 including one or more pixels;

13 identify a plurality of pixel partition sets, each pixel partition set
14 comprising a pixel partition from each image, wherein the pixel partitions of the pixel
15 partition set correspond to a common region in the patient's eye;

16 for each pixel partition set:

17 for each pixel partition of the pixel partition set:

18 determine a respective value for the respective common region of
19 the pixel partition set, wherein the respective value corresponds to the time-
20 varying characteristic of the pixel partition at the time of the corresponding
21 image;

22 calculate a regression model from the respective values of the pixel
23 partitions of the pixel partition set, wherein the regression model comprises a rate of
24 change value; and

25 determine whether the common region that corresponds to the pixel
26 partition set exhibits at least one abnormality in the patient's eye, based on whether
27 the rate of change value of the regression model is more negative than a rate of age-
28 related change.

1 11. The apparatus of claim 10, wherein:

2 the rate of change value comprises a slope value, the slope value being a
3 coefficient of a term in the regression model; and

4 the processor is further configured to determine whether the slope value
5 exceeds the slope value of age-related change.

1 12. The apparatus of claim 11, wherein:
2 the time-varying characteristic is a retinal nerve fiber layer (RNFL)
3 thickness;

4 the slope value represents the rate of change in the RNFL thickness; and

5 the regression model further comprises a baseline value that represents
6 the RNFL thickness of the earliest recorded image, and an error value.

1 13. The apparatus of claim 12, wherein the respective value for the
2 respective common region of the pixel partition set is the average RNFL thickness of
3 the pixel partition for the respective common region.

1 14. The apparatus of claim 12, wherein the error value follows a
2 Gaussian distribution; and

3 the processor is further configured to:

4 determine a false detection rate for each region of abnormality
5 detected, based on the error value; and

6 determine, for each region of abnormality, a likelihood the
7 abnormality detected is a false positive, based on the false detection rate for each
8 region of abnormality,

9 wherein determining whether the common region that
10 corresponds to the pixel partition set exhibits at least one abnormality in the
11 patient's eye is based further on the likelihood the abnormality detected is a false
12 positive.

1 15. The apparatus of claim 10, wherein the regression model is a
2 polynomial of order at least one, and wherein the rate of change value is a coefficient of
3 the linear term or greater term of the polynomial.

1 16. The apparatus of claim 10, wherein the plurality of images
2 comprises at least three images that are recorded successively over time.

1 17. The apparatus of claim 10, wherein the pixel partitions comprise
2 at least a single pixel.

1 18. The apparatus of claim 10, further comprising an imaging device
2 configured to record the plurality of images of the patient's eye.

1 19. A computer program product residing on a processor-readable
2 medium and comprising processor-readable instructions configured to cause a processor
3 to:

4 receive a plurality of images of the patient's eye, each image obtained at
5 a different time, wherein each image of the plurality of images is comprised of a
6 plurality of pixels, each pixel indicating a time-varying characteristic of a particular
7 location in the patient's eye;

8 divide each image into a plurality of pixel partitions, each pixel partition
9 including one or more pixels;

10 identify a plurality of pixel partition sets, each pixel partition set
11 comprising a pixel partition from each image, wherein the pixel partitions of the pixel
12 partition set correspond to a common region in the patient's eye;

13 for each pixel partition set:

14 for each pixel partition of the pixel partition set:

15 determine a respective value for the respective common region of
16 the pixel partition set, wherein the respective value corresponds to the time-
17 varying characteristic of the pixel partition at the time of the corresponding
18 image;

19 calculate a regression model from the respective values of the pixel
20 partitions of the pixel partition set, wherein the regression model comprises a rate of
21 change value; and

22 determine whether the common region that corresponds to the pixel
23 partition set exhibits at least one abnormality in the patient's eye, based on whether

24 the rate of change value of the regression model is more negative than a rate of age-
25 related change.

ABSTRACT OF THE DISCLOSURE

Methods, apparatuses, and computer readable media for detecting abnormalities in a characteristic of an eye using eye-imaging methods are presented. A plurality of images of the eye are received over time. Each image includes a plurality of pixels, which can be partitioned into blocks of pixels with varying sizes, called pixel partitions. A value is determined for each pixel partition, e.g., an average of the pixel values. A pixel partition set may be identified, which includes a pixel partition from each image, corresponding to a common region of a patient's eye. A regression model is computed for each pixel partition set using the values determined for each pixel partition. The regression model computes a rate of change of the retinal nerve fiber thickness at individual pixel partitions over time. An abnormality may be identified by comparing the rates of change of the model and the expected age-related rate of change.